

KAUNAS UNIVERSITY OF TECHNOLOGY

JONAS NAVICKAS

ANALYSIS OF THE EFFECT OF HIGH
FREQUENCY VIBRATIONS ON HUMAN
BIOLOGICAL TISSUES

Doctoral dissertation
Technological Sciences, Mechanical Engineering (09T)

2018, Kaunas

This doctoral dissertation was prepared at Kaunas University of Technology, Faculty of Mechanical Engineering, Department of Mechatronics during the period of 2013–2018.

Scientific Supervisor:

Habil. Dr. Algimantas BUBULIS (Kaunas University of Technology, Mechanical Engineering, Institute of Mechatronics, 09T).

Doctoral dissertation has been published in:

<http://ktu.edu>

Editor:

Inga Nanaronytė (Publishing Office “Technologija”)

Armandas Rumšas (Publishing Office “Technologija”)

© J. Navickas, 2018

ISBN 978-609-02-1477-0

The bibliographic information about the publication is available in the National Bibliographic Data Bank (NBDB) of the Martynas Mažvydas National Library of Lithuania.

KAUNO TECHNOLOGIJOS UNIVERSITETAS

JONAS NAVICKAS

AUKŠTADAŽNIŲ VIRPESIŲ POVEIKIO
BIOLOGINIAMS ŽMOGAUS AUDINIAMS
TYRIMAS

Daktaro disertacija
Technologijos mokslai, mechanikos inžinerija (09T)

2018, Kaunas

Disertacija rengta 2013–2018 metais Kauno technologijos universiteto Mechatronikos institute.

Mokslinis vadovas:

Habil. dr. Algimantas BUBULIS (Kauno technologijos universitetas, technologijos mokslai, mechanikos inžinerija, 09T).

Interneto svetainės, kurioje skelbiama disertacija, adresas:

<http://ktu.edu>

Redagavo:

Inga Nanartonytė (leidykla „Technologija“)

Armandas Rumšas (leidykla „Technologija“)

© J.Navickas, 2018

ISBN 978-609-02-1477-0

Leidinio bibliografinė informacija pateikiama Lietuvos nacionalinės Martyno Mažvydo bibliotekos Nacionalinės bibliografijos duomenų banke (NBDB).

TABLE OF CONTENTS

1. INTRODUCTION	7
2. PROBLEM ANALYSIS AND FORMULATION OF THE TASKS	10
2.1. The Blood Circulatory System of the Human and Anatomy of the Vessel.	10
2.2. Vascular Disease	13
2.3. Application of Ultrasound in Medicine	17
2.4. The Process of Cavitation.....	19
2.4.1. Acoustic Cavitation.....	19
2.4.2. Tension.....	20
2.4.3. The Method of Bertholet.....	20
2.4.4. Inclusions	20
2.4.5. Centrifuging	21
2.5. Dynamics of the Cavitation Bubble	22
2.5.1. Dynamics of the Spherical Bubble.....	22
2.5.2. Dynamics of Aspherical Bubble	23
2.6. Patented Ultrasound Devices for the Intravascular Thrombus Decomposition.....	24
2.7. Industrial Devices for the Intravascular Thrombus Decomposition.....	33
2.8. Computational Modeling of Commercial Devices Intended for Clearing Blood Vessels	36
2.9. Formulation of Objectives and Tasks.....	38
3. DESIGN AND MODELING OF THE WAVEGUIDE	40
3.1. Design of Ultrasonic Device for Internal Vascular Clearing	40
3.1.1. Description of the Device.....	40
3.1.2. Structural Layout of the Device	42
3.1.3. Novelty of the Device	43
3.1.4. Technological Challenges	43
3.2. Design of the Tube-Shaped Ultrasound Waveguide	44
3.2.1. Description of the Device.....	44
3.2.2. Structural Layout of the Device	46
3.2.3. Novelty of the Device	46
3.2.4. Technological Challenges	47
3.3. Computational Modeling of a Waveguide Wire Operating within a Blood Filled Blood Vessel	47
3.4. Summary of Chapter 2	57
4. THEORETICAL INVESTIGATION OF THE TUBE-SHAPED WAVEGUIDE WIRE	59
4.1. Sound Waves in Fluids.....	59
4.2. Sound Waves in a Tissue.....	61
4.3. Conditions for the Existence of the Proposed Solution.....	63
4.4. Description of Caverns	64
4.5. The Equations for the Determination of the Caverns	67

4.6. Displacements of the Caverns	70
4.7. Calculation of the Size of the Cavern.....	74
4.8. Summary of Chapter 3	74
5. EXPERIMENTAL INVESTIGATION OF THE TUBE-SHAPED WAVEGUIDE WIRE WAVEGUIDE SYSTEM.....	76
5.1. Equipment Used for the Research	76
5.1.1. Ultrasound Generator VT-400	76
5.1.2. The Ultrasound Transducer.....	77
5.2. Effect of Low Intensity Cavitation on Isolated Human Arteries	77
5.3. Experimental Investigation of Tube-Shaped Waveguide Displacement Using Polytec PSV 3D Laser Vibrometer	85
5.4. Amplitude-Frequency Characteristic.....	90
5.5. Experimental Investigation of Waveguide Wire Influence to Surrounding Fluids	93
5.5.1. Mechanical and Thermal Influence on Blood	93
5.5.2. Determination of the Safe Operating Regime for the Ultrasound System	96
5.6. Impedance Analysis of the Waveguide in Different Working Regimes .	98
5.7. Summary of Chapter 4	106
CONCLUSIONS	107
REFERENCES	108
SCIENTIFIC PUBLICATIONS IN THE INTEREST FIELD OF THE THESIS .	114
ANNEXES	117
Annex 1	117
Annex 2	120

1. INTRODUCTION

The Relevance of the Topic

Cardiovascular diseases are the leading cause of death in the European Union. They cover a broad class of medical problems and disorders affecting the circulatory system (the heart and the blood vessels). They commonly stem from atherosclerosis (the abnormal build-up of plaque made of, among other materials, cholesterol or fatty substances deposited on the inside walls of arteries). Ischaemic heart disease (heart attacks) and cerebrovascular diseases (strokes) are considered to be the most common diseases affecting the circulatory system in humans [1].

Currently, more than 6 million new cases of cardiovascular diseases are recorded in EU every year, and in Europe as a whole this number is in excess of 11 million. In total, almost 49 million people live with CVD in the EU, which results in high costs to the EU economies – nearly €210 billion a year [2]. Of the total cost of CVD in the EU, health care costs account for approximately 53 percent (€111 billion), whereas productivity losses contribute 26 percent (€54 billion), and informal care of people suffering from CVD costs 21 percent of all the relevant expenses (€45 billion).

The main risk factors for cardiovascular diseases are as follows: high blood pressure (annually, 15 percent more in Western Europe) [3], smoking (16 percent of deaths in adults over 30), just to mention a few [4]. Excessive alcohol consumption (which has recently been considered a major problem in Lithuania, too), high sugar consumption (the cause of 15 percent of deaths due to CVD), obesity (+5 percent in Lithuania during the last 5 years) [5], high cholesterol levels (closely linked to unhealthy lifestyles, overweight and diabetes), lack of physical activity, frequent stress and diabetes (expected to go 165 percent up globally in 2050) [6].

Almost half of the individuals who have had their extremity amputated due to a vascular disease die within 5 years. This is higher than the five-year mortality rates for breast cancer, colon cancer, and prostate cancer [7]. Nearly 55 percent of persons suffering from diabetes who have undergone a lower limb amputation will require the amputation of the other leg as well within 2–3 years [8].

The majority of limb amputations is caused by circulatory disturbances, such as vascular occlusions and strictures. Consequently, it is necessary to search for novel and more effective methods of eliminating vascular malformations. For this reason, various invasive and non-invasive ultrasonic devices are currently being used. However, given the depressing statistics, they are far from being sufficiently effective.

The discovery of a modern and more advanced ultrasonic interventional vascular clearing methodology would enable saving not only the limbs of CVD patients and their lives but would also contribute to the wealth of the economies of Lithuania and Europe as a whole as this would allow saving lots of finances currently being spent on treating patients in non-effective ways, as well as nursing and taking care of them after they lose their ability to work.

Aim and Objectives of the Research

The aim of the research is to investigate the effect of the active invasive ultrasonic vascular clearing systems on live human tissues and to use the relevant findings and the results obtained in the course of the research for the further improvement of the active members that are currently used in ultrasonic systems.

In order to achieve the above stated aim, the following objectives were set:

1. To accomplish comprehensive analysis of literature on the human cardiovascular system covering the currently known effects of ultrasound on human tissues, to collect data on various waveguides currently being used for the purpose of vascular clearing, and to analyze the blood vessel cleaning devices currently available on the market.
2. To develop a multipurpose waveguide capable of operating in three directions (along axes x , y , and z) and suitable for restoring the functioning of the blood vessels in an interventional way.
3. To develop a technique for the research of the cavitation process within fluids while mathematically modeling the waveguide of a newly designed structure operating within the tissue-confined fluid.
4. To investigate experimentally the newly designed waveguide (operating as an active member of the ultrasonic vascular clearing system), to find out the effects it has on human tissues and the medium within which it is being operated (blood), and to determine the operational characteristics of the system under consideration.

Methods and Means

This work is carried out by using theoretical and experimental research methods. The theoretical studies were performed by using COMSOL MULTIPHYSICS computer software packages. The experimental studies for the performance of piezoelectric actuators were created in the Institute of Mechatronics, Kaunas University of Technology. The experimental results were obtained by using the most up-to-date available non-contact laser measuring equipment.

Research Novelty

1. A unique waveguide of an innovative shape has been developed;
2. A dynamic model and a computational methodology of the unique waveguide featuring an innovative shape has been created;
3. The effect of cavitation caused by the ultrasound on human tissues and the medium within which it is being operated (namely, blood) has been examined.

Practical Value

An innovative waveguide of a unique shape has been designed for invasive clearing of blood vessels capable of generating the cavitation flow by means of inducing mechanical multidimensional vibrations of ultrasonic frequency. The waveguide under consideration is used within the ultrasound system for the elimination of vascular disorders in humans. The information gathered while preparing the thesis was used for the research in the framework of the joint KTU and the Lithuanian University of Health Sciences project “Go-SMART” funded by Research Council of Lithuania, Project No. MIP-097/15.

Work Results Submitted for Evaluation

1. The experimental trials and the discovered values of the operating characteristics of the mechanical ultrasound apparatuses fitted with the waveguide of a unique shape;
2. The calculation of the effect stemming from waves caused within the tissue-confined body fluid during the operation of the waveguide;
3. Experimental trials of the ultrasound effect on live human tissues.

Work Approval

The scientific research results and publications focused on the topic of this doctoral thesis were presented in 9 international scientific conferences, published in 2 international journals having an *Impact Factor* as well as in 6 other publications listed in the main journal of the *Institute for Scientific Information (ISI)*. Two different scientific inventions were patented in Lithuania.

Scope of the Dissertation

The dissertation consists of an introduction, four parts, general conclusions, a bibliography of 99 sources and a list of the author’s scientific publications on the dissertation topic. The dissertation volume is 116 text pages and 14 pages of annexes.

Acknowledgements

The author of the dissertation would like to thank dear friends prof. dr. V. Jūrėnas and habil. dr. V. Garalienė, as well as prof. dr. V. Veikutis for scientific advice in the course of the preparation of the doctoral dissertation.

2. PROBLEM ANALYSIS AND FORMULATION OF THE TASKS

2.1. The Blood Circulatory System of the Human and Anatomy of the Vessel

The blood circulatory system (also known as the cardiovascular system) delivers nutrients and oxygen to all the cells of the body. It is comprised of the heart and the blood vessels that are deployed throughout the entire body. The arteries carry blood away from the heart, whereas the veins return it back to the heart [9]. The system of blood vessels might be compared to a tree: the main artery (called the aorta) being similar to a tree trunk branches into large arteries that further lead to smaller and smaller vessels. The smallest arteries end in a network of tiny vessels that comprise the so-called capillary network.

The human body contains two blood circulatory systems that are interconnected: the systemic circulation provides organs, tissues and cells with blood that carries oxygen as well as other vital substances. The pulmonary circulation is where the fresh oxygen enters the blood as we breathe in, and simultaneously carbon dioxide is released from the blood [10].

Blood starts circulating when the heart relaxes between two heartbeats: blood flows from both atria (the upper two chambers of the heart) into the ventricles (the lower two chambers) which then expand. The phase that follows is called the ejection period. During the ejection period, both ventricles pump the blood into the large arteries.

In the systemic circulation, the left ventricle pumps oxygen-rich blood into the main artery (aorta). The blood flows from the main artery to larger arteries first, then to smaller arteries, and, finally, reaches the capillary network [11]. In the capillary network, oxygen, nutrients and other vital substances are released from the blood, and carbon dioxide as well as waste substances are taken on. The blood, being low in oxygen, is now collected in veins and flows to the right atrium and into the right ventricle [12].

Then, pulmonary circulation starts: the right ventricle pumps the blood low in oxygen into the pulmonary artery which branches off into smaller and smaller arteries and capillaries. The capillaries form a fine network around the pulmonary vesicles (grape-like air sacs at the end of the airways). This is where carbon dioxide is released from the blood into the air contained in the pulmonary vesicles, and fresh oxygen is supplied to the bloodstream. When we make a breath out, carbon dioxide is removed from our body [12]. Oxygen-rich blood flows through the pulmonary vein and the left atrium into the left ventricle. With the next heart beat, a new cycle of systemic blood circulation starts.

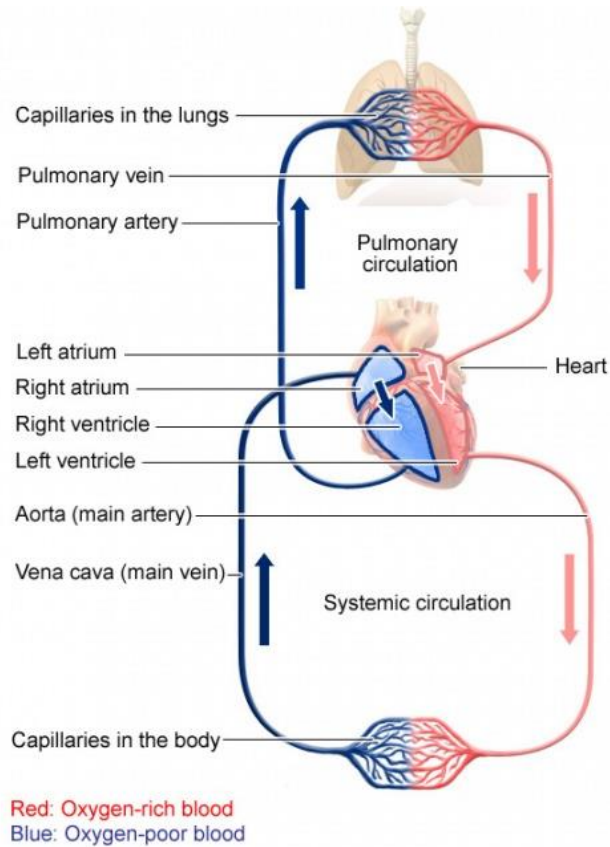


Fig. 1. The cardiovascular system [13].

All the blood vessels can be grouped into three major types as follows: arteries, capillaries, and veins. As the heart contracts, it forces blood to leave the ventricles and flow into the large arteries. Blood then moves further to smaller arteries successively, until it finally reaches the smallest branches, the so-called arterioles, which feed into the capillary beds of organs and tissues. Blood drains from the capillaries into venules, the smallest veins, and then into larger veins that merge and ultimately empty into the heart. If all the blood vessels contained in the human body were stretched out, these would be 100,000 km long [14].

Arteries carry blood away from the heart while forming smaller and smaller divisions, thus arteries are said to ‘branch’. In contrast, veins carry blood towards the heart and are said to ‘merge’ into larger and larger vessels approaching the heart. In the systemic blood circulation, arteries always carry oxygen-rich blood, and veins always carry blood low in oxygen [15]. The opposite is true for the pulmonary circulation. The arteries, defined as the vessels leading away from the heart, carry blood low in oxygen to the lungs; whereas the veins carry oxygen-rich blood from the lungs to the heart. Capillaries are the only blood vessels that have intimate contact with the tissue cells in the human body. Consequently, they are responsible for serving

cellular needs. Any exchanges between the blood and tissue cells occur primarily through the capillary walls that are thin.

The walls of any blood vessel (except for the smallest ones) have three layers, the so-called tunics, that surround a central blood-containing space, which is referred to as the vessel lumen [16].

The innermost tunic is called the *tunica intima*. The *tunica intima* contains the endothelium which is the simple squamous epithelium, and it lines the lumen of all the vessels. The endothelium is continuous with the endocardial lining of the heart. Its flat cells fit closely together thus forming a slippery surface that minimizes friction so that blood could move smoothly through the lumen. In vessels larger than 1 mm in diameter, a subendothelial layer consisting of a basement membrane and a loose connective tissue supports the endothelium [17].

The middle tunic, called the *tunica media*, is mainly circularly arranged smooth muscle cells and sheets of elastin. The activity of the smooth muscle is regulated by sympathetic vasomotor nerve fibres of the autonomic nervous system and chemicals. Depending on the body's needs at any given moment, regulation causes either vasoconstriction (decrease in the lumen diameter) or vasodilatation (increase in the lumen diameter). The activities of the *tunica media* are critical for the regulation of the circulatory system because even very small changes in the vessel diameter have a huge influence on the blood flow and the blood pressure. Generally, the *tunica media* is the bulkiest layer in arteries, and it bears the chief responsibility for maintaining the blood pressure and the proper blood circulation [18].

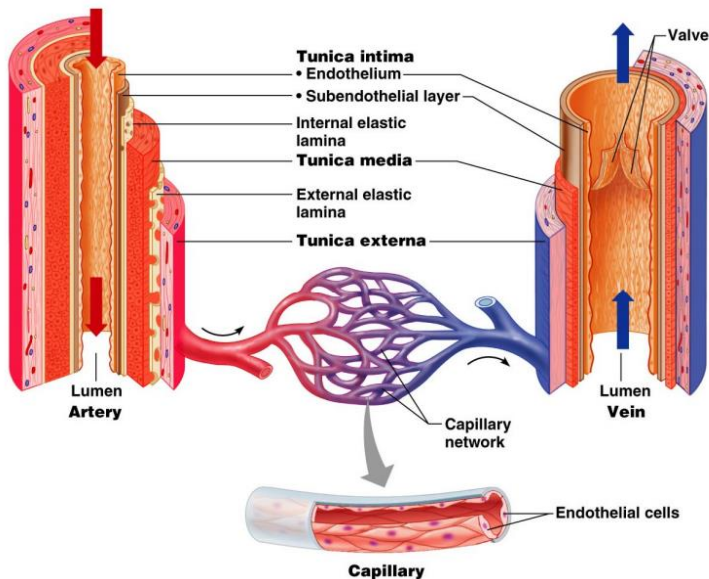


Fig. 2. Generalized Structure of Blood Vessels [18].

The outer layer of a blood vessel wall is called the *tunica externa*. It is mainly comprised of collagen fibres that protect and reinforce the vessel, and anchor it to the

surrounding structures [19]. The *tunica externa* contains nerve fibres, lymphatic vessels, and elastic fibres (in large veins). In large vessels, the *tunica externa* contains a structure known as the *vasa vasorum* – literally, ‘vessels of vessels’ – that nourish the external tissues of the blood vessel wall. The interior layers of blood vessels receive nutrients directly from the blood carried in the lumen.

2.2. Vascular Disease

Vascular Disease is the term describing blood vessel diseases. When a disease occurs in the arteries, it is called an arterial disease. Veins return blood back to the heart from all the parts of the body. When a disease occurs in the veins, it is called a venous disease.

Atherosclerosis is a disease, in which, plaque tends to build up on the inside of the arteries (Fig. 3). Over time, this plaque build-up hardens around the artery walls thus narrowing the blood flow to the organs and various parts of the body. As organs do not receive blood rich enough in oxygen, they cannot function properly. Furthermore, blood clots often form around plaques. Sometimes, the plaque or a clot can break loose and travel to smaller arteries where it blocks the blood flow. In addition, a plaque can rupture [20]. Such blood flow blockages and plaque ruptures can lead to serious problems including, but not limited to, heart attacks, strokes and, in the worst-case scenario, death. There are many factors that contribute to causing atherosclerosis, such as smoking, high cholesterol level, diabetes, etc. Atherosclerosis can affect almost any artery. In many cases, it involves multiple arteries at the same time. It is commonly found in the coronary or heart arteries, the carotid or neck arteries, and the leg arteries. Atherosclerosis can also occur in the aorta, the largest artery of the body responsible for carrying blood from the heart to the chest, abdomen and legs. In a severe case of atherosclerosis, an artery may become fully blocked, resulting in ischemia – a restriction in oxygenated blood supply to any muscle group, organ or tissue. It is very common for ischemia to result in heart attacks and strokes [21].

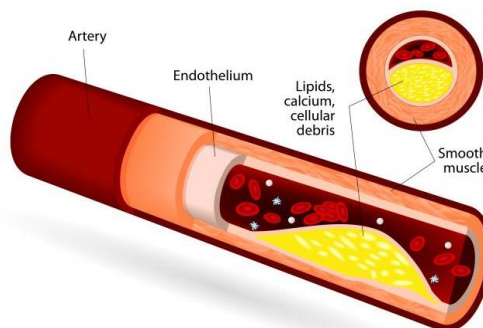


Fig. 3. Atherosclerosis [22].

Some of the diseases that can stem from atherosclerosis are as follows [23]:

- Carotid Artery Disease is diagnosed when the major arteries in the neck, called the carotid arteries, become narrowed or blocked. These arteries are responsible for the blood supply to the brain. Significant artery narrowing leads to the increased risk of plaque or a clot breaking loose and travelling to the brain which will ultimately cause a stroke;
- Coronary Artery Disease (CAD) occurs when plaque builds up inside the coronary or heart arteries. Narrowing or full blockage of coronary arteries prevents oxygen-rich blood from reaching the heart. Sometimes, this causes chest pain which is called angina (pronounced as *an-JI-nuh* or *AN-juh-nuh*); however, in severe cases, it results in a type of heart attack called myocardial infarction;
- Mesenteric Artery Disease refers to the condition in which the major arteries carrying blood to the intestines become narrowed or blocked. Its symptoms, among others, include abdominal pain after eating, blood in the stool, and loss of weight.
- Peripheral Arterial Disease (PAD) is diagnosed when the leg arteries become narrowed or blocked. Such a condition is also known as poor circulation or peripheral vascular disease. In case of insufficient blood flow to the legs and feet, patients diagnosed with PAD can experience leg pain, ulcers or sores. In some cases, patients with PAD suffer no symptoms whatsoever. However, in extremely severe cases, peripheral arterial disease, also known as a critical limb ischemia, can even require an amputation of the limb or at least a part of it.
- Renovascular Disease is a progressive condition in which renal arteries responsible for the blood flow to the kidneys become narrowed or blocked. Atherosclerosis of renal arteries can cause high blood pressure or kidney failure.
- Vertebrobasilar Insufficiency is a disorder characterized by poor blood flow to the posterior portion of the brain. Symptoms of narrowed vertebral arteries may include blurred or double vision, dizziness, and lack or loss of coordination or imbalance. Vertebrobasilar insufficiency can also cause drop attacks, or sudden and spontaneous falls while standing or walking.

Aneurysm is a balloon-like bulge in the artery which occurs due to a weakening in the artery wall (Fig. 4). In most of the cases, aneurysms occur in the aorta, the largest artery in the body, carrying blood from the heart to the chest, abdomen and legs. However, aneurysms can also occur in brain and leg arteries. A ruptured aneurysm is an emergency which requires immediate medical attention. Progressive weakening of the aortic wall causes the so-called Aortic Aneurysm. This may cause bulging or ballooning of the vessel, which, if not treated properly, may continue to grow and even rupture. An aneurysm in the abdomen is known as abdominal aortic aneurysm (AAA, or triple A), whereas an aneurysm in the chest is called a thoracic aortic aneurysm [23].

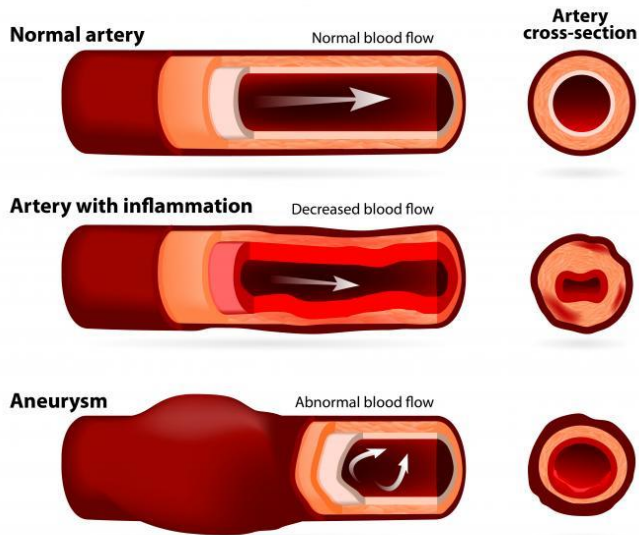


Fig. 4. An Aneurysm [23].

Venous Thrombosis is a blood clot that forms in any of the veins (Fig. 5). Venous clots can block the blood flow through the vein, or can also travel to any part of the body. There are many factors that are considered to increase the risk of developing venous clots including, but not limited to, various leg traumas, injuries to the veins, a recent surgery or hospitalization, being overweight, and prolonged body immobility, such as a long airplane ride or bed rest [24]. Taking birth control pills, having cancer, and even pregnancy can also lead to the increased risk of blood clot formation in the veins. Moreover, people who once have had a blood clot face a higher chance of having another one. Clots can occur in both the arm and leg veins, however, it is more common for blood clots to form in legs. In most severe cases, blood clots are treated with blood thinner drugs called anticoagulants. Anticoagulant drugs decrease the blood's ability to clot to a controlled degree. They prevent clots from getting bigger, and also prevent the formation of new ones [25].

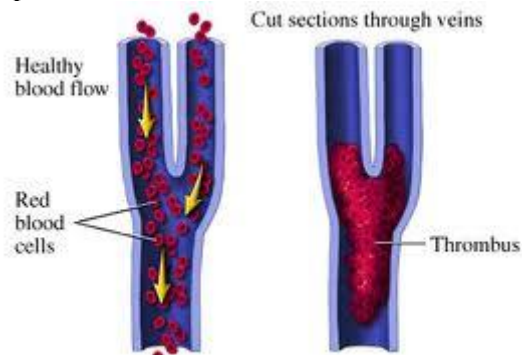


Fig. 5. Venous Thrombosis [26].

Deep Vein Thrombosis (DVT) is the condition in which blood clots form within the deep veins of the arms or legs (Fig. 6). As for the legs, DVT is diagnosed when a clot forms in one of the deep calf or thigh veins while blocking blood flow and causing pressure to build up in the vein. Symptoms include pain and swelling in one or both legs. DVT is rather rarely found in the arms; however, it occurs most often in the large veins called the axillary and subclavian veins. Symptoms of arm DVT include swelled and painful arms, prominent veins that can be clearly seen through the skin, and changes in the skin color [27].

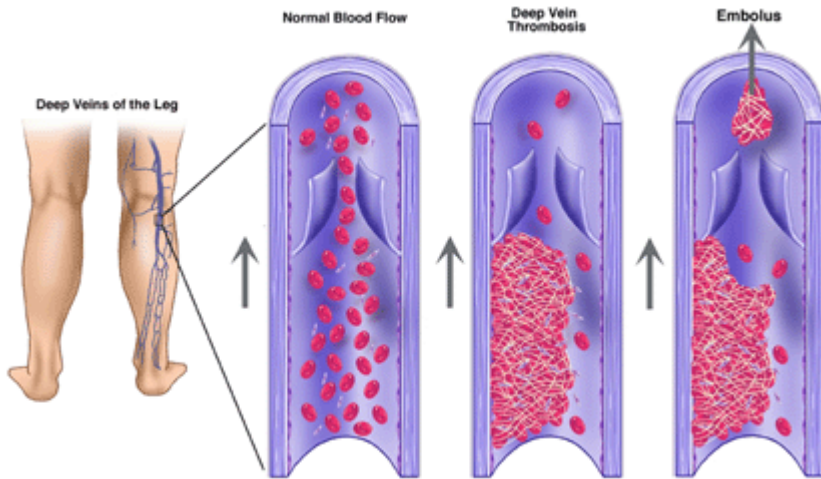


Fig. 6. Deep Vein Thrombosis [28].

DVT can lead to a serious complication called *Pulmonary Embolism (PE)*. It is diagnosed when some or all of the DVT breaks loose from its original location in a vein and is moved through the heart into the lungs. The most common symptoms of PE include chest pain, difficulty breathing, and heart palpitations or a racing heartbeat. Again, pulmonary embolism is an emergency and requires immediate medical attention [29].

Superficial Vein Thrombosis (SVT) refers to a blood clot in a surface vein of the arm or the leg, close to the skin. Blockages in the superficial veins are not as serious as those in the deep veins, but they may still cause swelling and discomfort [30].

Veins return blood from the arms and legs back to the heart in order for the lungs to resupply it with oxygen. Veins contain special valves that prevent blood from flowing in the opposite direction. In case these valves fail to work properly, blood can flow backwards down the veins and pool in the lower leg. This may cause veins to enlarge and can further result in leg swelling, aching and burning, skin color changes as well as leg ulcers [31].

Varicose Veins refer to the visibly bulging veins that mildly protrude or do not protrude above skin in the thigh or calf. Generally, varicose veins are larger than 3 mm in diameter. They develop due to the weakness of the vein wall and because the valves no longer function as they are supposed to. Sometimes, varicose veins form entire

families. There are two other conditions that are often mistakenly taken for varicose veins, namely, spider veins and reticular veins. Spider veins, also called teleangiectasia, refer to the tiny veins that can be easily seen but cannot be felt. Reticular veins are larger than spider veins but smaller than varicose veins [32].

Lymphedema is a disorder of the lymphatic blood vessels which leads to *Lymphedema* is a disorder of the lymphatic blood vessels that leads to severe swelling of one or both of the legs or arms. In some cases, lymphedema is caused by some damage of the lymphatic vessels, for example, this may happen among women who have received surgery in the course of the treatment for breast cancer. Sometimes, lymphedema is found to have run in families and is also diagnosed in children or young adults [33].

Vasculitis is an inflammation of the blood vessels that occurs when the body's immune system mistakenly attacks the blood vessels causing them to become inflamed. As a result of such inflammation, the blood vessels can become damaged, and this may lead to the narrowing or blockage of blood flow or aneurysms of the blood vessels. Vasculitis can affect any of the body's blood vessels [34].

Raynaud's phenomenon refers to a disorder in which arteries tend to go into spasm for brief periods. The contraction or narrowing of the blood vessels (called *vasospasm*) leads to decreased blood flow to the fingers and toes. In some cases, it can affect the nose, ears, nipples and lips. Due to the reduced blood flow, the color of the affected area may change. For example, some patients report that their fingers turn blue, white and/or red. It is common for a vasospasm to occur in response to cold, but it can also be triggered by stress. Mild Raynaud's phenomenon is commonly found among young women. Although severe Raynaud's phenomenon is rare, it may even lead to ischemia of the hands or feet and non-healing sores [35].

Compression Syndromes occur when blood vessels are narrowed or compressed by bones, muscle, or other body tissues. With Thoracic Outlet Syndrome (TOS), blood vessels and nerves of the arms are compressed as they leave the chest cavity by the surrounding bones and muscles. If the nerves are affected, TOS may cause pain or numbness in the arms with certain movements. If the blood vessels are affected, it may cause arm swelling or a blood clot. With Popliteal Entrapment Syndrome, the compression of the popliteal artery or the popliteal vein at the back of the knee by the calf muscles may cause leg pain with exercise or a blood clot in the leg [36].

Some of the diseases listed in Chapter 1.3 are healed while applying ultrasound and the process that ultrasound creates, i.e., cavitation. Therefore, it is important to understand how ultrasound is applied in the field of modern medicine.

2.3. Application of Ultrasound in Medicine

Ultrasound refers to a high frequency (0.02 to 200 MHz) acoustic wave that transfers energy in a gas, liquid or solid medium [37]. In gases and liquids, the longitudinal waves of sound mainly propagate, whereas, in solid bodies, both transverse and longitudinal sound waves can be transmitted. The speed of ultrasound transmission depends on the density and elasticity or the stiffness of the medium. The ultrasonic wave occurs due to the rhythmic oscillations of the particles (molecules and

atoms) in the medium that cause the medium to get denser and to bend (due to particles getting closer and farther from each other, respectively), because of which, the pressure tends to increase and decrease, respectively. The vibrations at frequencies higher than 20 kHz are called ultrasonic, or the ultrasound. When propagating, the sound pressure oscillations transfer kinetic energy [38]. The ultrasound energy absorbed by tissues is converted into heat. The ultrasound absorption (conversion into heat) is described by means of the Thermal Index (TI). When $TI=1$, the temperature in the medium under consideration rises by 1 degree, when $TI = n$, by n degrees. TI is mainly dependent on the characteristics of the tissue.

The energy transported in an ultrasound wave is usually characterized by acoustic intensity I which is defined as the energy transmitted per time unit (usually, 1 s) and per area unit (usually, 1 cm^2) in the direction normal to the area under consideration. In the field of medical ultrasound, the intensity is measured in $\text{W} \cdot \text{cm}^{-2}$.

In general, the ultrasound can be either continuous or pulsed. The continuous ultrasound is the regime in which the generated ultrasonic waves are propagating at the constant amplitude, with no pauses, under constant frequency. On the other hand, pulsed ultrasound is the intermittent regime, involving pauses, however a recurrent one. Ultrasound working regimes are shown in Fig. 7.

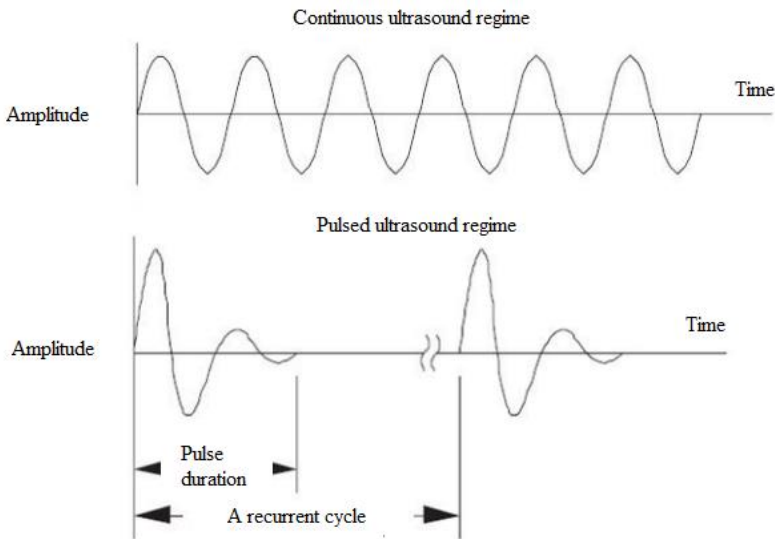


Fig. 7. Continuous and pulsed ultrasound regimes [39].

Ultrasonic energy can be a potent means enabling to achieve the desired biological effects. Having sufficient knowledge of the etiology and exosimetry, it is possible to plan some bioeffects for therapeutic purposes or to avoid other ones in diagnostic applications [40]. As for the therapy, ultrasound can induce the desired effects not only by the way of heating but also through certain non-thermal

mechanisms such as gas body activation, ultrasonic cavitation, mechanical stress, and other undetermined non-thermal processes [41].

Ultrasound-induced heating stems from the absorption of ultrasonic energy by biological tissue. By using ultrasound for diagnostic purposes, the temperature elevations and the potential for bioeffects are kept relatively low or negligible [42] by carefully following the described indications for use while applying the ALARA (As Low As Reasonably Achievable) principle, limited temporal average intensities, and generally short exposure times. On the other hand, therapeutic applications of ultrasonic heating therefore either involve longer durations of heating with unfocused beams or use higher-intensity (than for diagnostic purposes) focused ultrasound. The use of unfocused heating, for example, in physical therapy, to treat highly absorbing tissues, such as a bone or a tendon, can be moderated to produce enhanced healing without an injury [43]. Alternatively, the heat can be concentrated by focused beams until the tissue has been coagulated for the purpose of tissue ablation. Ultrasonic heating, which can lead to irreversible tissue changes, follows an inverse time-temperature relationship. Depending on the temperature gradients, the effects of ultrasound exposure can include mild heating, coagulative or liquefactive necrosis, tissue vaporization, or all the three effects [44].

Recently, a series of tests have been undertaken for the purpose of evaluating the blood vessel endothelial function because scholarly studies have shown that endothelial dysfunction can be considered to be an independent risk factor in patients with the suspected coronary insufficiency [45, 46]. A damaged endothelium is no longer able to release endothelium-dependent vascular smooth muscle relaxing factors. For this reason, it is still necessary to explore various tools that can potentially restore the endothelial function. Currently, ultrasound has also been widely applied in body's circular system diagnostics. However, there is lack of researches regarding the ultrasound's effect on the physiological functions of endothelium and the smooth muscles associated with the vessel contraction and relaxation.

2.4. The Process of Cavitation

Cavitation is defined as the formation of vapor cavities and small liquid-free zones (also named as 'voids') within a liquid body. There are a number of ways to force a cavitation to appear. The aim of this chapter is to describe the most common of these techniques.

2.4.1. Acoustic Cavitation

Acoustic cavitation refers to the formation (expansion) of bubbles during the negative phase of the acoustic cycle when liquid pressure is below the critical limit. When acoustic pressure achieves a positive value, the expansion of a bubble is slowed down, and, finally, the bubble bursts.

The term 'stable cavitation' refers to the condition in which the speed of bubble expansion under negative pressure is equal to the period of collapse in the positive portion of the acoustic cycle [47]. It is worth noting that the formation of stable

bubbles is not influenced by the process when the vibration-induced pressure field increases in volume more than it contracts after bursting.

2.4.2. Tension

The simplest way to stretch out a liquid is to pull some portion of it. Such tension of a liquid can be influenced by its own weight. When studying the effect of the liquid weight, in 1962, Huygens [48] was the first to record the existence of the negative pressure in a liquid. On the one side, an open column semi-filled with water was placed into a larger tank, and then all the remaining air was sucked out of it. This led to the observation that when the air above the larger tank has been sucked out, the water remains 'pending' in the smaller container turned upside-down. At the top of the water column of height h , $P_{\text{sat}} - \rho gh$, where ρ represents the density of water, and g is the force of the Earth's gravity.

When an air bubble is injected into a water column, the bubble shall rise upwards, and the water column falls down, respectively. The experiment was afterwards repeated; however, the container was filled with mercury instead of water.

Other ways to 'pull' a liquid also exist, and one of them is to mechanically increase the liquid volume by using special bellows or to heat it after compressing, and then to remove the pressing element of the apparatus. These two ways were the most popular ones for a rather long period of time while making bubble chambers where particles were recorded as carrying an extremely high energy and causing cavitation.

2.4.3. The Method of Bertholet

While using the method of Bertholet, to induce cavitation, it requires a container to be filled with water and then sealed. If a bubble of gas (air) persists, the entire structure is heated until the gas bubble has dissolved completely. The density of the liquid is found based on the temperature of bubble dissolution T_d .

Afterwards, the container is cooled down while decreasing its pressure to the negative value (i.e., cooled down to the sufficiently low temperature). At temperature T_{cav} , cavitation occurs, and the fluid restores its original condition (the ambient temperature). Bertholet used the cavitation-induced change in volume for measuring the size of the cavitation bubble.

2.4.4. Inclusions

Water contained in extremely small (10 to 100 micrometers) vessels is also found in the nature, often trapped inside various crystals. Roedder used such microscopic fluid inclusions for studying the equilibrium of ice crystals and water (fluid). His research started from a fluid with vapor inclusion. When freezing inclusions, vapor was found to disappear due to the increase in the ice volume. When such a specimen was heated, the vapor was observed not to recover, and the negative pressure was found to increase with the system approaching the melting point.

At a later date, the method of Bertholet was applied while using synthetic materials as inclusions instead of vapor. Primarily, the experiments involved salt

solutions of low concentrations [49]. Crystals of quartz, calcite and fluorite were processed in distilled water heated to 300° to 400°. Afterwards, cleft crystals were placed into tubes made of a silver and lead compound together with the known amount of absolutely pure water. The entire container was then vacuumed. During vacuuming, any fractures present in crystals were filled with water depending on the temperature and pressure applied during the process.

Hereafter, the specimens were studied by using the method of Bertholet. The water bubbles remaining inside the inclusions were observed to disappear when heated to temperature T_d . When freezing the specimen, the water parameters changed gradually until the occurrence of cavitation. The derivation of P_{cav} parameter was based on the EOS multi-parameter dependent on the pressure of the stable fluid.

2.4.5. Centrifuging

For the first time applied by Reynolds, this method involves rotation of the water present inside a specific container at a high speed [50]. Negative pressure is created on its axis due to eccentric power.

$$P = P_o - \frac{1}{2} \rho \omega^2 r^2 \quad (1.1)$$

Where P_o denotes the pressure outside the container; ρ represents the water density.

Ultrasonic cavitation and gas body activation are closely related mechanisms that depend on the rarefactional pressure amplitude of ultrasonic waves. Ultrasound transmitted into a tissue may have rarefactional pressure amplitudes of several megapascals (Fig. 8). This tensile stress is supported by the medium. For example, a 2 MPa rarefactional pressure, which is common even for diagnostic ultrasound, represents a negative tension 20 times the atmospheric pressure (i.e., 0.1 MPa) [51]. This high rarefactional pressure can act to initiate cavitation activity in a tissue when suitable cavitation nuclei are present or directly induce the pulsation of pre-existing gas bodies, such as those occurring in lungs and intestines, or with ultrasound contrast agents. Cavitation and gas body activation primarily cause local tissue injury in the immediate vicinity of the cavitation activity, including cell death and the hemorrhage of blood vessels [52].

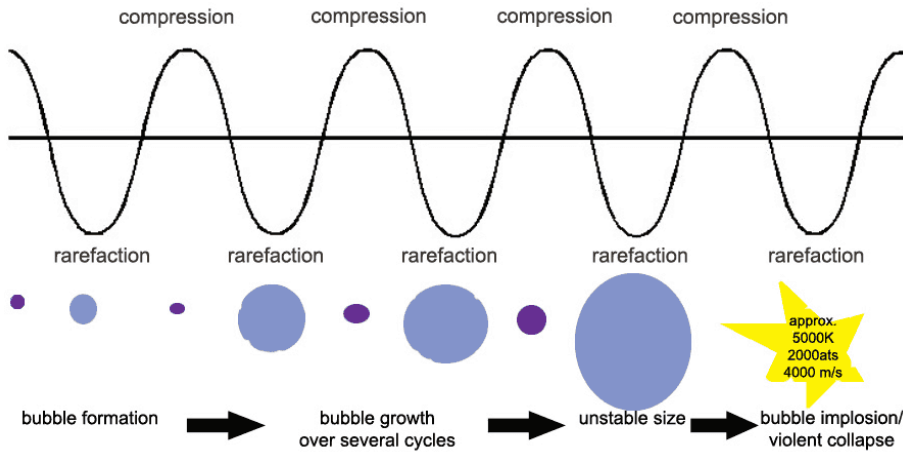


Fig. 8. Ultrasonic cavitation [51].

Other potential mechanisms for biological effects of ultrasound include the direct action of the compressive, tensile, and shear stresses. In addition, there are second-order phenomena that depend on the transmitted ultrasonic energy. They include radiation pressure, forces on particles, and acoustic streaming. What regards the high-power or high-amplitude ultrasound which is intended for therapy, several different mechanisms may be contributing simultaneously to the total biological effect of the treatment. In addition to direct physical mechanisms for bio-effects, there are secondary biological, physical, and physiologic mechanisms that cause further effects on the organism. Some examples are vasoconstriction, ischemia, extravasation, reperfusion injury, and immune responses [53]. In some cases, these secondary effects tend to be greater than the direct insult from the ultrasound.

2.5. Dynamics of the Cavitation Bubble

2.5.1. Dynamics of the Spherical Bubble

Investigation of spherical cavitation bubbles has no direct implications for the attempts to explain the cavitation erosion as bubbles present in sufficient vicinity to the walls to cause harm will always collapse aspherically. Despite that, such investigation provides a sound basis for interpreting the data obtained for asymmetrical collapse of bubbles in the non-Newtonian fluids. Up to date, it is the only way available for comparison of the test results and the theory.

A simple way to generate a single bubble in the fluid is to focus a low-pulsed laser light to a specific point on the fluid surface. Depending on the size of the focus point, the laser transverse mode, the pulse duration and the intensity of the light, a single drop or several small ‘drops’ of the fluid get rapidly heated (in nano-, pico- and femto-seconds).

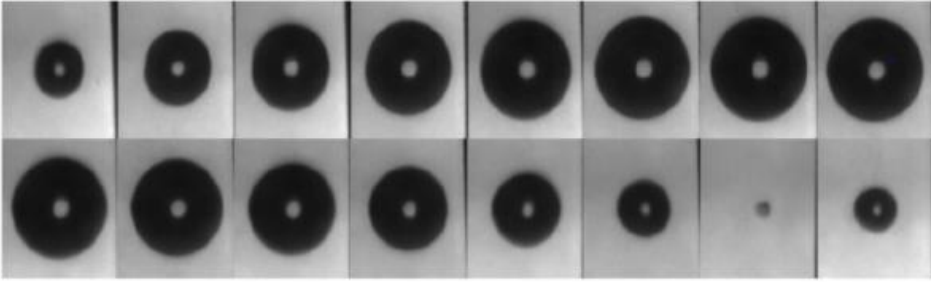


Fig. 9. Dynamics of the cavitation bubble in water and the respective pressure signal measured at a distance of 10 mm to the laser focus when laser pulse energy $EL = 10\text{mJ}$.

Fig. 9 shows a high-speed photography image of the dynamics of a bubble generated by a laser in water as well as the respective hydrophonic signals at a distance of $r = 10\text{ mm}$ to the laser focus when the laser pulse energy equals $EL = 10\text{mJ}$. The interval time between shots is $20\ \mu\text{s}$. The laser light is emitted from below. The hydrophonic signal is recorded at the same time as the images showed in the above figure. Over a certain period of time, the movement of the laser wave causes the formation of a shock wave. The resulting difference between the hydrostatic and the dropping internal pressure of the bubble determines a significant increase in the volume of the bubble, and finally leads to its burst. During this process, the kinetic energy of the fluid is converted into the potential energy of the bursting bubble.

The energy contained in the bubble is described as follows:

$$E_B = \frac{4\pi}{3}(p_\infty - p_v)R_{\max}^3 \quad (1.2)$$

It is dependent on the radius and maximum size R_{\max} of the bubble as well as on the difference between the hydrostatic pressure and vapor pressure p_v .

The bubble expanded to its maximum size will collapse again due to the static pressure of the surrounding fluid. The volume of the bubble then decreases to a very small size; however, at the moment of its collapse, extremely high pressure is created that may exceed even 1 GPa [54].

2.5.2. Dynamics of Aspherical Bubble

The dynamics of the bubbles being generated is mainly influenced by the physical limits of the bubble movement and the features of the fluid within which this bubble occurs. When a bubble is generated in the vicinity of a wall (a physical barrier), its burst will be asymmetric and linked to the formation of several high-speed water streams generated around it where the entire energy of the bubble is concentrated [55].

At the moment of the bubble burst, such water streams strike the wall which is present in close vicinity. When a bubble happens to burst in between two walls standing next to each other, they are struck by two such water streams.

2.6. Patented Ultrasound Devices for the Intravascular Thrombus Decomposition

Thrombolysis accelerated by ultrasound involves the breaking down or ‘melting’ of blood clots that can be found in the leg arteries or veins. In the past, it was common practice to treat blood clots by simply giving blood thinners to be consumed by the patient either orally or injected intravenously. As a result, over two to four months, those blood clots can be expected to disappear. However, recently, new methodologies have been under development that use ultrasound energy along with thrombolytics to facilitate and accelerate the process of thrombolysis.

A blood clot is generally made up of different elements, such as fibrin, weaved together into a net-like structure. Acoustic energy is known to generate a pressure wave that enables the disruption of the cross-linking of the fibrin. The ultrasound energy also helps loosening up the fibrin cross-links while creating a way for the thrombolytic to get into the clot. The ultrasound energy does not actually break up the clot. It only alters the shape of the fibrin network. As a result, the clot becomes more porous, which makes it easier for the drug to get inside the clot and have a more powerful effect there instead of just being dripped in around it (unfortunately, that is how the old catheter systems function). In medical practice, various catheters have been used for delivering the drug for many years, but the only reason they were good for was just getting the drug to the leg. Meanwhile, ultrasound-accelerated thrombolysis allows the drug to get into the clot directly.

Ultrasound system with pathfinding guidewire. A system is designed to enable the crossing of completely occluded blood vessels. The system is comprised of a pathfinding guidewire that is coupled to the distal end of an ultrasound catheter. The distal section of the pathfinding guidewire functions as a narrow extension of the distal end of the catheter. This way, the ultrasound energy is effectively transmitted, which allows to traverse the occlusions [56]. Once the distal section of the guidewire has successfully crossed the occlusion, the distal end of the catheter can be advanced over the distal section of the guidewire and against the occlusion to remove the occlusion (see Fig. 10).

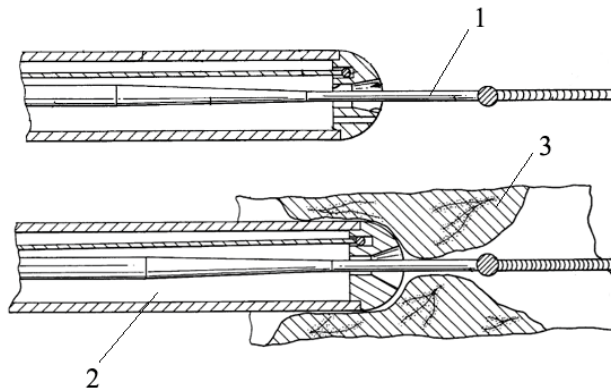


Fig. 10. An ultrasound system with the pathfinding guidewire, where 1 is the guidewire; 2 is the waveguide; 3 is an occluded blood vessel [56].

Ultrasonic transmission guidewire. The ultrasonic angioplasty transmission guidewire has reduced the cross-sectional diameter at some areas in order to improve its flexibility and to compensate for the degradation of the longitudinal displacement stemming from acoustic losses along the length of the guidewire. The core of a guidewire is made of ultrasonic transmission material. The guidewire also has a non-metallic outer jacket which surrounds the usable portion of the elongated shaft (see Fig. 11). The outer jacket is formed of a shrink tubing. Threads are disposed at the proximal end. These threads are configured to be connected to a connecting device for an ultrasound transducer. The distal end has a smooth ball tip in order to avoid any traumas during the application of ultrasound energy to the biological tissue [57]. In one embodiment, the guidewire is formed of stainless steel, whereas, in another one, it is formed at least partially of a super-elastic metal alloy, and in one case it is formed at least partially of a shape memory alloy that exhibits super-elastic properties when in its martensitic state. In one preferred embodiment, the guidewire is formed of a nickel and titanium alloy.

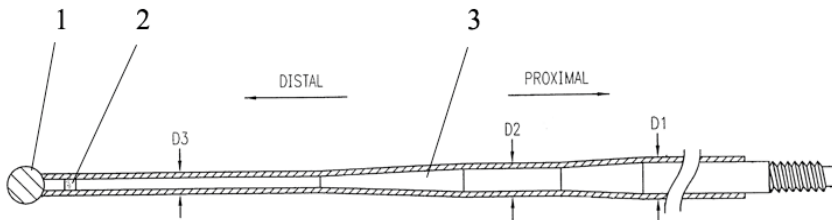


Fig. 11. Ultrasonic transmission guide wire, where 1 is the distal head; 2 is the radio opaque marker for use in locating the distal tip during *in vivo* procedures; 3 is the ultrasonic transmission wire [57].

Guidewire system for RF recanalization of vascular blockages. A system for recanalizing an occluded blood vessel is comprised of a centering catheter employed to center an ablative guide wire within the blood vessel as the guidewire traverses the occlusion. The centering catheter is made of a catheter body with an operative lumen through which the ablative guidewire is slidingly disposed. The centering catheter further includes a distally disposed centering mechanism that, when activated, centers the ablative guidewire within the blood vessel as it traverses the occlusion. The centering mechanism can involve various embodiments including a single inflatable balloon or a segmented inflatable balloon which is in fluid communication with the inflation lumen. An airless preparation lumen may be disposed within the inflation lumen to make it easier to center the catheter preparation [58]. The ablative guidewire is covered with insulation that is preferably made of heat shrink tubing which is stretched prior to or concurrently with the heating process. The ablative guidewire includes a distal ablation tip of the atraumatic structure and at least one discontinuous feature for creating high current densities to make tissue ablation more efficient (see Fig. 12).

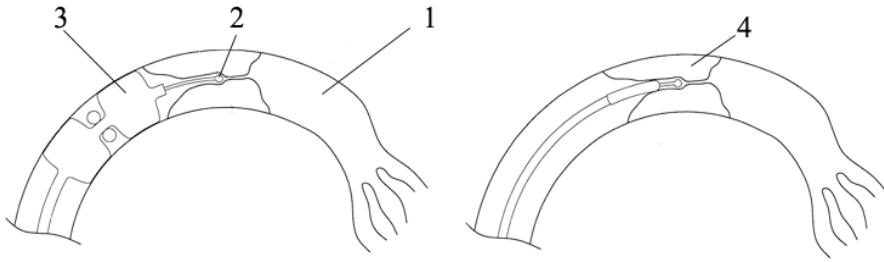


Fig. 12. A guide wire system for RF recanalization of vascular blockages, where 1 is a blood vessel; 2 is a waveguide; 3 is a balloon; 4 is the targeted thrombus [58].

Ultrasonic resonator (Fig. 13). An ultrasonic resonator is comprised of a wire member with an elongated shaft that has a proximal end and a distal end. The filler material is disposed within the proximal end. A crimp screw is used with an annular end and a threaded end. Its annular end is adapted to receive and fixedly secure the proximal end of the wire member. The annular end being crimped after the proximal end of the wire member is inserted within the annular end of the crimp screw. The resonator includes an ultrasonic transducer specifically adapted to receive the threaded end of the crimp screw. The ultrasonic transducer is operatively connected to an ultrasonic generator [59].

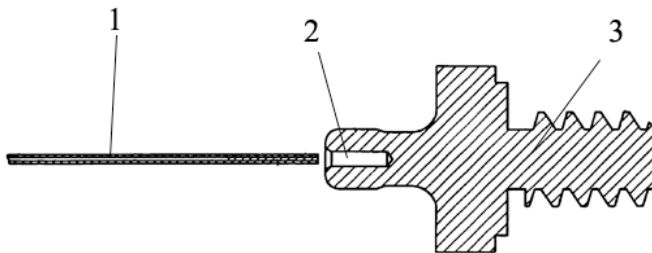


Fig. 13. Ultrasonic resonator, where 1 is the waveguide; 2 is the hole for the waveguide; 3 is the crimp screw [59].

Apparatus and method for an ultrasonic medical device with improved visibility in imaging procedures. The invention under consideration here refers to the apparatus and the operation method for an ultrasonic medical device with improved visibility in imaging procedures. This medical device has an elongated probe which at predetermined location(s) has a material of high radiopacity. The material of high radiopacity is able to withstand series of vibrations of the elongated probe [60]. Once the probe has been inserted into a body, this material of high radiopacity allows the elongated probe to be visualized in imaging procedures (see Fig. 14). The present invention covers a method of improved visibility of an ultrasonic medical device during a medical procedure by engaging a material of high radiopacity into a small diameter elongated probe wherein the material of high radiopacity engages the probe in at least one predetermined location.

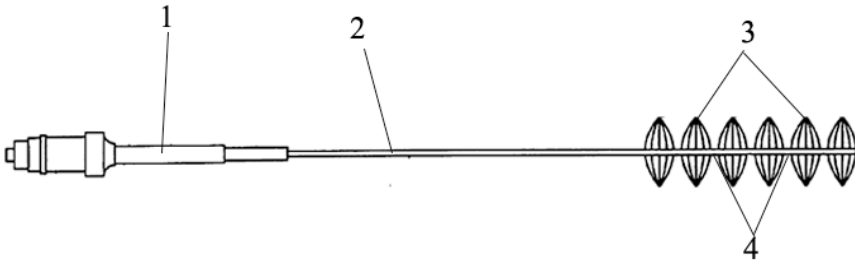


Fig. 14. Apparatus and method for an ultrasonic medical device with improved visibility in imaging procedures, where 1 is the coupling; 2 is the wireguide; 3 are the anti-nodes; 4 are the nodes [60].

Steerable ultrasound catheter. Ultrasound catheter devices and respective application methods offer enhanced disruption of blood vessel blockages. Such devices usually involve an elongated flexible catheter body with one or more lumens, an ultrasound transmission member extending longitudinally through the catheter body lumen, and a distal head coupled with the transmission member that is positioned adjacent to the distal end of the catheter body for disrupting occlusions (see Fig. 15). More advanced ultrasound catheters feature catheter bodies and ultrasound transmission members with increased distal flexibility, guidewire tubes allowing contact between the guidewire and the ultrasound transmission member, distal heads with improved guidewire lumens, and torquable proximal housings to ensure enhanced disruption of vascular occlusions [61].

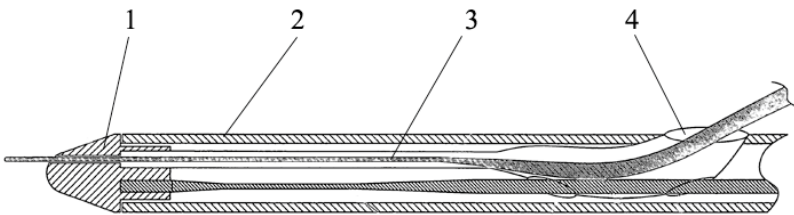


Fig. 15. Steerable ultrasound catheter, where 1 is the guidewire; 2 is the wall of the guidewire; 3 is the waveguide; 4 is the hall for the waveguide [61].

Apparatus and method for an ultrasonic medical device operating in torsional and transverse modes. This invention offers an apparatus and a method for an ultrasonic medical device intended to operate in torsional and transverse modes. An ultrasonic medical device has an ultrasonic probe which is placed in communication with a biological material. Once the ultrasonic energy source has been activated, it produces an electrical signal that drives a transducer to produce a torsional vibration of the ultrasonic probe [62]. As a result, the torsional vibration produces a component of force in a transverse direction relative to the longitudinal axis of the ultrasonic probe, thereby exciting transverse vibration along the longitudinal axis. This vibration causes the ultrasonic probe to undergo both torsional vibration and transverse

vibration, both of which concurrently cause cavitation in a medium surrounding the ultrasonic probe to ablate the biological material (Fig. 16).

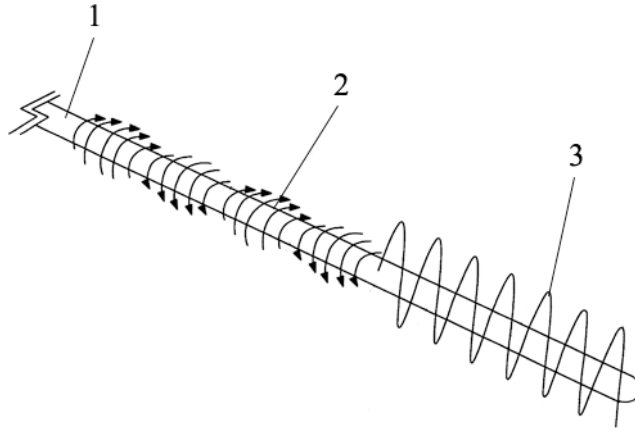


Fig. 16. Apparatus and method for an ultrasonic medical device operating in torsional and transverse modes, where 1 is the ultrasound waveguide; 2 are torsional vibrations; 3 are transverse vibrations [62].

Ultrasonic catheter for disrupting vascular occlusions. Ultrasonic catheters provide better disruption of vascular occlusions. Usually, an ultrasonic catheter consists of the elongated catheter body with one or more lumens. An ultrasonic transmission member or a wire extends through the catheter body lumen and, in many embodiments, a guidewire tube also extends through the same lumen [63]. A distal head is fixed to or otherwise mechanically coupled with the distal end of the ultrasonic transmission member or the wire and is positioned adjacent to the distal end of the catheter body. Although the distal end of the catheter body overlaps the distal head, the distal head is not directly fixed to the distal end of the catheter body (see Fig. 17). Thus when ultrasonic energy is applied through the ultrasonic transmission member, the distal tip is capable of moving freely with respect to the distal end of the catheter body. Such a freely floating distal head enables the ultrasonic catheter to remove calcific occlusions more efficiently. Moreover, it increases the life of the ultrasonic transmission member and the catheter.

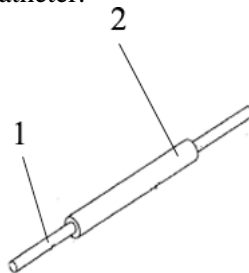


Fig. 17. Ultrasound catheter for disrupting blood vessel obstructions, where 1 is the ultrasound transmission member; 2 is the low friction coating or jacket [63].

Ultrasonic catheter and methods for making and usage thereof. Ultrasound catheter devices and their operation methods provide enhanced disruption of blood vessel obstructions. Generally, ultrasound catheters include an elongated flexible catheter body with one or more lumens, an ultrasonic transmission member extending longitudinally through the catheter body lumen and, in some embodiments, a guidewire tube extending through the lumen (Fig. 18). A distal head for disrupting occlusions is coupled with the distal end of the ultrasonic transmission member and is positioned adjacent to the distal end of the catheter body. Some embodiments include more advanced features such as a bend in the catheter body for enhancing the positioning and/or for the advancement of the catheter [64].

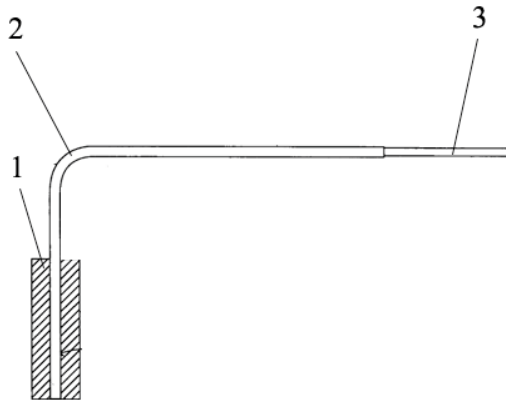


Fig. 18. Ultrasound catheter and methods of its functioning and use, where 1 is the mandrel on which the catheter body is formed; 2 is the bent catheter body; 3 is the stopper member [64].

Ultrasonic catheter with a protective feature against breakage. An ultrasound catheter is comprised of an elongated flexible catheter body having a lumen extending longitudinally therethrough, and an ultrasonic transmission member extending longitudinally through the lumen of the catheter body [65]. A proximal end of the ultrasonic transmission member is coupled to a separate ultrasound generating device. Its distal end terminates at the distal end of the catheter body. At least some portion of the distal end of the ultrasonic transmission member extends outside the lumen of the catheter body and beyond the distal end of the catheter body. The ultrasonic transmission member is directly attached to the catheter body via an attachment device (see Fig. 19).

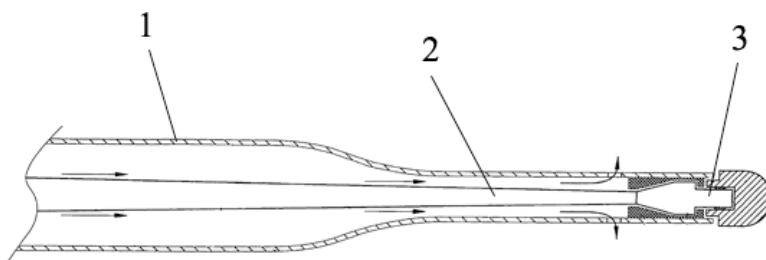


Fig. 19. Ultrasound catheter featuring a protective feature against breakage, where 1 is the catheter; 2 is the waveguide wire; 3 is the distal end of the waveguide [65].

Vibrational catheter devices and their applications. This is a vibrational catheter designed for disrupting occlusions in lumens such as blood vessels. It includes an elongated flexible catheter body that has a proximal end, a distal end and at least one lumen extending longitudinally through it. There is a vibrating transmission member that extends longitudinally through the lumen of the catheter body. It has a proximal end and a distal end, and a transition connector attached to the proximal end of the vibrating transmission member for coupling the transmission member with a vibrational energy source [66]. The transition connector includes a bore into which the proximal end of the vibrating transmission member extends (Fig. 20). The proximal end of the vibrating transmission member is attached within the bore of the transition connector with variable attachment forces in order for the transition connector to exert a minimum amount of attachment force on the attached distal-most portion of the vibrating transmission member housed within the bore.

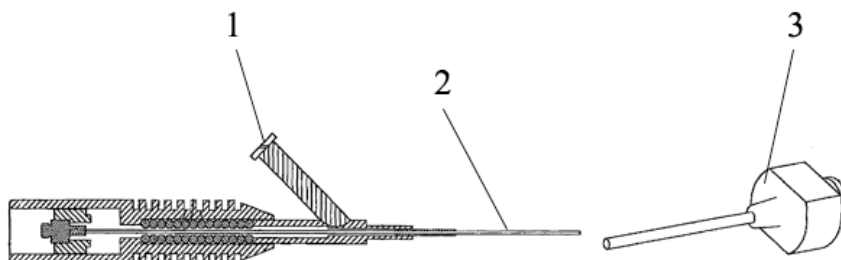


Fig. 20. Vibrational catheter devices and methods, where 1 is the intake; 2 is the waveguide wire; 3 is the transition connector [66].

Ultrasound catheter with an improved distal end. This ultrasound catheter is comprised of an elongate flexible catheter body featuring a lumen that extends longitudinally through it. There is also an ultrasound transmission member extending longitudinally through the lumen of the catheter body. The ultrasound transmission member has a proximal end that is coupled to a separate ultrasound generating device. Its distal tip is attached to the distal end of the ultrasound transmission member which is located at the distal end of the catheter body [67]. The distal tip has at least one-dimensional step. The ultrasound transmission member is directly attached to the

catheter body and/or to a guidewire tube, either directly or via an attachment device (Fig. 21). An additional radiopaque marker is positioned on the distal end of the catheter.

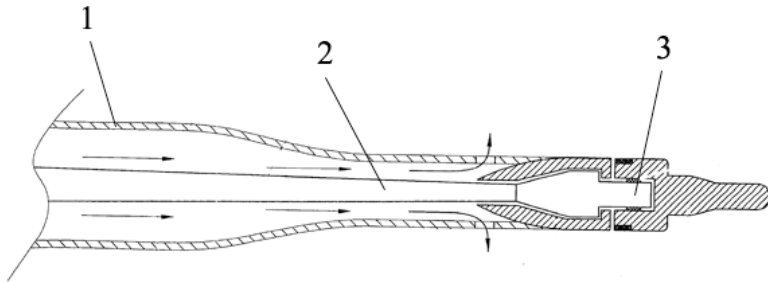


Fig. 21. Ultrasound catheter having an improved distal end; 1 is the catheter; 2 is the ultrasound transmission agent; 3 is the distal end of the ultrasound transmission member [67].

Ultrasonic catheter for disrupting vascular occlusions. Ultrasonic catheters provide better disruption of vascular occlusions. Usually, an ultrasonic catheter consists of the elongated catheter body with one or more lumens. An ultrasonic transmission member or a wire extends through the catheter body lumen and, in many embodiments, a guide wire tube also extends through the same lumen [68]. A distal head is fixed to or otherwise mechanically coupled with the distal end of the ultrasonic transmission member or the wire and is positioned adjacent to the distal end of the catheter body. Although the distal end of the catheter body overlaps the distal head, the distal head is not directly fixed to the distal end of the catheter body (Fig. 22). Thus the distal tip may move freely relative to the distal end of the catheter body when ultrasonic energy is being applied through the ultrasonic transmission member. Such a freely floating distal head enhances the efficiency of an ultrasonic catheter thus enabling it to remove calcific occlusions and increasing the life of the ultrasonic transmission member and the catheter itself.

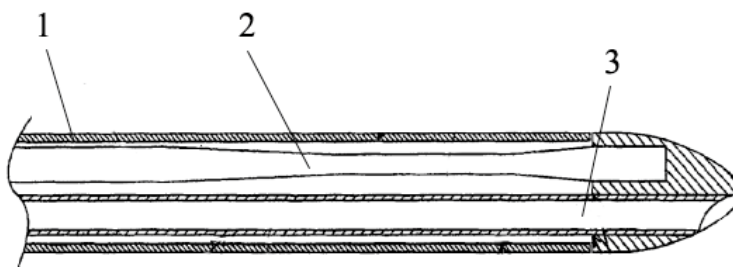


Fig. 22. Ultrasound catheter for disrupting blood vessel obstructions, where 1 is the catheter; 2 is the ultrasound transmission member; 3 is the guide wire lumen [68].

Treatment of vascular occlusions using ultrasonic energy and microbubbles. One method of treating vascular occlusions within a patient's vasculature requires positioning an ultrasonic catheter at the treatment site (Fig. 23). Further, during the

first treatment phase, the method requires to deliver the catheter's microbubble-therapeutic compound to the vascular occlusion [69].

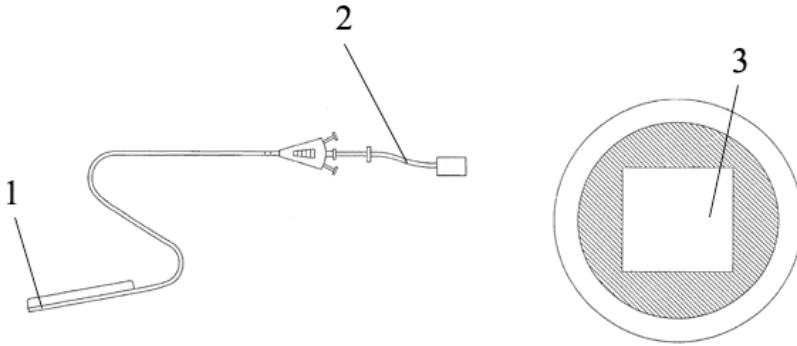


Fig. 23. Treatment of vascular occlusions while using ultrasonic energy and microbubbles, where 1 is the energy delivery section ; 2 is the cable; 3 is the inner core of the waveguide [69].

Method and Apparatus for Ablative Recanalization of Occluded Vasculature. In this particular case, a technique is offered for treating blood vessel occlusions, including chronic total occlusions (CTO) of the coronary arteries, with the capability to remove tissue material. This method is based on remotely actuated motion of an interventional RF-capable ablation device to the occlusion and controlled application of ablative RF energy [70]. The combined use of remote navigation-based precision control of the distal end of the device and the application of ablative energy enables the device to traverse elongated lesions and CTOs, as well as calcified lesions and CTOs, blockages and CTOs located at vessel branches, and in general allows the removal of the tissue material at the selected site of the tissue (Fig. 24).

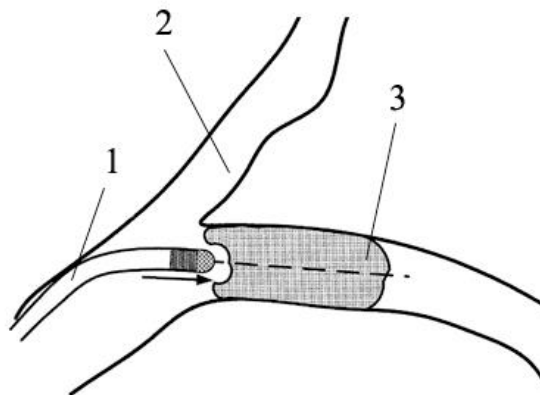


Fig. 24. Method and apparatus for ablative recanalization of blocked vasculature, where 1 is the waveguide; 2 is a blood vessel; 3 is a blood vessel occlusion [70].

Ultrasound waveguide wire for internal clearing of blood vessels. The domain of medicine can benefit from this particular invention as it may be applied for cleaning vascular walls from the inside.

With the aim to increase the efficiency and reliability of blood vessel cleaning, an ultrasound wave guide wire is used consisting of a metal wire with a tapered flexible cross-section (denoted 1) and its operational part (denoted 2), which is attached to the distal end of the catheter. The wire is made of a flexible material. The distal part of the wire equally makes the operational part (denoted 2) of a spiral shape. Its length is at least $\frac{1}{4} \lambda$, where λ is the wave length of the waveguide wire ultrasonic longitudinal vibration. The strand step is no more than 0.5 mm. The helical end makes a closed ring-shaped circuit as the ending of a spiral's last strand is connected to the beginning of the last strand (denoted 3). Then, the ending of the spiral's last strand is connected through the entire internal length of the spiral to the beginning of the spiral's first strand by the general component (denoted 4) and the housing. Thereby the spiral runs in the shape of a tube, whose walls are folded in zigzag. The ending of the last strand of such a zigzag is attached to the beginning of the last zigzag strand [71]. Once the flexible guidewire (denoted 5) has advanced through the internal cavity of the operational part and the operational part has advanced through arterial vessels, it is capable of flexing into different directions (see Fig. 25). Furthermore, all the connections of the spiral part are produced by way of mechanical twisting and/or spot welding.

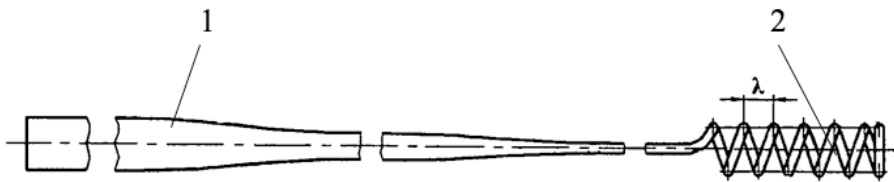


Fig. 25. Ultrasound wave guide wire for internal blood vessel cleaning, where 1 is the waveguide; 2 is the spiral end of the waveguide [71].

Despite a huge variety of invasive devices for cardiovascular recanalization, there is no vascular clearing device with the following capabilities: a) ability to operate in an invasive mode, as it is considered to be the most effective one; b) ability to deliver the required volume of drugs to the selected site of clearing; c) ability to instantly suck away the scurf of the blood clot being dissipated, at the same time; d) ability to ensure adequate advancement of the device forward (along the z axis).

2.7. Industrial Devices for the Intravascular Thrombus Decomposition

Endo Wave Infusion Catheter System The *EndoWave Infusion Catheter System* is designed for catheter-directed thrombolysis by accelerating the fibrinolytic process via ultrasound (see Fig. 26). The device combines a multiple side-hole drug infusion catheter with a guidewire-exchangeable ultrasound core for infusing therapeutic substances and delivering high frequency, low power ultrasound energy simultaneously [72]. *EKOS Endo Wave Infusion Catheter System* is different in a way

that it has three ultrasound transducers along the core wire. It combines a targeted drug delivery catheter with high frequency low-power US energy. Drugs are delivered through the catheter, not through the core wires. US accelerated CDT (Catheter-directed-thrombolysis) is used to make the blood vessel treatment procedure safe and instant; it also eliminates potential side effects. There is very little clinical data available concerning the feasibility, safety and efficiency of additional US-accelerated CDT, but the current results are very promising [73]. The success rate of real-life operations varies between 61% and 85% [74]



Fig. 26. Endo Wave Infusion Catheter System (EKOS Corporation) [72].

CLEANERXT Rotational Thrombectomy System. This system was presented at CIRSE 2016 in Barcelona, Spain (see Fig. 27). It is fitted with dual power cells that increase the run time and duration while maintaining the torque through tortuosity. The system also involves an improved drive shaft design which further increases the efficiency of the power transmission and torque. The device has an FDA clearance. It is comprised of a small ‘spiral/helical’ rotating device that extends from the end of the guiding catheter. Suction can then be applied manually from a syringe to the side port of the catheter aspirating the thrombus. The device has a rather soft end enabling it to be used as a guidewire to advance the device. The ‘sinusoidal wire’ is supposed to macerate the clot without making any damage to the blood vessel wall. However, during device rotation, the vessel wall can be contacted in even large veins and aneurysmal sections of dialysis fistulae. The motor and the power supply unit are fitted inside the handle of the device. This device is available in the following two versions: 6F (9 mm sinusoid) and 7F (15 mm sinusoid), and it comes in 65 cm and 135 cm lengths. These devices are serious competitors for *Angiojet*. Although they are by far less expensive, their effectiveness is questionable as no trials are available that would have attempted to compare them. Thus, so far, the choice among them depends mainly on the operator skills and personal preferences [75].



Fig. 27. CLEANERXT Rotational Thrombectomy System (*Argon Medical Devices*) [75].

The *AngioJet Ultra Thrombectomy System* (see Fig. 28) represents a mechanical thrombectomy device for PCI patients suffering from large thrombus burden. Moreover, this is the ONLY mechanical thrombectomy device approved by FDA for the removal of the thrombus in coronary arteries (see Fig. 29). The system is used to mechanically restore the blood flow in patients with thrombosed big arteries (more than 6 mm in diameter) [76]. *AngioJet™ Ultra* allows focused and directional thrombectomy for stronger thrombus removal capabilities. The catheter is 2.67 mm in width and 105 mm in length. The rotation of the inflow window location at the end of the catheter is directed with a torquable cylindrical component at the outside part of the catheter. *AngioJet™ Ultra* has a clear shortcoming in not being able to operate only in soft-type blood clot environment (no US is used to ease an opening of a hardened plaque) and is limited because of the fixed dimensions of the catheter.



Fig. 28. Coronary Thrombectomy System (*AngioJet™ Ultra*) [76].

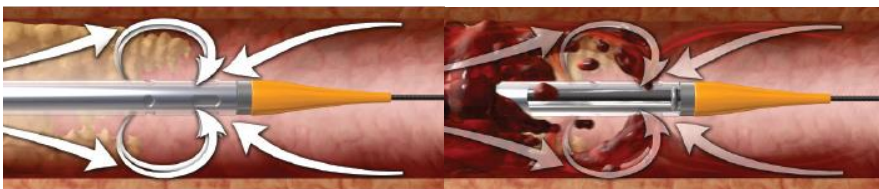


Fig. 29. A thrombus is drawn into the catheter where it is fragmented by the jets and evacuated from the body [76].

The Trellis Peripheral Infusion System [77] involves an isolated thrombolysis catheter fitted with two occluding balloons, drug infusion holes between the balloons and mechanical drug dispersion capabilities. As announced by the manufacturer, such a combination of the system's features enables medical practitioners to provide focused treatment of thrombus within a particular vessel (Fig. 30).



Fig. 30. The Trellis Peripheral Infusion System (*Covidien*) [77].

The Trellis Peripheral Infusion System is unique because of the two-occluding balloon system. After the waveguide goes through the damaged part of the blood vessel, two balloons – one at the end of the blood clot and the second one at the beginning – inflate. It stops the blood flow and isolates the abolished blood clot, so it does not go further through the blood vessel system. After the waveguide has been sunk through the damaged part of the blood vessel and the balloons have been inflated, the waveguide starts to vibrate thus destroying the scurf. The system does not provide an adequate displacement of the waveguide in the frontal direction.

2.8. Computational Modeling of Commercial Devices Intended for Clearing Blood Vessels

The delivery of high-power ultrasonic energy via small diameter wire waveguides represents an innovative alternative therapy suitable for the treatment of chronic complete occlusion of arteries. This type of energy is viable in a form of mechanical vibration at the distal tip of the waveguide with the amplitudes of vibration up to 60 μm and at frequencies of 20–50 kHz [78]. According to various reports, direct mechanical ablation, cavitation, pressure components and acoustic streaming result in the disruption of the affected tissue. It should also be noted that mechanical ablation was only evident in those cases when the cavitation threshold was exceeded. Prediction of the pressure profile generated by the distal tip of the wire waveguide was required for 140 elements per wavelength (EPW).

A significant role appears to be played by the acoustic pressures developed at the waveguide-fluid/tissue interface. As some authors observed, plaque ablation was only evident above the cavitation threshold [79].

Due to the significance of the pressure amplitude at the waveguide distal tip, the subsequent cavitation, and the pressures generated in the surrounding fluids and

tissues, a vast number of researchers became involved in studying this phenomenon. Some analytical solutions of simplified geometries and conditions were offered, and one of them is a solution involving a pulsating sphere within a fluid and a more representative oscillating sphere within a fluid. Equation 1.3 shows the Morse solution [80] for the pressure field near an oscillating sphere in a fluid. Although this linear solution is limited to a simple geometry, it has been suggested by Nyborg [81] as a useful approximation for the prediction of pressure amplitudes and the subsequent cavitation associated with the frequencies and conditions encountered in the use of ultrasound angioplasty.

$$P_{\max} = 2\pi^2 \rho R f^2 d \times \frac{R^2 \cos \theta}{r^2} \quad (1.3)$$

where: P_{\max} = Pressure amplitude at a location in the fluid, a function of θ and r ; d = amplitude of the vibration of the sphere; f = frequency of the vibration of the sphere; R = radius of the sphere; ρ = fluid density; r = radial distance from the centre of the sphere; θ = the angle between the direction of oscillation and the radius vector

With regard to medical applications, high power ultrasound basically represents a non-linear propagation of sound waves above approximately 20 kHz. It is derived from the nonlinear pressure-density relationship, and the variance in the speed of sound with the pressure amplitude during the compression/rarefaction cycle, and with higher frequencies and greater intensities, a more significant effect is observed.

For the purpose of solving the finite element acoustic fluid-structure interaction models, the NavierStokes equations of the fluid momentum and the flow continuity equation must be taken into consideration along with the structural dynamics equation. Assuming linear wave propagation for an incompressible fluid with no mean flow, neglecting shear stresses and with a uniform mean density and pressure throughout the fluid, the lossless acoustic wave equation can be written as follows [78]:

$$\frac{1}{c^2} \frac{\partial^2}{\partial t^2} - \nabla^2 P = 0 \quad (1.4)$$

Where $c = \sqrt{\frac{k}{\rho}}$ and: k is the bulk modulus of fluid.

The equation governing the acoustic wave propagation given in Equation 1.4 can be discretized by taking into account the coupling of acoustic pressure and the structural motion present at the fluid-structure interface.

$$\text{Fluid: } [M_F](\ddot{\vec{P}}) + [K_F](\vec{P}) + \rho[R]^T(\ddot{\vec{u}}) = 0 \quad (1.5)$$

$$\text{Structural: } [M_S](\ddot{\vec{u}}) + [K_S](\vec{u}) - [R](\vec{P}) = (\vec{F}_S) \quad (1.6)$$

Where $(\ddot{\vec{P}})$ is the 2nd derivative of the nodal pressure vector; (\vec{P}) is the nodal pressure vector; $(\ddot{\vec{u}})$ is the 2nd derivative of the nodal displacement vector; (\vec{u}) is the nodal displacement vector $[M_F]$ is the Fluid mass matrix; $[K_F]$ is the fluid stiffness

matrix; M_S] is the Fluid mass matrix; $[K_S]$ is the Structure stiffness matrix; $[R]$ is the coupling matrix that represents the effective surface area associated with each node on the fluid structure interface; (\vec{F}_S) is the fluid pressure load vector

Further, Equations 1.5 and 1.6 can be combined into a single relationship describing the load quantities at all locations in the fluid and structure as shown below in Equation 1.7.

$$\text{Combined: } \begin{bmatrix} M_S & 0 \\ \rho_0 R^T & M_F \end{bmatrix} \begin{pmatrix} \ddot{\vec{u}} \\ \ddot{\vec{P}} \end{pmatrix} + \begin{bmatrix} K_S & -R \\ 0 & K_F \end{bmatrix} \begin{pmatrix} \vec{u} \\ \vec{P} \end{pmatrix} = \begin{pmatrix} \vec{F}_S \\ 0 \end{pmatrix} \quad (1.7)$$

Finite element models applied for ultrasound angioplasty to date have mainly focused on modeling the way how the wire waveguide transmits the ultrasonic waves to the distal tip. Meanwhile, Gavin *et al.* [82] opted to perform a modal and harmonic analysis in order to determine the resonant characteristics, damping and stresses of the wire waveguide. The analysis of mesh density revealed that having an adequate mesh density is of huge importance in order to make it possible to resolve the wave structure accurately. These authors also undertook the modeling of the effect that the presence of fluid had on the resonant response of waveguides. It led to the conclusion that the effect was negligible due to the low forces encountered at the distal tip. However, the hydrodynamic effects, such as the drag on the distal tip, appeared to be capable of playing a more critical role.

From the theoretical point of view, the process of making a computational model is comprised of the following steps:

- 1) Model verification that involves analysis of mesh density;
- 2) Analysis of an acoustic pressure field versus waveguide parameters;
- 3) Validation of the model developed: an *in vivo* model in a peripheral artery.

The 3-step FEM methodology was used in the following Chapters 2.3 and 2.4.

2.9. Formulation of Objectives and Tasks

According to mortality statistics, cardiovascular disease (CVD) remains the most common cause of death in Europe, currently accounting for 45 percent of the total deaths, to be more precise, 49 percent of deaths among women and 40 percent among men. Each year, more than 4 million people die from CVD in Europe with 1.4 million of these deaths before the age of 75 years.

According to the findings of various studies, the burden of CVD mortality features huge inequalities across Europe and a significant variation in mortality rates from these diseases. On average, EU member countries suffer a lesser burden in terms of CVD mortality, whereas the lowest burden on the average is borne by EU-15 countries (the ones that have been members of the EU the longest). Interestingly, the 12 countries where the burden in terms of mortality from CVD decreased significantly, resulting in the number of deaths from CVD being less than that from cancer in men, along with the 2 countries where the same is true for women, are all located in Western Europe [83].

Endovascular intervention is the most rapidly growing domain of vascular medicine. Peripheral vascular interventions have been developed in pursuit of several objectives, some of them being as follows: to avoid the need for general or epidural anaesthesia, to eliminate the risks related to conventional surgical procedures, to minimize discomfort to the patients, to reduce the recovery times, and to lower the cost of treatment [84].

One of the endovascular interventional techniques covers ultrasound enhanced catheter-directed thrombolysis. Generally, it involves high-frequency low-energy ultrasonic waves, concurrently with the infusion of thrombolytic drugs with the general aim of accelerating plasmin-mediated thrombolysis. It is designed to reduce the treatment duration, the dose of the infused thrombolytic drug, and thrombolysis-related complications when compared to catheter-directed thrombolysis alone [85].

A comprehensive literature review revealed a need for an innovative ultrasonic vascular clearing device with the following capabilities: a) operating in an invasive mode, as it is considered to be the most effective one; b) delivering the required volume of drugs to the selected site of clearing; c) instantly sucking away the scurf of the blood clot being dissipated at the same time; d) ensuring adequate advancement of the device forward (along the z axis).

3. DESIGN AND MODELING OF THE WAVEGUIDE

During the process of the research, two different ultrasonic devices were designed for vascular clearing. They are intended to operate in the same frequency range of (15–30 kHz) and to perform a similar primary function (vascular recanalization). However, they are radically different in their structure and principle of operation. The structures of these two waveguides are presented in detail below. Since the second invention, detailed in Chapter 2.2, is more functional, easier to be produced, and in fact represents an improved version of the first one, the ‘Ultrasonic device for internal vascular clearing’ discussed in Chapter 2.1 was not experimentally investigated.

In both cases under consideration, the waveguide system is comprised of the guiding catheter, a thinner soft wire (to prevent perforation of a blood vessel) fitted with the second catheter, also made of a soft material which is used to simultaneously pull through the first catheter while introducing the elongated metal waveguide into the blood vessel.

In the further research, discussed in detail in Chapters 3 and 4, the waveguide (an innovative device being designed) is investigated without taking into consideration the guiding catheter and the second catheter, which, while being larger, mainly performs a protective function.

3.1. Design of Ultrasonic Device for Internal Vascular Clearing

3.1.1. Description of the Device

The invention under consideration here is attributed to the field of medicine as it can be applied for the pharmaceutical clearing of blood vessel inner walls as well as the suction of the plaque deposited on the surface of these walls.

The ultrasonic vascular clearing system is comprised of the source of ultrasound made of a high frequency ultrasound generator and a piezo transducer, a concentrator of mechanical vibrations which is connected in series, a metal wire waveguide with its free end being in a shape of a spiral and which is made of a solid and the same highly elastic substance, for instance, stainless steel, nickel, titanium or alloys thereof.

The ultrasonic micropump-dispenser intended for supplying and dispensing liquids is comprised of a cylindrical body fitted with the conical spiral member inside of it, and the generator inducing vibrations, i.e., a piezoceramic ring is placed on the cylindrical body. The cylindrical body is filled with the relevant liquid.

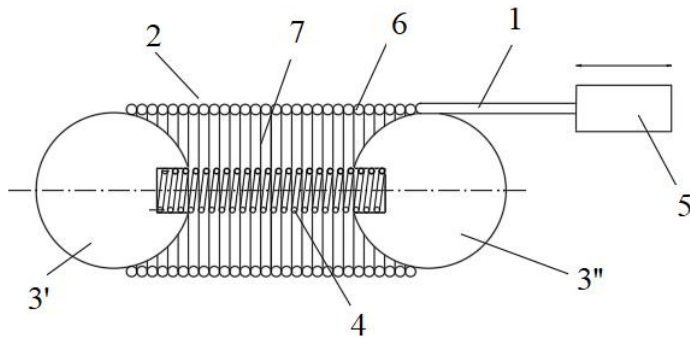


Fig. 31. Ultrasonic volumetric dispenser: 1) is the waveguide; 2) is the operational part; 3) are the spheres; 4) is the spring; 5) is the ultrasound generator; 6) are spiral threads; 7) is confined space.

The closest possible analogue is presented in European patent application No. 08478001.4: *the ultrasonic device for internal vascular clearing comprised of the specifically shaped waveguide with its free end being twisted into the spiral*. The waveguide is excited from the generator of high frequency vibrations.

The above mentioned device can be charged with a liquid (drugs) to be dispensed from the end of the waveguide of a spiral shape. However, the liquid can only be charged if it is in the form of a frozen capsule or powder (drugs) mixed with viscous grease that, under the influence of the vibrations induced from the ultrasonic generator and transmitted through the waveguide to the spiral, is/are spread at the localized site of the blood vessel. The generated scurf is sucked away into the catheter through a special exterior suction device.

The ultrasonic device of the innovative design for the internal vascular clearing covered by this invention offers a solution of the shortcomings characteristic to the devices discussed above. It also boosts the efficiency of the vascular clearing and expands the functional capabilities of an ultrasonic device (including the local dosing of drugs and sucking away the scurf).

The aim of the invention was to increase in efficiency the vascular clearing while expanding its functional capabilities (the local dosing of drugs and sucking away the scurf) of the ultrasonic device for the internal vascular clearing, which is achieved by making the clearing device's waveguide out of the wire of a variable diameter and involving an operational part of a spiral shape which is clamped between two spheres by using a spring. This results in a confined cavity which may be charged with drug delivery nanosystems, for instance, nanoparticles, nanospheres, nanocapsules, and hydrogels. Sucking away the generated scurf into the catheter happens in a confined space between the strands of the spiral by means of creating vacuum and by inducing deformations of the running wave of the opposite direction within the waveguide.

3.1.2. Structural Layout of the Device

Fig. 32 shows the vascular clearing device, comprised of the ultrasonic waveguide (1) having the operational part of a spiral shape (2) which is confined by spheres on its both sides (3', 3'') attached to each other by the spring (4), inside of which, drug delivery nanosystems are to be placed (not shown in the figure), such as nanoparticles, nanospheres, nanocapsules, and hydrogels. The above-mentioned waveguide is attached to the ultrasonic vibration generator (5) through a thread connection.

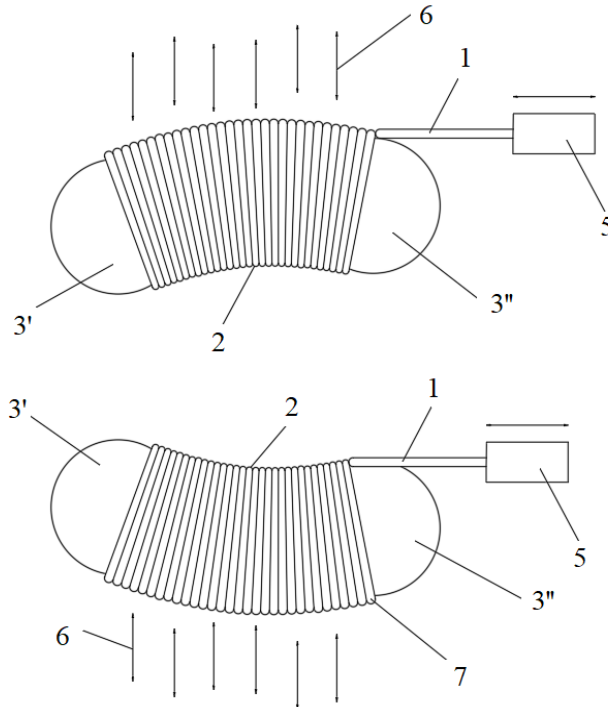


Fig 32. A schematic view of operation of the ultrasonic volumetric dispenser, where 1) is the waveguide; 2) is the operational part; 3) are spheres; 4) is the spring; 5) is the ultrasound generator; 6) is the cavitation stream; 7) are spiral threads; 8) is confined space.

High frequency mechanical vibrations coming from ultrasound generator (4) are transmitted to waveguide (1) where they continue to propagate over its entire length to the operational part of a spiral shape (2). Due to its specific structure, the operational part of the waveguide (2) allows placing a particular limited amount of drugs inside of it delivered in a form of nanoparticles (drug carrier nanosystems), which in turn enables feeding the drug to the selected site (the point of lesion).

When the internal vascular clearing device is in operation, the mechanical motion of its operational part (2), the increased temperature and the hydrodynamic processes occurring in the blood speed up the distribution of drugs in a form of nanoparticles in the operational field (at the site of the lesion). Nanoparticles (which

are spread in the fluid) are exposed to the concentrated energy flowing through the waveguide (1) and its operational spiral part (2) with spheres (3', 3'') resulting in cavitation processes within the blood vessel. The cavitation process is distributed over the entire length of the operational part (2) in the radial direction (6). In the course of the cavitation process, microbubbles are formed in the fluid (i.e., blood), and the microenergy released during their rupture tends to disrupt the sediments built up on the interior walls of the blood vessels thus destroying (removing) blockage from the blood vessel. By inducing bending deformations opposite in direction within the waveguide (1) and simultaneously within the operational part (2), sucking away the generated scurf into the catheter takes place (not shown in the figure) through the vacuum created in the confined space (8) available between the strands of the spiral (6) and the spheres (3', 3'').

In comparison to its closest possible analogue, this ultrasonic device of the innovative design for internal vascular clearing with the included drug delivery nanosystems helps lowering the cavitation threshold (the amount of the energy required to induce cavitation), breaks and dissolves the thrombus present inside of the vessel, promotes tissue regeneration processes, minimizes the risk of drug overdosing and enables eliminating the scurf generated inside of the blood vessel which in turn increases the reliability and efficiency of the vascular clearing.

3.1.3. Novelty of the Device

The ultrasonic device for internal vascular clearing offered by this invention is different from its predecessors as follows:

1. The free ending of the ultrasonic device for internal vascular clearing is twisted into a spiral thus making an internal cavity inside of the operational part of the waveguide additionally limited by two spheres that are interconnected with a spring while creating a confined space limited by the strands twisting in a shape of a spiral and by two spheres. The spiral end of the ultrasonic device can be used as a drug transporter. However, it is necessary to freeze or put into the soluble membrane before transporting drugs the required place of the body.

2. This ultrasonic device for internal vascular clearing is distinguished by the vacuum created during its operation in the closed cavity of the operational part of the waveguide.

3.1.4. Technological Challenges

The ultrasound catheter under consideration contains a metal wire probe with a free ending leading to a risk of the spiral part's fracture under particular frequencies of spiral vibrations.

The volume of the drugs delivered through a catheter is limited due to its structural features, i.e., the size of the frozen capsule to be inserted is determined by the cavity available between the strands of the spiral that link two spheres in the operational part of the waveguide.

The device described herein possesses no capability to precisely divert and target the dispensed-sucked liquid to the localized site of the blood vessel to be treated

through the catheter as the entire catheter has to be filled with the fluid, and the source of vibrations is located outside the device, which makes it less efficient than desired.

Although the ultrasonic volumetric dispenser is sound theoretically, due to clear technological challenges described above, the decision to continue developing an ultrasound waveguide was made. Therefore, the design of the tube-shaped ultrasound waveguide described in Chapter 2.2. was created.

3.2. Design of the Tube-Shaped Ultrasound Waveguide

3.2.1. Description of the Device

The results described/presented in this chapter have been published in the following article: Kargaudas, V., Bubulis, A., Navickas, J., Vitkus, L., Venslauskas, M. Theoretical and Experimental Investigation of Tube-Shaped Waveguide Wire. *Journal of Measurements in Engineering* 5, 2017, 257-265.

The tube-shaped ultrasound waveguide wire with orifices at its operational end was offered as the alternative to some currently patented interventional thrombosis treatment solutions. The principal scheme of an innovative waveguide is presented below in Figures 34 and 35.

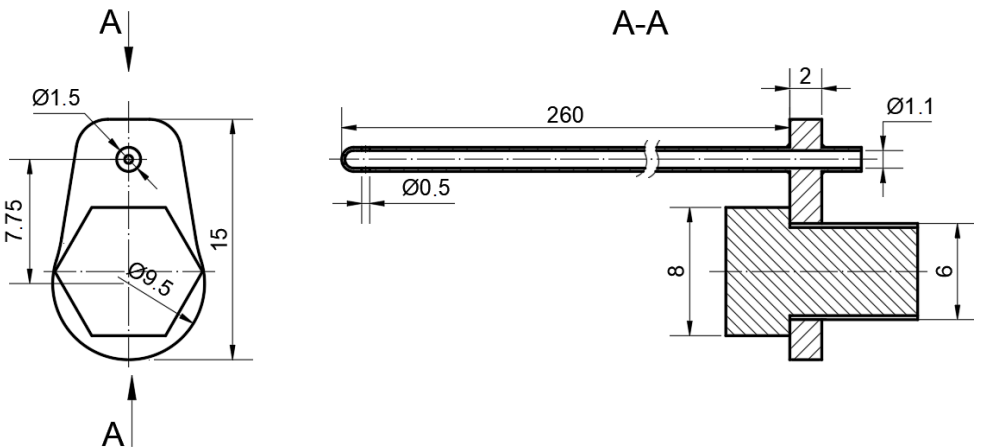


Fig. 33. Ultrasonic vascular cleaning device (cross-section).

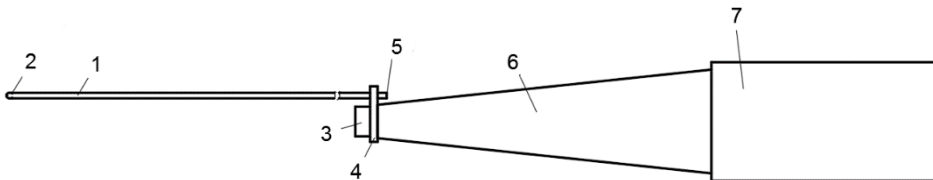


Fig. 34. Ultrasonic blood vessels cleaning system, where: 1) is the tube-shaped waveguide; 2) is the waveguide hole; 3) is the fixing screw; 4) is the lug; 5) is the intake; 6) is the concentrator; 7) is the transducer.

The waveguide wire of 260 mm in length and 1.5 mm in diameter is considered to be an interventional medical device. It can be used for cleaning the inner walls of arteries. It can also be used as a tool to break down and destroy the thrombus and simultaneously suck out the scurf of the blood clot being dissipated.

Adequate feed of the drugs to the damaged site of the blood vessel is secured by the unique design of the wire. The lug that enables the device to get attached to the concentrator is separated from the tube intended for drug infusion. Fig. 34 shows its construction in detail. The diameter of the intake is 1.1 mm.

The waveguide wire of such a structure allows impacting the occlusion not only mechanically but also by the flow of physiological fluid infused through the intake (denoted 5 in Fig. 34).

To ensure the efficient delivery of a sufficient quantity of drugs to the required site of the artery to be treated, a tube-shaped waveguide wire was selected. The orifices drilled at the end of it act both as intake and suction holes, if necessary.

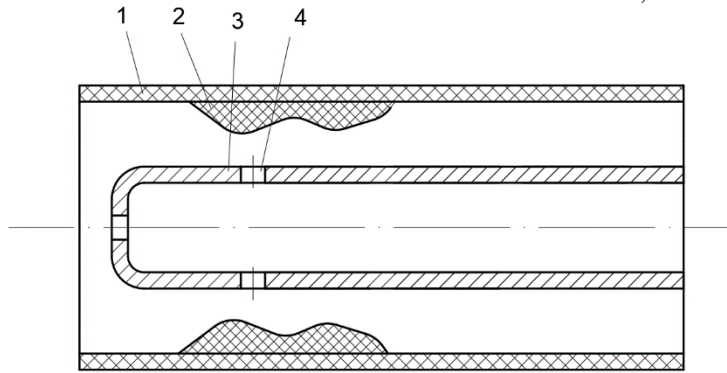


Fig. 35. The tip of the waveguide: 1) is the blood vessel wall; 2) is the occlusive derivative; 3) is the waveguide; 4) is the wall of the waveguide.

The dimensions of the waveguide were selected based on the standard diameter of arteries in lower human limbs. To ensure that the device is capable of operating even at the level of popliteal arteries, the diameter of 1.5 mm was specifically chosen for the waveguide. The selection of the other dimensions, as well as the length optimization of the innovative design system under consideration, are disclosed in the upcoming European patent application “Tube-Shaped Ultrasound Wave Guide Wire for Internal Blood Vessels Cleaning”.

As arteries can be totally (meaning that the blood circulation is completely blocked) or partially occluded (meaning that a blood clot might be adhered to the wall of the blood vessel), waveguide holes can be positioned in the following two directions – frontal (for totally occluded arteries) and transverse (for partially occluded arteries). As an alternative, holes may only be positioned at the front or only on the side of the waveguide; however, in this case, the waveguide under consideration would only be useful for very specific situations.

3.2.2. Structural Layout of the Device

The vascular clearing device shown in Fig. 34 involves a tube-shaped waveguide (1) with the holes drilled at its tip (2), a trough (3) and an open aperture (5) for the infusion of drugs and physiological saline solution to the required site of the blood vessel under treatment, and a metal screw (3) used to attach the waveguide to the concentrator (6) through a specific lug (5). The system is excited by a high-frequency vibration generator.

During the operation of the vascular clearing device, the mechanical work accomplished by its operational part (1) not only destroys harmful formulations present in its vicinity inside the blood vessel by means of the induced cavitation process but also effectively distributes drugs being fed to the site of lesion. The tube-shaped part (1) of the waveguide while vibrating in its radial and frontal directions causes the cavitation process in blood.

The process of cavitation causes microbubbles to form in the fluid (i.e., in blood), and the microenergy released during the rupture of these bubbles disrupts the sediments built up on the interior walls of the blood vessels thus destroying (removing) blockage from the blood vessel.

To increase the efficiency of the interior vascular clearing while simultaneously expanding the functional capabilities of the ultrasonic device for internal vascular clearing, a steel tube (1) was used as one of the parts comprising the waveguide with the holes drilled at its tip (2). The open orifice (4) at the tip of the tube-shaped part of the waveguide enables feeding an unlimited volume of drugs through the trough to the damaged site of the blood vessel under treatment, and at the same time allows sucking away scurf of broken harmful formulations generated during the operation of the clearing system.

Smooth feeding of drugs is ensured due to the unique structural solution built-in in the waveguide – its separate part that is present at the concentrator which is not used for the delivery of drugs to the damaged site of the blood vessel – is attached to it with the metal screw (3).

In comparison to its closest possible analogue, this ultrasonic device of the innovative design for internal vascular clearing with the included drug feeding system breaks, dissolves and removes thrombus present inside of the vessel, promotes tissue regeneration processes, ensures the delivery of any required amount of drugs, and, if necessary, is capable of operating in a freshly supplied blood substitute (physiological saline) instead of blood, which in turn significantly increases the reliability and efficiency of vascular clearing.

3.2.3. Novelty of the Device

1. The ultrasonic device for internal vascular clearing comprised of the waveguide of a specific shape with holes drilled at its tip is distinguished by the hollowed operational part which also has an orifice for feeding the required amount of the fluid.

2. The ultrasonic device for internal vascular clearing makes it possible to deliver an unlimited volume of drugs to the selected site of a damaged blood vessel through the open part of the waveguide.

3. High frequency vibrations transmitted by this ultrasonic device for internal vascular clearing bypass the site used to feed the drugs or physiological saline. Vibrations are transmitted from the concentrator to the required site of the blood vessel treated through a separate fixation member including the screw.

4. The ultrasonic device for internal vascular clearing under consideration here offers the possibility of executing the cavitation process (breaking and disrupting adjacent tissues and causing high temperatures) in a specific fluid fed from the outside instead of the patient's blood.

3.2.4. Technological Challenges

The use (or the reliability, to be more precise) of the above-discussed invention is mainly limited by the relatively complicated structure of its component (4) in Fig. 34, i.e., the lug. It requires the highly accurate and precise welding of the tube (1) and the lug. Otherwise, not only the reliability of the device operation may be impaired but the transmission of the high frequency vibrations from the generator to the damaged site in the human body might be impeded as well.

3.3. Computational Modeling of a Waveguide Wire Operating within a Blood Filled Blood Vessel

Simulation of the tube-shaped ultrasonic waveguide wire under consideration was accomplished by using the *Finite Element Method* (FEM). Eigenfrequency analysis was performed for the body of waveguide in addition to time-dependent simulation for the entire waveguide wire structure. The waveguide wire was modeled by using COMSOL Multiphysics – a finite element analysis, solver and simulation software package intended for various engineering and physics applications and coupled phenomena. Fig. 36 features a geometry and FEM meshing of the model.

Interface of Solid Mechanics physics was used to model the behavior of the waveguide wire. Structural steel with density $\rho = 7,850 \text{ kg/m}^3$, Young's modulus $E = 200\text{e}9 \text{ Pa}$, and Poisson's ration $\nu = 0.33$ were applied to the body of the tube-shaped ultrasound waveguide wire and its housing. The main equations governing the finite element model for the time-dependent study are as follows:

$$\rho \frac{d^2 u}{dt^2} - \nabla \sigma = Fv \quad (2.1)$$

$$S - S_0 = C(\varepsilon - \varepsilon_0 - \varepsilon_{inel}) \quad (2.2)$$

$$\varepsilon = \frac{1}{2}(\nabla u^T + \nabla u) \quad (2.3)$$

Here, u denotes the displacement field; t denotes time; ρ is the density of the material; σ is the stress tensor; F represents an external volume force; v denotes the velocity, ε is the strain value (ε_0 is the initial strain, ε_{irei} is the inelastic strain), S

represents stress (S_0 is the initial stress value), C is a tensor product. The ambient temperature condition is $T = 293.15$, and the absolute pressure is $P_A = 1 \text{ atm}$.

Understanding the dynamics of a waveguide vibrating in an elastic fluid-filled vessel is important for effective applications of ultrasound in invasive blood-vessel cleaning systems. Numerical simulations are performed based on a two-dimensional (2D) asymmetric finite element model to investigate the influences of both acoustic driving parameters (e.g., pressure and frequency) and material properties (the vessel size, visco-elastic parameters, and fluid (blood) viscosity) on the dynamic interactions in the waveguide-blood-vessel-muscle system. A simplified model is shown in the figure below, and the main parameters of the simplified model are described in Table 1.

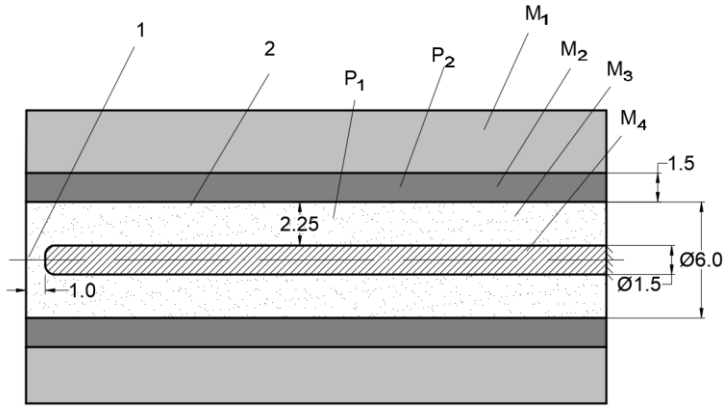


Fig. 36. A simplified model of the waveguide operating inside a blood vessel, where M_1 is a human muscle; M_2 is the wall of the blood vessel; M_3 is blood; M_4 is stainless steel; Point 1 is the pressure measuring point within 1 mm distance from the tip of the waveguide; Point 2 is Pressure measuring point 2 within 2.25 mm distance from the side of the waveguide; P_1 is the pressure inside the blood vessel; P_2 is the pressure inside the wall of the blood vessel.

Table 1. Main parameters of the simplified model

Diameter of the waveguide	1.5 mm
Artery diameter	6 mm
Waveguide length	260 mm
Waveguide fixing point	On the right

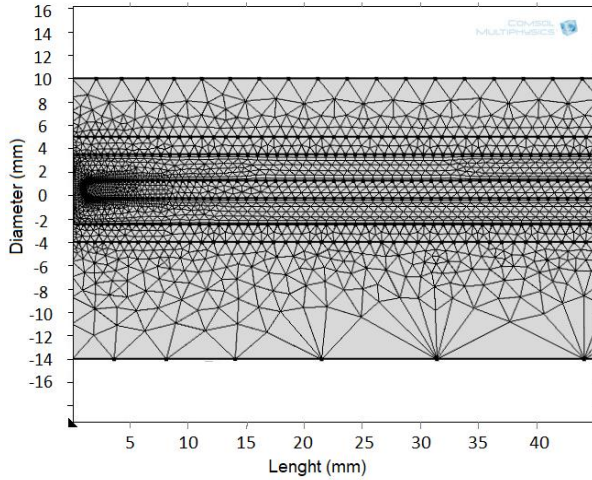


Fig. 37. Illustration of the geometry and FEM meshing of the simplified waveguide wire and the surrounding tissues.

FEM analysis showed that the surrounding fluid does not have any notable impact on the piezo rings-generated high frequency (~22-24 kHz) longitudinal vibrations, although it is significant for the modes of transverse vibrations. Fig. 38 describes the longitudinal displacement of the vibrating waveguide (cylinder) that was fastened on the right.

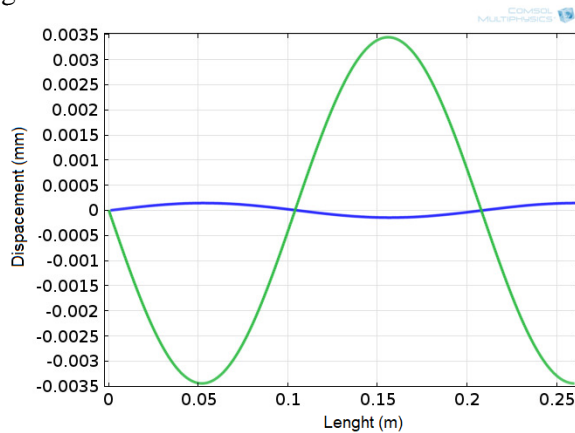


Fig. 38. Real vibration forms. The green line shows the longitudinal vibrations, the blue line represents the transverse vibrations.

Fig. 39 shows the resonance frequency of the rod for the best longitudinal vibrations. The difference between the resonant frequency in a fluid environment (water) or air is insignificant. The rod was actuated by the longitudinal 5 μm movement of the piezo ring. Analysis showed that the resonant frequency providing the best displacement of the tip of the waveguide is 24.970 kHz.

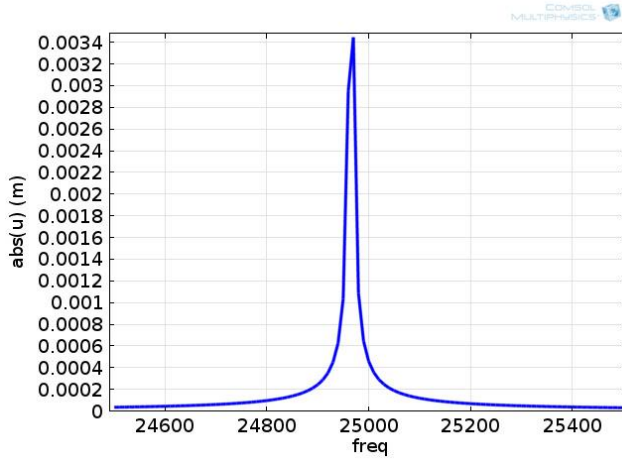


Fig. 39. Amplitude-frequency characteristics at the end of the rod.

A transient analysis of the working system (in 24.970 kHz) is shown in Fig. 40. Fig 41 is just an enlarged representation of Fig. 40 for clearer understanding of the process and describes vibrations after the process becomes stationary (6×10^{-4} s after the piezo rings start to vibrate). The transient analysis also shows at what point of time the excitation is the best and what kind of response to the excitation of the stainless-steel rod placed in a blood-filled blood vessel it actually provides.

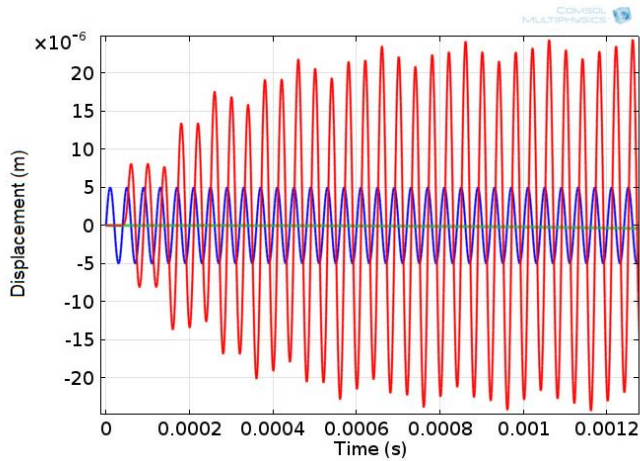


Fig. 40. Transient analysis, where the blue curve denotes excitation; the red curve is the longitudinal displacement response to the excitation; the green line is the transverse vibrations of the response.

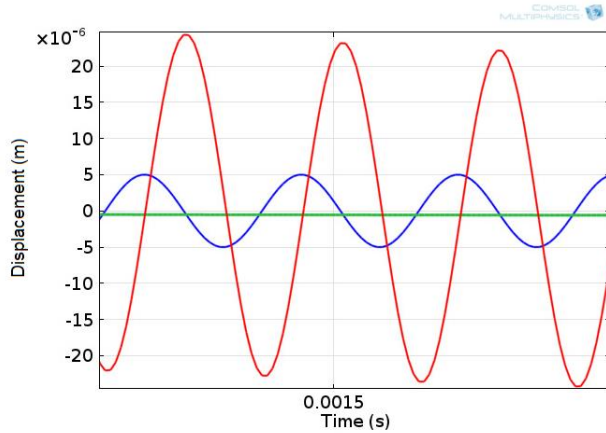


Fig. 41. Transient analysis (zoomed), where the blue curve is excitation; the red curve shows the longitudinal displacement response to the excitation; the green line demonstrates the transverse vibrations of the response.

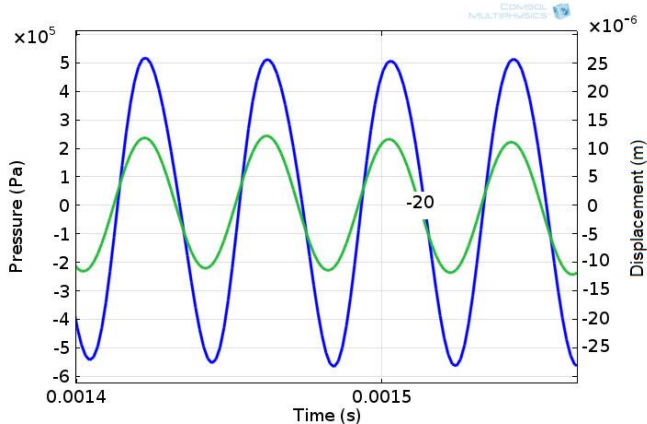


Fig. 42. Pressure at the point in the middle of the thrombus and rod displacement. The blue line is the longitudinal displacement of the tip of the rod; the green line is the pressure at the centre point of the thrombus

The green line in Fig. 42 shows the pressure at the tip of the rod and at the point of the middle of the thrombus caused by the longitudinal vibration component. The pressure at the tip of the rod is $\pm 5.05 \times 10^5$ Pa, and the pressure at the middle point of the thrombus is $\pm 2.40 \times 10^5$ Pa.

Further graphs show the results of the analysis of the vibrational period of the rod at four different points of time after the vibration process becomes stationary:

- 1562 (A) – stretched in frontal direction;
- 1573 (B) – at point 0 between being stretched and shrunken;
- 1583 (C) – shrunken in the frontal direction;
- 1593 (D) – at period point 0.

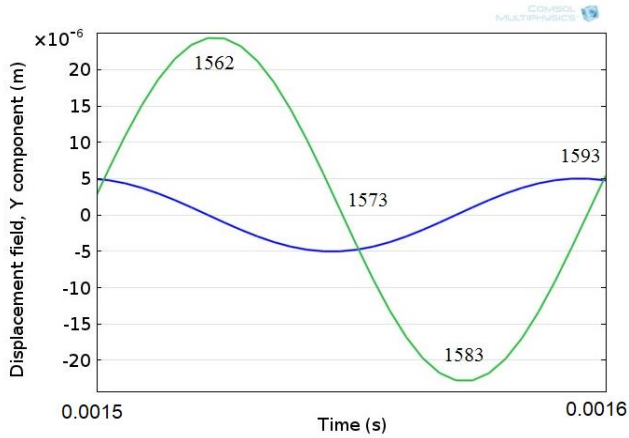


Fig. 43. The particular analyzed time points of the stationary process. The blue curve denotes excitation; the green curve shows the displacement response at the tip point of the rod. The numbers above the curves show the time point of the process.

As it is shown in Figure 43, the best displacement of the Y component is $\pm 2.3 \times 10^{-5}$ m. Fig. 44 shows displacements of the wall of the blood vessel throughout its length at different time points during the time period.

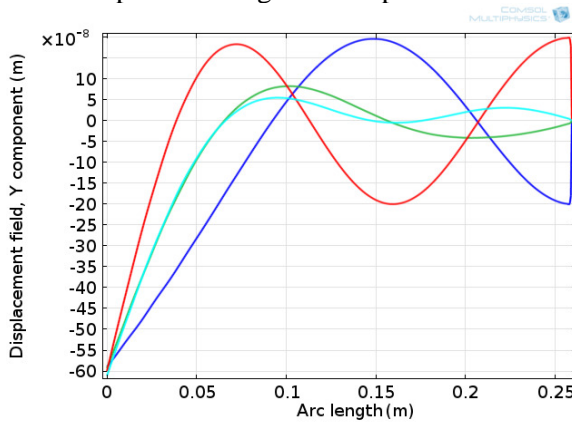


Fig. 44. Transverse displacement of the wall of the blood vessel. The blue curve is at time point A (when the rod is stretched in the frontal direction); the green curve is at time point B (at point θ between being stretched and shrunken); the red curve is at time point C (the rod is shrunken in the frontal direction); the electric curve is at time point D (at point θ).

Fig. 45 is related with Fig. 38 (the first figure of Chapter 2.4.). The mode of the longitudinal vibration is influenced by longitudinal and transverse vibrations. Fig. 46 shows an enlarged and more detailed view of Fig. 45.

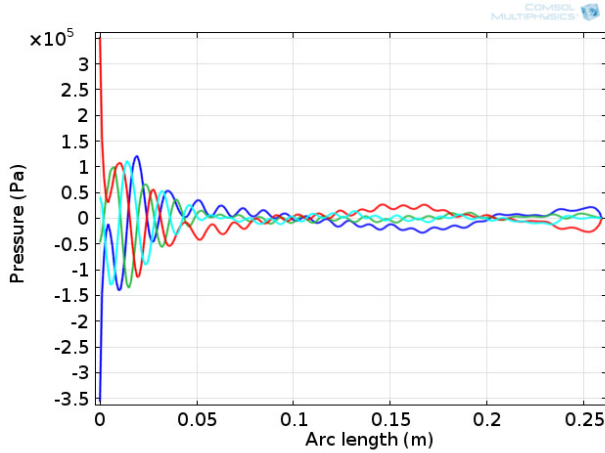


Fig. 45. Pressure to the inner wall of the blood vessel. The blue curve is given at time point A (when the rod is stretched in the frontal direction); the green curve is at time point B (at point 0 between being stretched and shrunken); the red curve is at time point C (the rod is shrunken in the frontal direction); the electric curve is at time point D (at point 0).

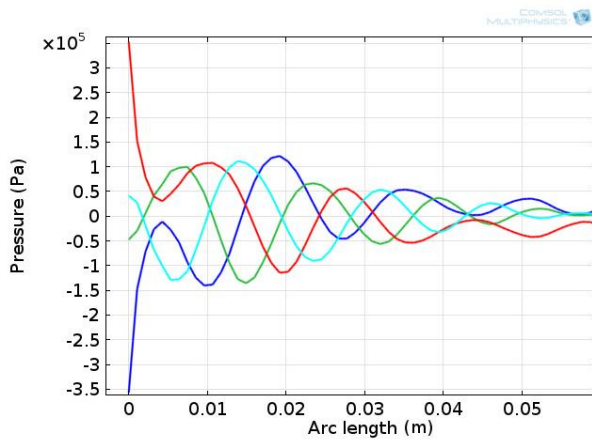


Fig. 46. Pressure to the inner wall of the blood vessel (enlarged). The blue curve is given at time point A (when the rod is stretched in the frontal direction); the green curve is at time point B (at point 0 between being stretched and shrunken); the red curve is at time point C (the rod is shrunken in the frontal direction); the electric curve is at time point D (at point 0).

Analysis shown in Figures 45–46 show that the optimal pressure ($\pm 3.5 \times 10^5$ Pa) when the ultrasound vascular clearing system is working in the resonant mode happens at the tip of the waveguide. Therefore, it generates the best pressure to the inner wall of the blood vessel.

The following graphs show the variations of the pressure fields and the intensity of deformations at the previously described time points (A, B, C and D) of the vibration period. The lines describe the pressure fields, while the intensity of the colors describes the intensity of deformation.

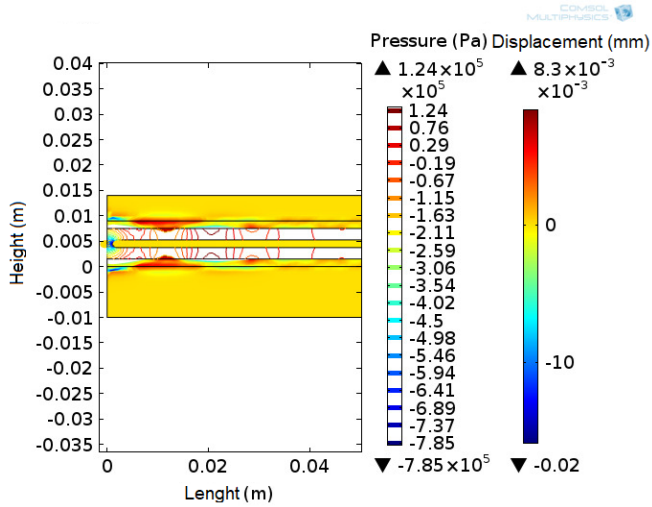


Fig. 47. The pressure fields and intensity of deformation at time point A (1), when the rod is stretched in the frontal direction. The left column shows pressure (Pa), while the right column shows displacement (mm).

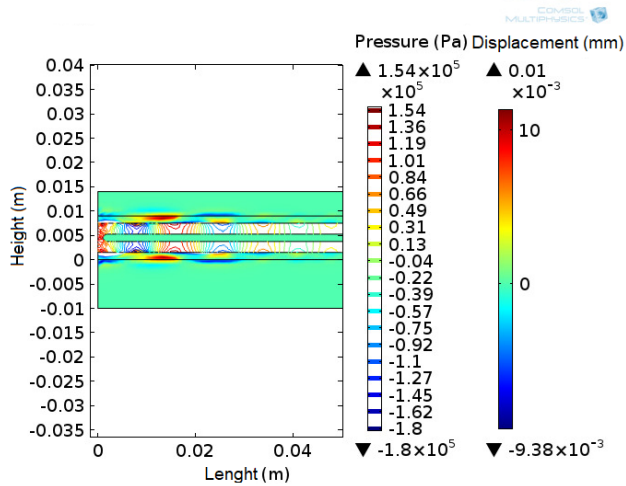


Fig. 48. The pressure fields and intensity of deformation at point B (0). The left column shows pressure (Pa), while the right column shows displacement (mm).

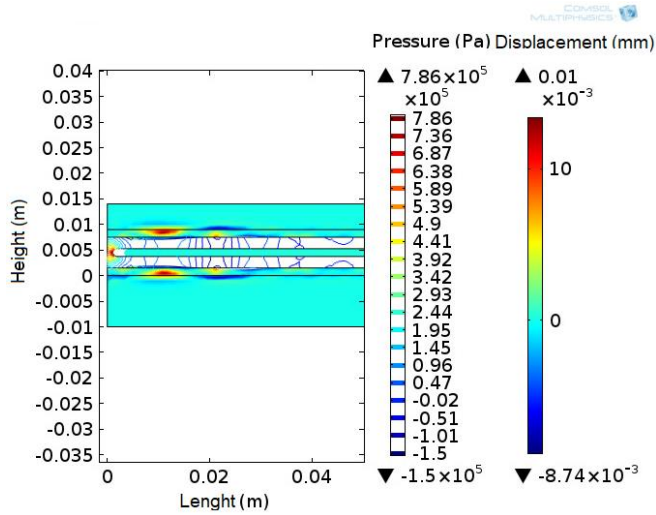


Fig. 49. The pressure fields and intensity of deformation at time point C, when the rod is shrunken in the frontal direction. The left column shows pressure (Pa), while the right column shows displacement (mm).

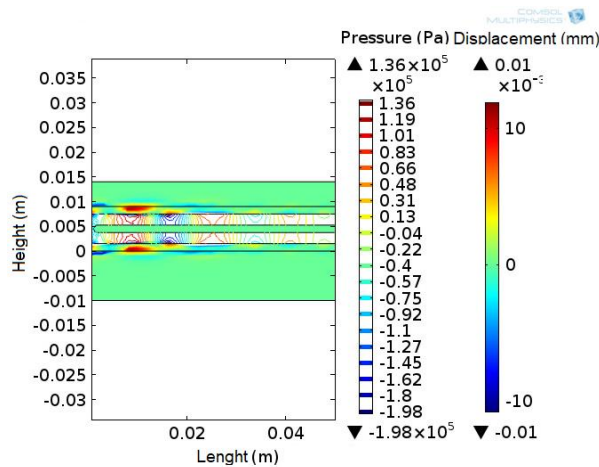


Fig. 50. The pressure fields and intensity of deformation at time point D, when the rod is at the end of the vibrational period. The left column shows pressure (Pa), while the right column shows displacement (mm).

Figures 47–50 graphically show blood velocity and acceleration. The size of the arrow varies according to the size of the vectorial field. The same four time points during the particular period were analyzed. The analysis shows nodes and antinodes that appear during the process. The distance between the nodes is about 10 mm. The intensity of deformation is the optimal on the first anti-node (at the tip of the waveguide) and gets smaller with each node towards the fixed part of the waveguide. The best blood vessel wall displacement appears at time point B and is -9.38×10^{-3}

mm. The best pressure to the inner wall of the blood vessel appears at time points A and C and is $\pm 7.85 \times 10^5$ Pa.

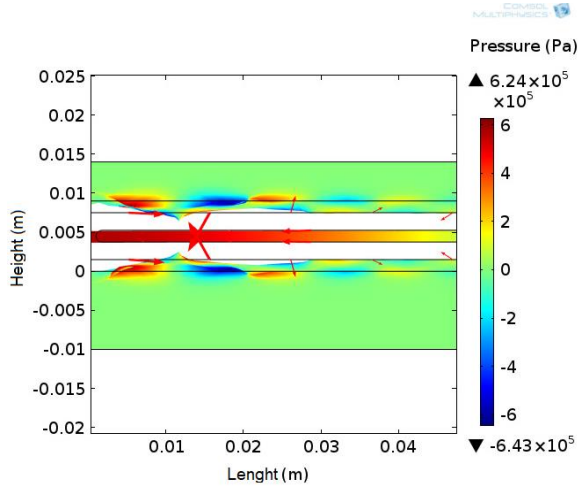


Fig. 51. The vectorial acceleration and blood velocity field at time point A.

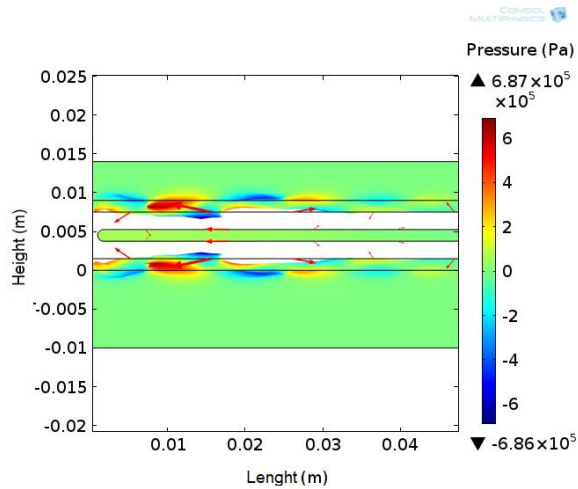


Fig. 52. The vectorial acceleration and blood velocity field at time point D.

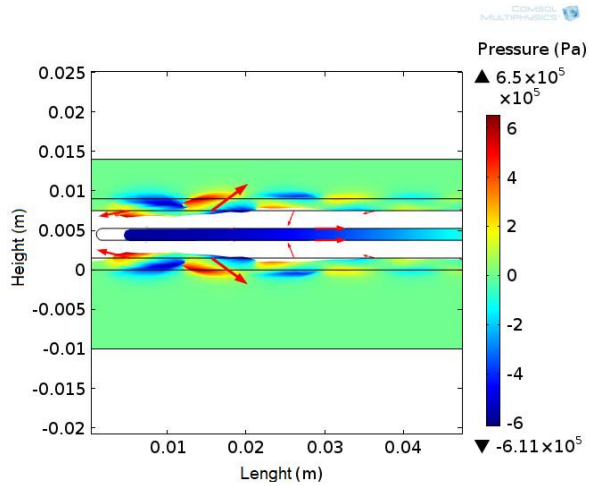


Fig. 53. The vectorial acceleration and blood velocity field at time point C.

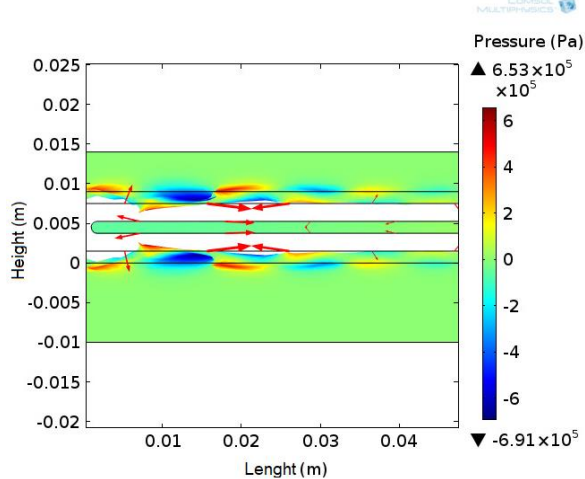


Fig. 54. The vectorial acceleration and blood velocity field at time point D.

The FEM modeling showed that an increased pressure field is generated while the ultrasound blood vessel cleaning system is working at its resonant frequency. The phenomenon of streaming at different flow rates in the direction of the blood flow appears as well. The streaming activates the destruction of the thrombus or another occlusive derivative inside the blood vessel.

3.4. Summary of Chapter 2

The waveguide of 260 mm in length and 1.5 mm in diameter has been developed for clearing blood vessels in the human body that is attached to the concentrator (a comprising part of the transducer) through a lug of a specific shape by using a screw (as the thread connection).

The FEM modeling of the simplified waveguide acting in close to real-life conditions (in a muscle-surrounded blood vessel filled with blood) showed that the best frequency for the greatest amount of frontal and transverse pressure is 24.970 kHz. While working in such a resonant mode, the best waveguide tip point displacement towards the z axis (forward) is 8.3 μm .

FEM modeling also allowed to determine the nodes and the anti-node dynamics through the length of the waveguide. It was determined that the most intensive (i.e., providing the optimal pressure and displacement of the surrounding fluids and tissues) value appears at the tip of the waveguide. The nodes and the anti-nodes recur each 10 millimeters and get lower (within their value) with each next anti-node. The analysis also showed that the process becomes stationary after 6×10^{-4} s after the vibrations of the rod start. After the process becomes stationary, the pressure of $\pm 5.05 \times 10^5$ Pa (positive and negative at different time points of the period) at the tip of the waveguide appears. This pressure is transferred through human blood and becomes lower ($\pm 2.40 \times 10^5$) at the middle point of the thrombus which is distanced from the tip of the waveguide at 1 mm.

Further analysis of the vectorial acceleration and blood velocity fields at different points of time of the period showed that the pressure to the inner wall of the blood vessel varies around $\pm 6.91 \times 10^5$ Pa depending on the time point of the period. Such a number is a bit lower if compared to the best pressure that appears at the tip of the waveguide at $\pm 7.86 \times 10^5$ Pa.

4. THEORETICAL INVESTIGATION OF THE TUBE-SHAPED WAVEGUIDE WIRE

The results presented in this chapter have been published in the following article: Kargaudas, V., Bubulis, A., Navickas, J., Vitkus, L., Venslauskas, M. Theoretical and Experimental Investigation of Tube-Shaped Waveguide Wire. *Journal of Measurements in Engineering* 5, 2017, 257–265.

The mathematical modeling of the waveguide and its interaction with the operational environment involved in the device is detailed in Figures 34 and 35. With the aim to gain better understanding of hydrodynamic processes, the modeling did not take into consideration the fact that the waveguide is normally operating in the second tube-catheter which serves to protect the blood vessel against negative notes distributed over the entire waveguide at particular steps of its length (experimentally determined nodes and antinodes will be covered in Chapter 4 that follows below). For the sake of simplicity of the mathematical model, it was also assumed that, when being operated, the tip of the waveguide moves in circles instead of ellipses. The working regime of the waveguide tip was selected based on the results obtained from the mathematical model described in Chapter 2.

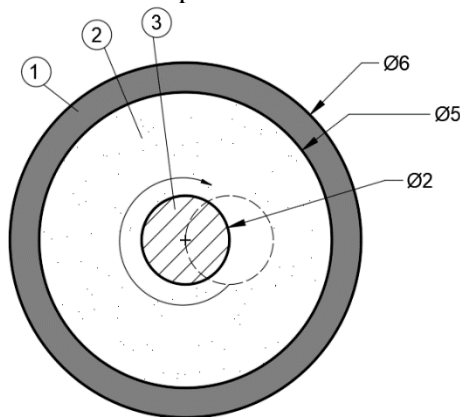


Fig. 55. Input data for the task being solved through modeling: 1) is the wall of the blood vessel, 2) is the liquid medium (blood), 3) is the tip of the waveguide moving in circles.

4.1. Sound Waves in Fluids

Let us assume that the tube moves slidingly in the plane xy , thus displacements of any point in directions of axes x, y can be defined as follows [86]:

$$\begin{cases} \xi_x = -b \cos \omega t, \\ \xi_y = b \sin \omega t. \end{cases} \quad (3.1)$$

The velocities of these points will then be as follows:

$$\begin{cases} v_x = b\omega \sin \omega t, \\ v_y = b\omega \cos \omega t. \end{cases} \quad (3.2)$$

where b is the amplitude of displacement, ω is the angular frequency in rad/s. The radial velocity of surface point B is described as follows:

$$v_r = v_x \cos \theta + v_y \sin \theta = b\omega \sin(\theta + \omega t). \quad (3.3)$$

Taking into account the fact that the tube is being flexed along the z axis, the radial component of the velocity is defined as follows:

$$v_r = b\omega \sin(\theta + \omega t) \cos \frac{2\pi z}{\lambda_z}, \quad (3.4)$$

where λ_z is the wave length of the tube deflection in the direction of the z axis.

The liquid surrounding the tube is considered to be of an/ideal pressure, consequently, the vibrations of the fluid are defined through the following differential equation:

$$\frac{\partial^2 \varphi}{\partial r^2} + \frac{1}{r} \frac{\partial \varphi}{\partial r} + \frac{1}{r^2} \frac{\partial^2 \varphi}{\partial \theta^2} + \frac{\partial^2 \varphi}{\partial z^2} = \frac{1}{c_\varphi^2} \frac{\partial^2 \varphi}{\partial t^2}. \quad (3.5)$$

The individual solution to the potential $\varphi = \varphi(r, \theta, z, t)$ can be proposed to be as follows:

$$\varphi_n = R_n(r) e^{i(n\theta + \omega t)} b \cos \frac{2\pi z}{\lambda_z}. \quad (3.6)$$

The incorporation of this into (3.5) results in a differential equation of Bessel as follows [86]:

$$R_n'' + \frac{1}{r} R_n' + \left(k_\varphi^2 - \frac{4\pi^2}{\lambda_z^2} - \frac{n^2}{r^2} \right) R_n = 0, \quad (3.7)$$

where $k_\varphi = \omega/c_\varphi$. The velocity of wave propagation in a fluid $c_\varphi = 14.7 \cdot 10^4 \text{ cm/s}$, with vibration frequency 21.8 kHz , thus $\omega = 13.7 \cdot 10^4 \text{ rad/s}$ and $k_\varphi = 0.932 \text{ cm}^{-1}$. If the wave length equals $\lambda_z = 4-5 \text{ cm}$, then $\frac{2\pi}{\lambda_z} = 1.26-1.57 \text{ cm}^{-1}$ resulting in the following:

$$k^2 = \frac{4\pi^2}{\lambda_z^2} - k_\varphi^2 = 0.72 - 1.59 \text{ cm}^{-2}. \quad (3.8)$$

Taking all the above into account makes a differential equation of Bessel (3.7) to be rearranged as follows:

$$R_n'' + \frac{1}{r} R_n' - \left(k^2 + \frac{n^2}{r^2} \right) R_n = 0. \quad (3.9)$$

Two independent solutions to this differential equation represent modified functions of Bessel, namely $I_n(kr)$ and $K_n(kr)$, thus solution (3.6) can be proposed to be formulated as follows:

$$\varphi_n = (D_n - iC_n) [I_n(kr) + iK_n(kr)] e^{i(n\theta + \omega t)} b \cos \frac{2\pi z}{\lambda_z}. \quad (3.10)$$

where D_n, C_n are constants. The physical meaning is carried by the real part of the complex function (3.6):

$$\begin{aligned} \varphi_n = & \left\{ [C_n I_n(kr) - D_n K_n(kr)] \sin(n\theta + \omega t) + \right. \\ & \left. + [C_n K_n(kr) + D_n I_n(kr)] \cos(n\theta + \omega t) \right\} b \cos \frac{2\pi z}{\lambda_z}. \end{aligned} \quad (3.11)$$

Differentiation results in real velocities and pressure within the fluid are as follows:

$$\begin{aligned} v_{ms} = \frac{\partial \varphi_n}{\partial r} = & \left\{ [C_n I'_n(kr) - D_n K'_n(kr)] \sin(n\theta + \omega t) + \right. \\ & \left. + [C_n K'_n(kr) + D_n I'_n(kr)] \cos(n\theta + \omega t) \right\} kb \cos \frac{2\pi z}{\lambda_z}, \end{aligned} \quad (3.12)$$

$$\begin{aligned} p_{ns} = \rho_\varphi \frac{\partial \varphi_n}{\partial t} = & \left\{ [C_n I_n(kr) - D_n K_n(kr)] \cos(n\theta + \omega t) - \right. \\ & \left. - [C_n K_n(kr) + D_n I_n(kr)] \sin(n\theta + \omega t) \right\} \rho_\varphi \omega b \cos \frac{2\pi z}{\lambda_z}. \end{aligned} \quad (3.13)$$

where ρ_φ is the fluid density. The real velocity and pressure are obtained by summing up in the following way:

$$v_{rs} = \sum_{n=1}^{\infty} v_{ms}, \quad p_s = \sum_{n=1}^{\infty} p_{ns}. \quad (3.14)$$

4.2. Sound Waves in a Tissue

The fluid is assumed to be confined by the tissue in the form of a concentric cylinder with the radius of $r_1 > r_o$, r_o representing the radius of the tube. To some extent, the simplest way to describe the effect of sound waves propagating within the fluid on the tissue is to use the hypothesis proposed by E. Winkler $p = -k_w \xi_r$, where p is the pressure on the tissue, ξ_r is the radial displacement of the tissue, k_w is the constant. Such a law might be applicable in case p and ξ_r are independent of angle θ , i.e., if the excitation of vibrations is pulsed. When p and ξ_r are dependent on θ , the determination of the coefficient of proportion k_w becomes somewhat difficult and complicated, and the very assumption hardly reflects the reality. For this reason,

it is assumed that the fluid is confined by a limitless tissue into which sound waves are transmitted, and they keep propagating further in a similar fashion as in a fluid. The computation of dynamics for the tissue is proposed in the following while taking into account only the radial displacements of the particles in the tissue. The wave propagation within a tissue is assumed to be of the same density as the wave propagation velocity within a fluid. Longitudinal waves are defined through the following equation [87, 88]:

$$\frac{\partial^2 \Phi}{\partial r^2} + \frac{1}{r} \frac{\partial \Phi}{\partial r} + \frac{1}{r^2} \frac{\partial^2 \Phi}{\partial \theta^2} + \frac{\partial^2 \Phi}{\partial z^2} = \frac{1}{c_i^2} \frac{\partial^2 \Phi}{\partial t^2}. \quad (3.15)$$

The wave velocity within a tissue is found as follows:

$$c_i^2 = \frac{\lambda + 2\mu}{\rho_i} = \frac{(1-\nu)E}{(1+\nu)(1-2\nu)\rho_i} = \frac{E_{ef}}{\rho_i}. \quad (3.16)$$

The modulus of elasticity for the tissue $E = 0.6 \text{ N/cm}^2$, Poisson's coefficient $\nu = 0.45$, density $\rho_i = 1000 \text{ kg/m}^3$ [89], thus $c_i = 477 \text{ cm/s}$ and wave number $k_i = \omega/c_i = 287 \text{ s}^{-1}$. Further, the constant is found:

$$\kappa = \sqrt{k_i^2 - \frac{4\pi^2}{\lambda_z^2}} = 287 \text{ cm}^{-1}. \quad (3.17)$$

If the solution for the tissue is proposed to be the following:

$$\Phi_n = P_n(r) e^{i(n\theta + \omega t)} b \cos \frac{2\pi z}{\lambda_z}, \quad (3.18)$$

then a differential equation of Bessel is obtained from (3.19) for the determination of function $P_n(r)$:

$$P_n'' + \frac{1}{r} P_n' + \left(k_i^2 - \frac{4\pi^2}{\lambda_z^2} - \frac{n^2}{r^2} \right) P_n = 0. \quad (3.19)$$

When taking into consideration totally different k_i values than that for fluid k_ϕ , independent solutions $J_n(\kappa r)$ and $Y_n(\kappa r)$ to Equation (3.19) are obtained [90]. The general solution to differential Equation (3.19) can be formulated as follows:

$$\Phi_n = (B_n - iA_n) [J_n(\kappa r) - iY_n(\kappa r)] e^{i(n\theta + \omega t)} b \cos \frac{2\pi z}{\lambda_z}. \quad (3.20)$$

The real part of potential Φ_n is as follows:

$$\Phi_n = [\alpha_n \sin(n\theta + \omega t) + \beta_n \cos(n\theta + \omega t)] b \cos \frac{2\pi z}{\lambda_z}. \quad (3.21)$$

where

$$\begin{cases} \alpha_n(r) = A_n J_n(\kappa r) + B_n Y_n(\kappa r), \\ \beta_n(r) = B_n J_n(\kappa r) - A_n Y_n(\kappa r). \end{cases} \quad (3.22)$$

The velocities of particles and pressure are proposed to be as follows:

$$v_{ra} = \frac{\partial \Phi_n}{\partial r} = \left[\alpha'_n(r) \sin(n\theta + \omega t) + \beta'_n(r) \cos(n\theta + \omega t) \right] b \kappa \cos \frac{2\pi z}{\lambda_z}, \quad (3.23)$$

$$p_{na} = \rho_i \frac{\partial \Phi_n}{\partial t} = \left[\alpha_n(r) \cos(n\theta + \omega t) - \beta_n(r) \sin(n\theta + \omega t) \right] \rho_i \omega b \cos \frac{2\pi z}{\lambda_z}. \quad (3.24)$$

Equations (3.11) and (3.23) contain hyphens which denote fluxions of the Bessel's functions with respect to their arguments but not with respect to r . Thus Equations (27) must be supplemented as follows:

$$\begin{cases} \alpha'_n(r) = A_n J'_n(\kappa r) + B_n Y'_n(\kappa r), \\ \beta'_n(r) = B_n J'_n(\kappa r) - A_n Y'_n(\kappa r). \end{cases} \quad (3.25)$$

Equations (3.22) and (3.23) contain separated solutions when $n = 1, 2, \dots$. The general solution for the tissues is obtained by summing up in the way it was done for the fluid in (3.14).

4.3. Conditions for the Existence of the Proposed Solution

Functions (3.12), (3.13), (3.23) and (3.24) used to define the velocities and pressures of the wave flow, in principle, remain unchanged over time t , thus steady-state flows in a fluid and in a tissue are the same at any moment in time only turned at certain angle. For this reason, the solution can be found at any t , for instance, at $t = 0$. In this case, by using $r = r_o$ and $r = r_1$ (i.e., on the surface of the tube and on the surface of the fluid-tissue contact), we obtain results in the Fourier series for functions $v_{rs}(r_o)$, $v_{ra}(r_1)$, $p_a(r_1)$. We hereby refer to the sums when $n = 1, 2, 3, \dots$. Factors (multipliers) at $\cos n\theta$, $\sin n\theta$ represent the Fourier coefficients for these functions. If two θ functions in range $[-\pi; +\pi]$ are equal, their Fourier coefficients are equal as well. And if all the coefficients are equal, all the functions in the function space $L_2(G)$ are equal, too [91]. For the purpose of determining functions constants C_n, D_n, A_n, B_n , $n = 1, 2, \dots$ are available. The following are the conditions that must be met by these functions:

$$v_{rs}(r_o) = b\omega \sin \theta \cos \frac{2\pi z}{\lambda_z}, \quad (3.26)$$

$$v_{rs}(r_1) = v_{ra}(r_1), \quad (3.27)$$

$$p_{rs}(r_1) = p_{ra}(r_1). \quad (3.28)$$

The first condition (3.26) was determined from (3.4). The following is obtained from (3.27) and (3.28), when $n = 1, 2, 3, \dots$:

$$\begin{cases} \alpha'_n(r_1) = C_n I'_n(kr_1) - D_n K'_n(kr_1), \\ \beta'_n(r_1) = C_n K'_n(kr_1) + D_n I'_n(kr_1), \\ \alpha_n(r_1) = C_n I_n(kr_1) - D_n K_n(kr_1), \\ \beta_n(kr_1) = C_n K_n(kr_1) + D_n I_n(kr_1). \end{cases} \quad (3.29)$$

Here, the incorporation of (3.22) and (3.25) results in a homogenous system of 4 linear algebraical equations for the calculation of constants A_n, B_n, C_n, D_n . The system of Equations (3.29) has nonzero solution only in case if the determinant is as follows:

$$\begin{vmatrix} J'_n(\kappa r_1) & Y'_n(\kappa r_1) & -I'_n(\kappa r_1) & K'_n(\kappa r_1) \\ Y'_n(\kappa r_1) & -J'_n(\kappa r_1) & K'_n(\kappa r_1) & I'_n(\kappa r_1) \\ J_n(\kappa r_1) & Y_n(\kappa r_1) & -I_n(\kappa r_1) & K_n(\kappa r_1) \\ Y_n(\kappa r_1) & -J_n(\kappa r_1) & K_n(\kappa r_1) & I_n(\kappa r_1) \end{vmatrix} = 0.$$

This is possible only for certain values of r_1 , and only for a few $n = 1, 2, 3, \dots$, but not all. Thus, conditions (3.27) and (3.28) cannot be met simultaneously.

It is assumed that the condition regarding pressure definitely must be met, but equations of velocities and displacements when $r = r_o$ and $r = r_1$ are compulsory not for every θ . Let us assume that gaps occur in between the fluid and the tube, and between the fluid and the tissue. Since the flow is in a steady state, the above-mentioned gaps that are hereinafter referred to as caverns, represent cavities filled with some gas or vapor and acquire the constant shape that remains unchanged over time. They tend to rotate jointly with the sliding motion of the tube, and their position should follow after the tube or tissue is moved in the opposite direction. Further research involves the calculation of caverns at the moment of time $t = 0$.

4.4. Description of Caverns

The cavern beside the tube is defined as the difference of velocities as follows [91]:

$$v_{rs}(r_o) - b\omega \sin \theta \cos \frac{2\pi z}{\lambda_z} = b\omega G^*(\theta) \cos \frac{2\pi z}{\lambda_z}, \quad (3.30)$$

when $\mathcal{G}^* - \lambda^* \leq \theta \leq \mathcal{G}^* + \lambda^*$ and $v_{rs}(r_o) - b\omega \sin \theta \cos \frac{2\pi z}{\lambda_z} = 0$ for every

other θ . Let us denote the reduced velocity as follows:

$$\tilde{v}_{rs} = \frac{v_{rs}}{b\omega \cos \frac{2\pi z}{\lambda_z}}, \quad (3.31)$$

then:

$$\begin{cases} \tilde{v}_{rs}^*(r_o) - \sin \theta = G^*(\theta), & \mathcal{G}^* - \lambda^* \leq \theta \leq \mathcal{G}^* + \lambda^*, \\ \tilde{v}_{rs}^*(r_o) - \sin \theta = 0, & \theta < \mathcal{G}^* - \lambda^*; \theta > \mathcal{G}^* + \lambda^*. \end{cases} \quad (3.32)$$

where λ^* is the angle to the centre of the tube cavern, $2\mathcal{G}^*$ is the angular width of the tube cavern.

The reduced velocity of the tissue is similarly defined:

$$\tilde{v}_{ra} = \frac{v_{ra}}{b\omega \cos \frac{2\pi z}{\lambda_z}} \quad (3.33)$$

and the tissue cavern equals:

$$\begin{cases} \tilde{v}_{ra} - \tilde{v}_{rs} = G(\theta), & \mathcal{G} - \lambda \leq \theta \leq \mathcal{G} + \lambda, \\ \tilde{v}_{ra} - \tilde{v}_{rs} = 0, & \theta < \mathcal{G} - \lambda; \theta > \mathcal{G} + \lambda. \end{cases} \quad (3.34)$$

Definitions (3.32) and (3.34) show that the functions of caverns $G(\theta)$ and $G^*(\theta)$ are defined in analogous manner, thus further calculations involve the description of tissue cavern $G(\theta)$ only, whereas the tube cavern is offered too, but only by writing up an asterisk.

If $G(\theta)$ represents an integrated periodic function within range $[\mathcal{G} - \lambda, \mathcal{G} + \lambda]$, the following can be formulated:

$$G(\theta) = e_o + \sum_{j=1}^{\infty} (g_j \sin j\theta + e_j \cos j\theta), \quad (3.34)$$

where g_j, e_j represent real numbers. In order to apply the outside conditions (3.26) and (3.27), function (3.35) must be regrouped into the periodic function over the entire range $[-\pi, +\pi]$ as follows:

$$\tilde{v}_{ra} - \tilde{v}_{rs} = f(\theta), \quad -\pi < \theta \leq +\pi, \quad (3.36)$$

$$f(\theta) = \frac{a_o}{2} + \sum_{n=1}^{\infty} (a_n \cos n\theta + b_n \sin n\theta), \quad (3.37)$$

where coefficients of Fourier series are as follows:

$$\begin{cases} \pi a_n = \int_{-\pi}^{\pi} f(x) \cos nxdx = \int_{\vartheta-\lambda}^{\vartheta+\lambda} G(x) \cos nxdx, \\ \pi b_n = \int_{-\pi}^{\pi} f(x) \sin nxdx = \int_{\vartheta-\lambda}^{\vartheta+\lambda} G(x) \sin nxdx. \end{cases} \quad (3.38)$$

Incorporation of (3.35) into (3.38) results in the following:

$$\pi a_n = \sum_{j=1}^{\infty} g_j h_{ajn} + \sum_{j=1}^{\infty} e_j q_{ajn}, \quad n = 0, 1, 2, \dots \quad (3.39)$$

Where:

$$h_{ajn} = \frac{\sin(j+n)\vartheta \sin(j+n)\lambda}{j+n} + \frac{\sin(j-n)\vartheta \sin(j-n)\lambda}{j-n} -$$

$$-2 \frac{\cos n\vartheta \sin n\lambda}{n} \cdot \frac{\sin j\vartheta \sin j\lambda}{j\lambda}, \quad j \neq n,$$

$$h_{ann} = \sin 2n\vartheta \frac{\sin n\lambda}{n} \left(\cos n\lambda - \frac{\sin n\lambda}{n\lambda} \right), \quad j = n,$$

$$q_{ajn} = \frac{\cos(j+n)\vartheta \sin(j+n)\lambda}{j+n} + \frac{\cos(j-n)\vartheta \sin(j-n)\lambda}{j-n} -$$

$$-2 \frac{\cos n\vartheta \sin n\lambda}{n} \cdot \frac{\cos j\vartheta \sin j\lambda}{j\lambda}, \quad j \neq n,$$

$$q_{ann} = \lambda + \frac{\cos 2n\vartheta \sin 2n\lambda}{2n} - 2 \frac{\cos^2 n\vartheta \sin^2 n\lambda}{n^2 \lambda}, \quad j = n.$$

The second equation in system (3.39) after function $G(x)$ is incorporated into it, allows other Fourier coefficients to be calculated as follows:

$$\pi b_n = \sum_{j=1}^{\infty} g_j h_{bjn} + \sum_{j=1}^{\infty} e_j q_{bjn}, \quad n = 1, 2, \dots \quad (3.40)$$

Here:

$$h_{bjn} = \frac{\cos(j-n)\vartheta \sin(j-n)\lambda}{j-n} - \frac{\cos(j+n)\vartheta \sin(j+n)\lambda}{j+n} -$$

$$-2 \frac{\sin n\vartheta \sin n\lambda}{n} \cdot \frac{\sin j\vartheta \sin j\lambda}{j\lambda}, \quad j \neq n,$$

$$h_{bnn} = \lambda - \frac{\cos 2n\vartheta \sin 2n\lambda}{2n} - 2 \frac{\sin^2 n\vartheta \sin^2 n\lambda}{n^2 \lambda}, \quad j = n,$$

$$q_{bjn} = \frac{\sin(j+n)\mathcal{G}\sin(j+n)\lambda}{j+n} - \frac{\sin(j-n)\mathcal{G}\sin(j-n)\lambda}{j-n} - 2\frac{\sin n\mathcal{G}\sin n\lambda}{n} \cdot \frac{\cos j\mathcal{G}\sin j\lambda}{j\lambda}, \quad j \neq n,$$

$$q_{bnn} = \sin 2n\mathcal{G} \frac{\sin n\lambda}{n} \left(\cos n\lambda - \frac{\sin n\lambda}{n\lambda} \right), \quad j = n.$$

If the position and the length of the cavern, i.e., numbers \mathcal{G} and λ are the selected ones, then all the h_{ajn} , q_{ajn} , h_{bjn} , q_{bjn} are known values.

The following can be obtained from (3.39), when $n = 0$:

$$\pi a_o = e_o + \sum_{j=1}^{\infty} \sin j\lambda \frac{g_j \sin j\mathcal{G} + e_j \cos j\mathcal{G}}{j\lambda}. \quad (3.41)$$

All the formulas proposed here can also be applied for the tube cavern by using \mathcal{G}^* and λ^* instead of \mathcal{G} and λ .

4.5. The Equations for the Determination of the Caverns

Next, particles' velocities (3.12) and pressure (3.13) in a fluid as well as particles' velocities (3.23) and pressure (3.24) in a tissue are to be found. For this purpose, constants C_n, D_n, A_n, B_n , $n = 1, 2, \dots$ need to be found. Since the solutions must meet Equations (3.26), (3.27) and (3.28) for every t and θ , there are 6 equations (factors at $\sin n\theta$ and $\cos n\theta$) for every n . Taking into account the caverns, Equation (3.27) is replaced with Equation (3.36), and Equation (3.26) with the following equation [92]

$$\tilde{v}_{rs}(r_o) - \sin \theta = f^*(\theta), \quad (3.42)$$

where

$$f^*(\theta) = \frac{a_o^*}{2} + \sum_{n=1}^{\infty} (a_n^* \cos n\theta + b_n^* \sin n\theta). \quad (3.43)$$

This is a Fourier series analogous to series (3.37) proposed above. This way, the equation of velocities when $r = r_o$ is satisfied for every t and θ if

$$\begin{cases} \bar{C}_n I'_n(kr_o) - \bar{D}_n K'_n(kr_o) = b_n^* + \delta_n, \\ \bar{C}_n K'_n(kr_o) + \bar{D}_n I'_n(kr_o) = a_n^*, \end{cases} \quad n = 1, 2, 3, \dots, \quad (3.44)$$

and the constant $\delta_1 = 1$ and $\delta_n = 0$ if $n > 1$. The first equation in Formula (3.44) represents multipliers at $\sin n\theta$, and the second one represents multipliers at $\cos n\theta$. Moreover, new constants have been incorporated into (3.44)

$$\bar{C}_n = C_n k/\omega, \quad \bar{D}_n = D_n k/\omega.$$

The equation of velocities (3.27) for the tissue when $r = r_1$, while taking into account the cavern and Equation (3.36), is formulated with the following system of equations:

$$\begin{cases} \bar{A}_n J'_n(\kappa r_1) + \bar{B}_n Y'_n(\kappa r_1) - \bar{C}_n I'_n(\kappa r_1) + \bar{D}_n K'_n(\kappa r_1) = b_n, \\ \bar{A}_n Y'_n(\kappa r_1) - \bar{B}_n J'_n(\kappa r_1) + \bar{C}_n K'_n(\kappa r_1) + \bar{D}_n I'_n(\kappa r_1) = -a_n. \end{cases} \quad (3.45)$$

where $n = 1, 2, 3, \dots$ and new constants are incorporated, too

$$\bar{A}_n = A_n \kappa / \omega, \quad \bar{B}_n = B_n \kappa / \omega.$$

The equation of pressure (3.28) is considered to remain the same when $r = r_1$, thus, taking into account the new constants, it results in the following:

$$\begin{cases} [\bar{C}_n K_n(\kappa r_1) + \bar{D}_n I_n(\kappa r_1)] \chi + \bar{A}_n Y_n(\kappa r_1) - \bar{B}_n J_n(\kappa r_1) = 0, \\ [\bar{C}_n I_n(\kappa r_1) - \bar{D}_n K_n(\kappa r_1)] \chi - \bar{A}_n J_n(\kappa r_1) - \bar{B}_n Y_n(\kappa r_1) = 0. \end{cases} \quad (3.46)$$

$$\text{Here, } \chi = \frac{\kappa}{k} \frac{\rho_\varphi}{\rho_i}.$$

The main problem here is the computation of constants g_n, e_n, g_n^*, e_n^* that are used to define caverns. For this reason, it is worth eliminating $\bar{C}_n, \bar{D}_n, \bar{A}_n, \bar{B}_n$ from the system of 6 equations (3.44), (3.45), (3.46). Formulation (3.46) can be further expressed as follows:

$$\begin{cases} \bar{A}_n = M_n \bar{C}_n - N_n \bar{D}_n, \\ \bar{B}_n = N_n \bar{C}_n + M_n \bar{D}_n, \end{cases} \quad (3.47)$$

where

$$M_n = \frac{I_n J_n - K_n Y_n}{J_n^2 + Y_n^2} \chi; \quad N_n = \frac{K_n J_n + I_n Y_n}{J_n^2 + Y_n^2} \chi.$$

Here, arguments for all the Bessel functions I_n, K_n are κr_1 , and for functions J_n, Y_n arguments are κr_1 .

The following can be expressed from the system of equations:

$$\begin{cases} \bar{C}_n = \tilde{M}_n a_n^* + \tilde{N}_n (b_n^* + \delta_n), \\ \bar{D}_n = \tilde{N}_n a_n^* - \tilde{M}_n (b_n^* + \delta_n). \end{cases} \quad (3.48)$$

Here:

$$\tilde{M}_n = \frac{\tilde{K}'_n}{\tilde{I}'_n{}^2 + \tilde{K}'_n{}^2}, \quad \tilde{N}_n = \frac{\tilde{I}'_n}{\tilde{I}'_n{}^2 + \tilde{K}'_n{}^2}$$

and arguments for each and every Bessel function are κr_1 .

Incorporating (3.47) and (3.48) into (3.45) results in the following equations:

$$\begin{cases} X_n a_n^* + Y_n (b_n^* + \delta_n) + b_n = 0, \\ Y_n a_n^* - X_n (b_n^* + \delta_n) + a_n = 0. \end{cases} \quad (3.49)$$

Here the following denotations are used:

$$\begin{cases} X_n = \tilde{M}_n R_n - \tilde{N}_n S_n, \\ Y_n = \tilde{N}_n R_n + \tilde{M}_n S_n, \end{cases} \quad (3.50)$$

$$\begin{cases} R_n = I'_n(\kappa r_1) - J'_n(\kappa r_1) M_n - Y'_n(\kappa r_1) N_n, \\ S_n = K'_n(\kappa r_1) - J'_n(\kappa r_1) N_n + Y'_n(\kappa r_1) M_n. \end{cases} \quad (3.51)$$

Numbers X_n, Y_n can be calculated, thus only two equations (3.49) are available for finding the constants g_n, e_n, g_n^*, e_n^* for every $n = 1, 2, 3, \dots$. If $n = 1, 2, \dots, N$, then total $2N$ equations and $4N$ parameters are obtained apart from four numbers $\mathcal{G}^*, \lambda^*, \mathcal{G}$ and λ .

The system of equations (3.49), as a result of incorporation of (3.39) and (3.40), turns out to be as follows:

$$\begin{cases} \sum_{j=1}^N (h_{ajn}^* X_n + h_{bjn}^* Y_n) g_j^* + \sum_{j=1}^N (q_{ajn}^* X_n + q_{bjn}^* Y_n) e_j^* + \\ \quad + \sum_{j=1}^N h_{bjn} g_j + \sum_{j=1}^N q_{bjn} e_j = -\pi Y_n \delta_n, \\ \sum_{j=1}^N (h_{ajn}^* Y_n - h_{bjn}^* X_n) g_j^* + \sum_{j=1}^N (q_{ajn}^* Y_n - q_{bjn}^* X_n) e_j^* + \\ \quad + \sum_{j=1}^N h_{ajn} g_j + \sum_{j=1}^N q_{ajn} e_j = \pi X_n \delta_n. \end{cases} \quad (3.52)$$

Constants e_o and e_o^* have been incorporated into the solution to cavern (3.35) and tube's cavern $G^*(\theta)$, having a physical meaning, such as the movement in the radial direction at a constant speed. Consequently, these constants must be equal to zero. The same is true about constants a_o, a_o^* . It can be obtained from (3.41) that if $a_o = 0$, it follows:

$$e_o = -\sum_{n=1}^N \sin n\lambda \frac{g_n \sin n\mathcal{G} + e_n \cos n\theta}{n\lambda}. \quad (3.53)$$

4.6. Displacements of the Caverns

Velocities have been investigated that were described in Equation (3.23) as periodic functions of argument $(n\theta + \omega t)$. Such an argument shows that with the change in angle θ by 2π or change in time by $T = 2\pi/\omega$, all the functions remain unchanged. Accordingly, it can be stated that the steady-state solution somewhat turns around the z axis without experiencing any changes.

For the sake of simplicity, the calculation of caverns involved, $t = 0$ which in turn resulted in a somewhat instantaneous picture of cavern (3.35) where $e_o = 0$. Since the cavern turns at the same angular velocity as the entire steady-state solution, the law of the cavern motion (3.35) must be generalized in the following manner:

$$G_r(\theta, t) = \sum_{j=1}^{\infty} g_j \sin(j\theta + \omega t) + \sum_{j=1}^{\infty} e_j \cos(j\theta + \omega t). \quad (3.54)$$

Here, it is understood that $e_o = 0$ was incorporated. When $r = r_1$, the velocities are $\tilde{v}_{ra} - \tilde{v}_{rs} = G_r(\theta, t)$, $\vartheta - \lambda \leq \theta \leq \vartheta + \lambda$. (3.55)

The integration of (3.54) and (3.55) by time results in the reduced displacements of the tissue and the fluid as follows:

$$\tilde{\xi}_{ra} - \tilde{\xi}_{rs} = \frac{1}{\omega} \sum_{n=1}^{\infty} e_n \sin(n\theta + \omega t) - \frac{1}{\omega} \sum_{n=1}^{\infty} g_n \cos(n\theta + \omega t) + \frac{c_\xi}{\omega}. \quad (3.56)$$

Here, c_ξ represents the constant that generally can be a function of angle θ . As it can be understood from (3.53), the actual displacements can be assumed to be as follows:

$$\xi_{ra} - \xi_{rs} = \left[\sum_{n=1}^{\infty} e_n \sin(n\theta + \omega t) - \sum_{n=1}^{\infty} g_n \cos(n\theta + \omega t) + c_\xi \right] b \cos \frac{2\pi z}{\lambda_z}. \quad (3.57)$$

Here, b represents the amplitude of the sliding displacement of the tube. Incorporating $t = 0$ allows obtaining the form of the cavern when $\vartheta - \lambda \leq \theta \leq \vartheta + \lambda$:

$$\xi_{as} = \left(c_\xi + \sum_{n=1}^{\infty} e_n \sin n\theta - \sum_{n=1}^{\infty} g_n \cos n\theta \right) b \cos \frac{2\pi z}{\lambda_z}. \quad (3.58)$$

The tube's cavern is defined in ideally the same manner:

$$\xi_{sv} = \left(c_\xi^* + \sum_{n=1}^{\infty} e_n^* \sin n\theta - \sum_{n=1}^{\infty} g_n^* \cos n\theta \right) b \cos \frac{2\pi z}{\lambda_z}. \quad (3.59)$$

The determination of constants c_ξ, c_ξ^* requires additional physical data that should be associated with the pressure and gas flow within the caverns.

Since $\lambda \neq 0$, as otherwise it would mean that the cavern simply does not exist, and $\lambda \neq \pi$, as in this case the cavern would be present around the entire perimeter of

θ , then, as it can be understood from (3.53), in order to have $e_o = 0$, it must be as follows:

$$g_n \sin n\vartheta + e_n \cos n\vartheta = 0, \quad n = 1, 2, 3, \dots \quad (3.60)$$

If $\cos n\vartheta \neq 0$ and $\cos n\vartheta^* \neq 0$ at every $n = 1, 2, 3, \dots, N$, then it can be derived from (3.60) that $e_n = -g_n \tan n\vartheta$, $e_n^* = -g_n^* \tan n\vartheta$ and incorporated into (3.52). If $\sin n\vartheta \neq 0$ and $\sin n\vartheta^* \neq 0$, $n = 1, 2, 3, \dots, N$, then it can be expressed as g_n, g_n^* , and result in equations with the unknown quantities e_n, e_n^* . However, there is always a good chance that any of the factors $\tan n\vartheta, \tan n\vartheta^*$ (or $1/\tan n\vartheta, 1/\tan n\vartheta^*$) can turn out to be infinitely huge and impede our computation. The simplest option is apparently to write $2N$ equations (3.52) and then to supplement them with N equations (3.60) and N following equations:

$$g_n^* \sin n\vartheta + e_n^* \cos n\vartheta = 0, \quad n = 1, 2, 3, \dots \quad (3.61)$$

This way, the system of $4N$ linear equations is obtained with $4N$ unknown quantities g_n, e_n, g_n^*, e_n^* .

When making an assumption regarding the existence of caverns, the outside conditions (3.26) and (3.27) were modified, but the equation of pressure (3.28) was kept the same. This equation, as a matter of fact, must also be slightly modified if the solution of the cavern gas dynamics is to be taken into account. This would in turn affect the entire system of equations described above in this chapter.

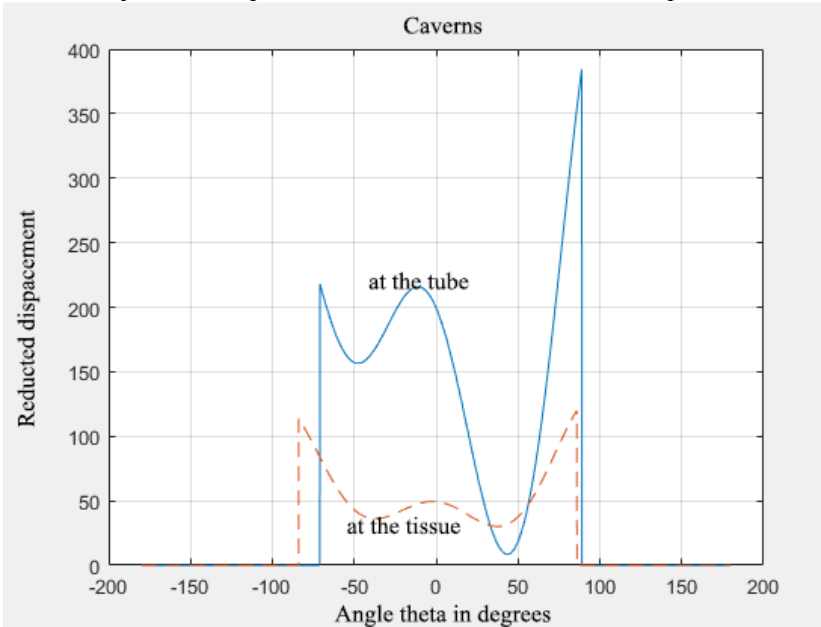


Fig. 56. Formation of caverns (that of the tube is the solid line, that of the tissue is the dotted line)

Both caverns, that of a tube and that of a tissue, are described by a general system of equations. The movement and the appearance of the caverns is shown in Fig. 56. Both caverns are interdependent and cannot be investigated separately one by one.

The calculation of the pressure at the tip of the waveguide, the pressure at the beginning of the tissue, and pressure as the function of distance in the infinite fluid and environment considering the cavern phenomena are shown in Figures 57, 58 and 59.

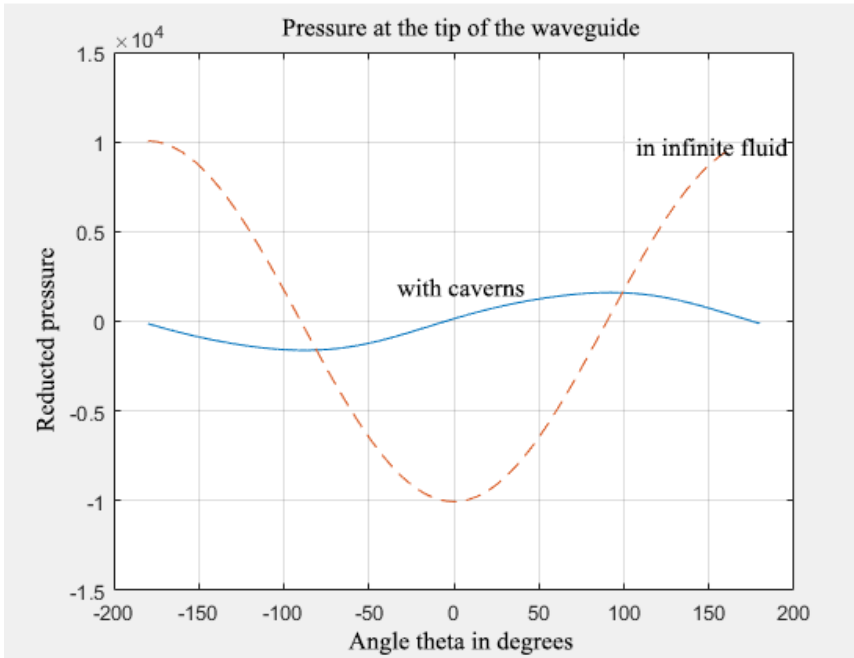


Fig. 57. Pressure on the tip of the waveguide.

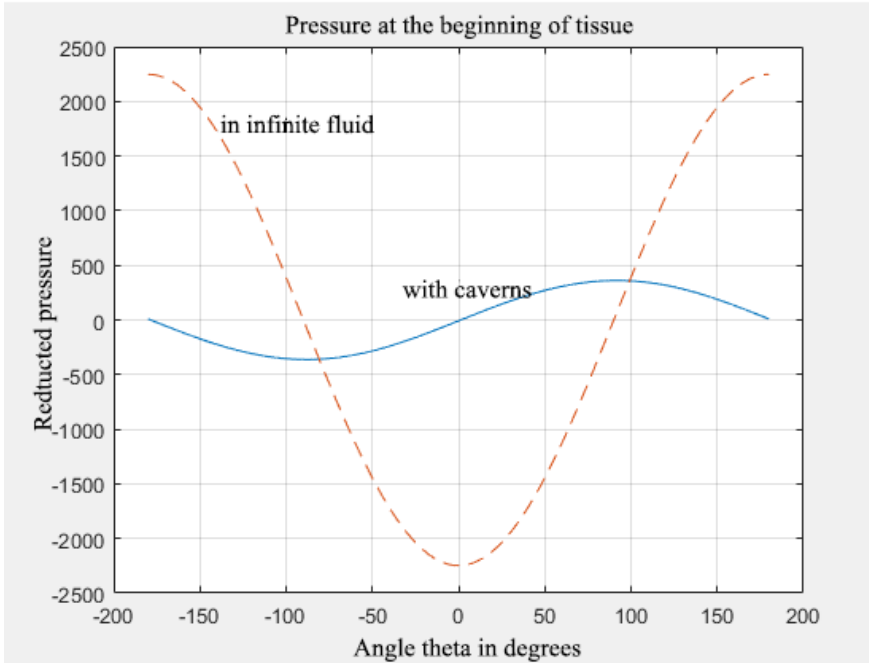


Fig. 58. Pressure at the beginning of the tissue.

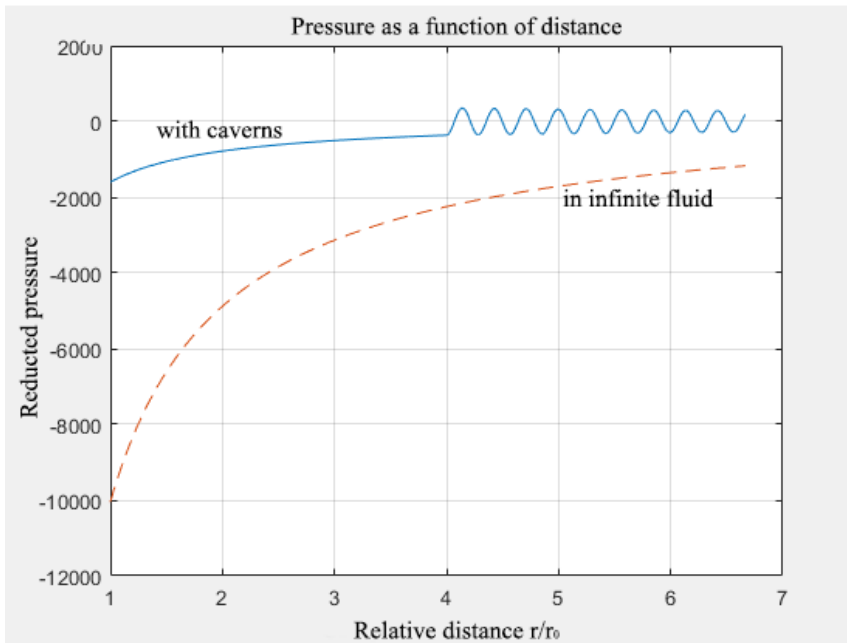


Fig. 59. Pressure as the function of distance. The dotted line is in an infinite (non-limited) fluid.

4.7. Calculation of the Size of the Cavern

Solving the task of modeling led us to the observation that during the operation of the ultrasonic system, a cavity containing tenuous gas, here referred to as the cavern, is formed at the wall of the blood vessel. Section 3.7 offers the calculation of its width.

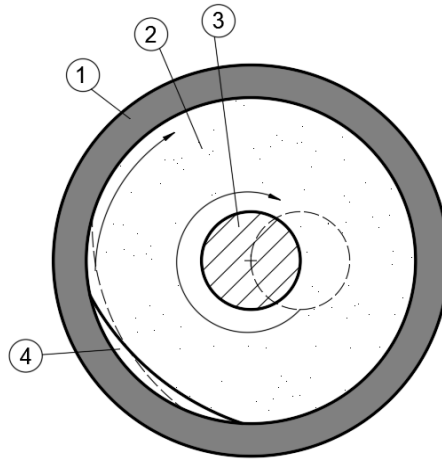


Fig. 60. Formation of the cavern where 1) is the wall of the blood vessel; 2) is a liquid environment (blood); 3) is the tip of the waveguide; 4) is the cavern.

The thickness of the outside layer can be calculated when the surface is vibrating at 23.185 kHz frequency in its own plane as follows:

$$\delta = \sqrt{\frac{\nu}{\omega}} = \sqrt{\frac{0.73 \cdot 10^{-2}}{13.7 \cdot 10^4}} = 0.23 \cdot 10^{-3} \text{ cm} = 2.3 \mu$$

Here, viscosity of water is incorporated $\nu = 0.73 \cdot 10^{-2} \text{ cm}^2/\text{s}$ at a temperature of 35° C . The vibration frequency is $\omega = 13.7 \cdot 10^4 \text{ rad}/\text{s}$.

4.8. Summary of Chapter 3

The mathematical model of the waveguide and its operational environment, in this particular case – human blood, confined by biological human tissues (the wall of a blood vessel) has been developed.

In the course of the solution of the mathematical task, a highly important phenomenon was revealed: with the waveguide operating under the resonant regime, a pocket containing tenuous gas of a size of up to $2.3 \mu\text{m}$ is formed at the wall of the blood cell that keeps sliding along the wall of the blood cell at a speed of the waveguide rotation. It can have a significant effect on the energy balance in the medium in which the waveguide is operated and may also significantly affect the absorption of drugs through the wall of the blood vessel and may exert influence on a

large scale thus enhancing the effect that the ultrasonic system has on the occluding malformation of the vascular walls.

This phenomenon has not yet been addressed and requires to be experimentally investigated in further research.

5. EXPERIMENTAL INVESTIGATION OF THE TUBE-SHAPED WAVEGUIDE WIRE WAVEGUIDE SYSTEM

5.1. Equipment Used for the Research

The ultrasonic system under consideration has been designed to operate jointly with *Ultrasound Generator VT-400* and a non-standard transducer constructed *in situ*. The descriptions of the ultrasound generator capable of operating under the pulsed regime and of the piezo-transducer are offered below. Unless specified otherwise, all the experiments under consideration here involved these two non-standard parts of the system.

5.1.1. Ultrasound Generator VT-400

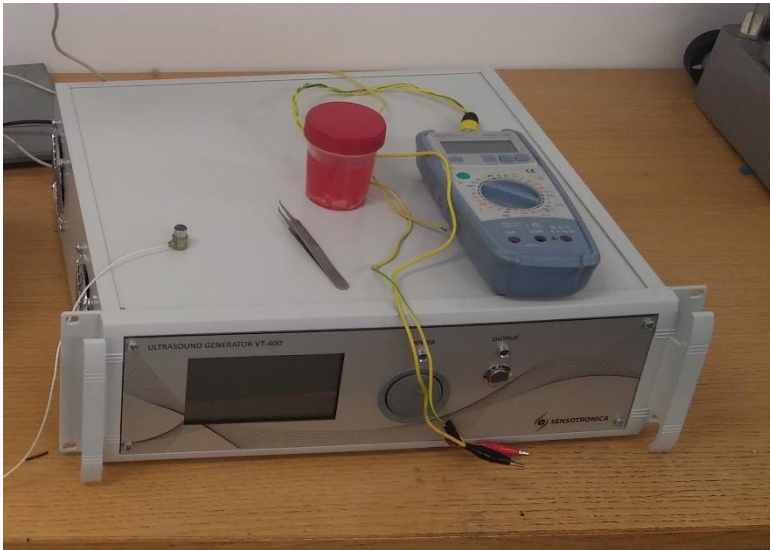


Fig 61. Ultrasound generator VT-400.

The main technical characteristics of the ultrasound generator are described in Table 2.

Table 2. The technical characteristics of ultrasound generator *VT-400*

Supply voltage, V	200-240
Output power, W	Up to 400
Number of channels	1
Output frequency, kHz	15-60
Dimensions, mm	300×425×135
Capacity, W	500

5.1.2. The Ultrasound Transducer

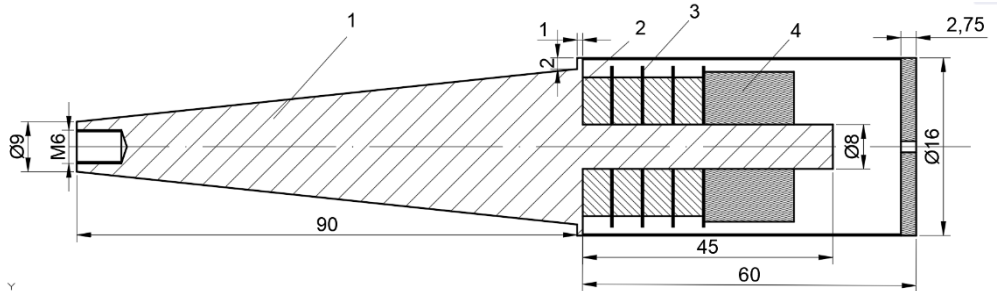


Fig. 62. The construction of an ultrasonic blood vessel cleaning system, where: 1) is the conical concentrator 2) is a piezo ceramics ring, 3) is a copper ring, 4) is the pressing element.

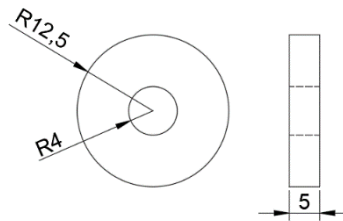


Fig. 63. Dimensions of the piezo ring used in the transducer of the ultrasonic system.

The ultrasound transducer is comprised of the conical concentrator (1) and four piezo ceramic rings PZT-4 (2) with the diameter of 25 mm and thickness of 5 mm that are fitted on the conical concentrator and spaced by copper rings with the diameter of 0.5 mm and paper insulation. The entire system is reinforced by the fastening component made of stainless steel with a thickness of 16 mm which is smaller by 1 mm in diameter (4).

5.2. Effect of Low Intensity Cavitation on Isolated Human Arteries

The results described/presented in this chapter have been published in the following article: Bubulis, A., Garalienė, V., Jurėnas, V., Navickas, J., Giedraitis, S. Effect of Low-Intensity Cavitation on the Isolated Human Thoracic Artery *in Vitro*. *Ultrasound in Medicine and Biology* 43, 2017, 1040–1047.

The experiments have been conducted on isolated human thoracic artery samples. The samples were collected during conventional myocardial revascularisations in patients who underwent coronary artery bypass grafting in the Department of Cardiothoracic and Vascular Surgery at the Lithuanian University of Health Sciences. All the patients chose to sign a letter of informed consent. The study was approved by the Regional Ethics Committee of Biomedical Research on the 5th of November 2010, licence No. BE-2-64, in Kaunas, Lithuania.

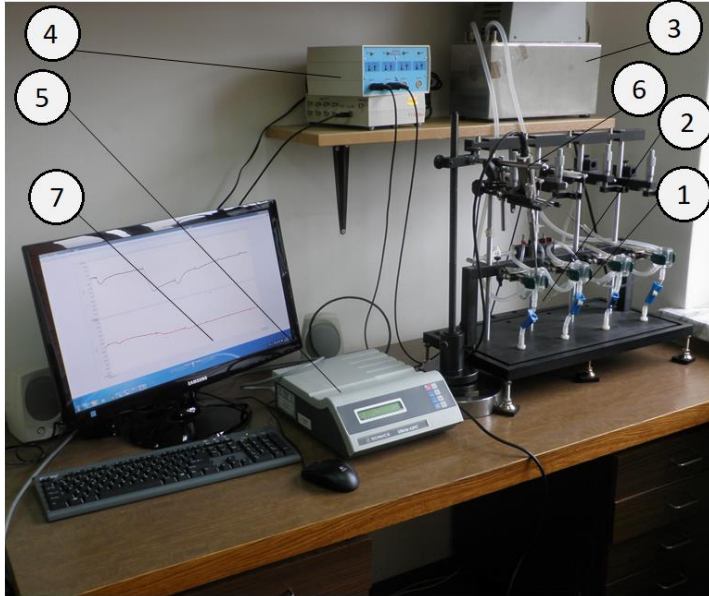


Fig. 64. Experimental set-up for the ultrasonic treatment of blood vessel samples, where 1) is the *EZ-Bath Tissue/Organ Bath System*; 2) are tissue baths; 3) is the pre-warming system (thermostat); 4) is the L-BRAM4 Bridge Amplifier; 5) is the Ultrasonic processor VCX130PB; 6) is the Piezoelectric transducer and its probe; 7) is a PC monitor.

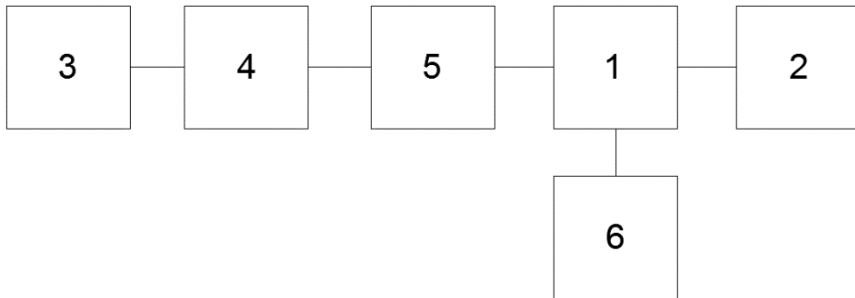


Fig. 55. The experiment scheme, where: 1) is the *EZ-Bath Tissue/Organ Bath System*; 2) is the bath pre-warming system; 3) is the ultrasonic processor VCX130PB; 4) is the L-BRAM4 Bridge Amplifier; 5) is the piezoelectric transducer and its probe; 6) is a PC.

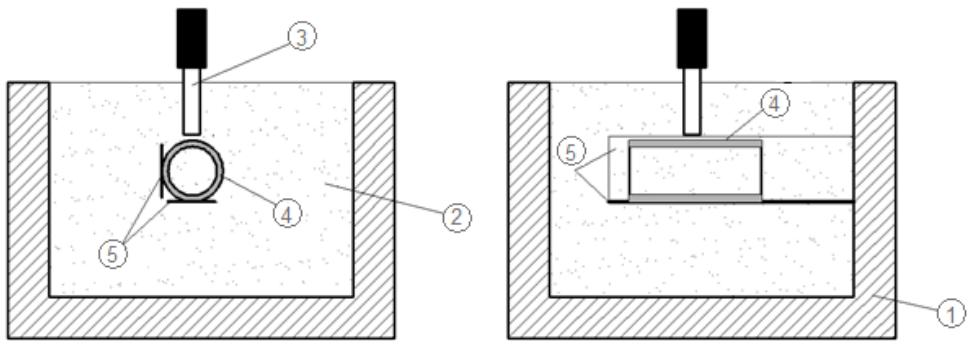


Fig. 66. The scheme of our experiment, where 1) is the water tank; 2) is the physiological fluid; 3) is the ultrasound transducer; 4) is the blood vessel; 5) are blood vessel holders.

The artery samples were obtained from a total of 152 patients. Their age average was 67.3 ± 9.6 years. Women accounted for 30.7 percent of the total number of the patients involved.

Vascular preparation. For the purpose of investigating blood vessel segments *in vitro*, a tissue/organ bath system produced by the *Global Town Microtechnology Company* (Sarasota, FL, USA) was used. The artery samples were collected at the ambient temperature from patients undergoing coronary artery bypass grafting. Afterwards, the samples were gently cleansed of the connective tissue, then carefully cut into 3–4 mm long rings and hung on a vascular holder. The upper hook of the vascular holder was attached to an isometric force transducer. The samples were dipped into 5 ml tissue baths filled with Tyrode's solution that was warmed to 37°C and continuously bubbled with 100 % oxygen. The composition of the solution was as follows (in mM): NaCl, 137; KCl, 5.4; CaCl_2 , 1.8; MgCl_2 , 0.9; Tris HCl, 10; and glucose, 5; $\text{pH} = 7.4$. Prior to starting the experiments, the blood vessel samples were allowed to equilibrate for at least 45–60 min. Throughout the investigation period, the preparations were periodically (every 15 min) washed with fresh Tyrode's solution.

With the aim to examine the effect of the ultrasound, an irradiation to the side and the open end of the blood vessel was performed. For this purpose, the contraction and relaxation process was invoked, then, an equilibration period followed, and, finally, the isolated vascular samples were exposed to discontinuous ultrasound pulse for a period of ten or twenty seconds. The tip of the transducer was positioned at the distance of 0.5 cm to the sample surface or along the vessel lumen.

Protocol. The first series of experiments involved studying the isometric contraction and relaxation effects in artery rings when phenylephrine-induced contraction was produced by zero, 10 and 20 min after exposing them to 10 s ultrasound pulse. Phenylephrine solution at 10^{-4} M concentration was used in all the experiments under consideration. Phenylephrine acts as a vasoconstrictor, i.e., it binds to α_1 -adrenoceptors located at the surface of sarcolemma, and activates the enzyme phospholipase C which is responsible for the synthesis of inositol 1,4,5-triphosphate (IP_3). The latter affects inositol 1,4,5-triphosphate receptors (IP_3R) that are localized

on the surface of the sarcoplasmic reticulum (SR) in the vascular smooth muscle and that prevail there [92, 93]. At the same time, the sarcolemma depolarizes, and external calcium enters through L-type Ca^{2+} channels into the cell. Due to the interaction of IP_3 with IP_3 receptors, the calcium ions entered into cytosol initiate Ca^{2+} release from the SR. Consequently, the more Ca^{2+} ions accumulate in the SR, the more of them should move into the cytoplasm during depolarization. As a result, the isometric contraction of the smooth muscle is forced to increase proportionally [94].

The effects of ultrasound on the functioning of the endothelium or slow (L-type) calcium channels within the vessel rings was assessed by examining the relaxation response to carbachol, an agonist of muscarinic acetylcholine receptors [95] and diltiazem, an inhibitor of the slow calcium channel [96]. Once the phenylephrine-produced isometric contraction has reached its steady state, the above mentioned agents were added to the solution in a cumulative-concentration manner, at doses of 10^{-7} – 10^{-4} M. The time course of the exerted force was recorded. The relaxation and isometric contraction forces were expressed in percentages and in mN (milinewtons), respectively, of the vasoconstrictor induced pre-contraction.

Subsequently, the second series of experiments was undertaken. In order to determine whether the blocking of the slow calcium channel alters the effect that ultrasound irradiation has on the contraction force of vessel segments, the samples were pre-treated with diltiazem in accordance with the following scheme: after leaving the rings for 30 min in Tyrode's solution to achieve their equilibration state, diltiazem was added into the bath at a concentration of 50 μM , and ultrasound was applied at 20 min after diltiazem had been added.

In control groups, the vessel samples were taken from the same patients as in the experimental groups, and all the measurements were carried out in parallel.

Drugs and chemicals used. Carbamylcholine chloride (carbachol), phenylephrine chloride (phenylephrine) and diltiazem (CAS No. 42399-41-7) were obtained from *Sigma-Aldrich Chemie* (Taufkirchen, Germany). They were dissolved in deionised water to obtain a stock solution of 0.1 mM. All the stock solutions were stored at a low temperature.

Statistics. The statistical analysis was performed by using *SPSS (Statistical Package for the Social Sciences)* software packed version 10.0. All the values obtained were expressed as means \pm SEM. The statistical significance was defined as $P < 0.05$.

Results

The effects of ultrasound irradiation on the contraction force in the isolated human thoracic samples are detailed below.

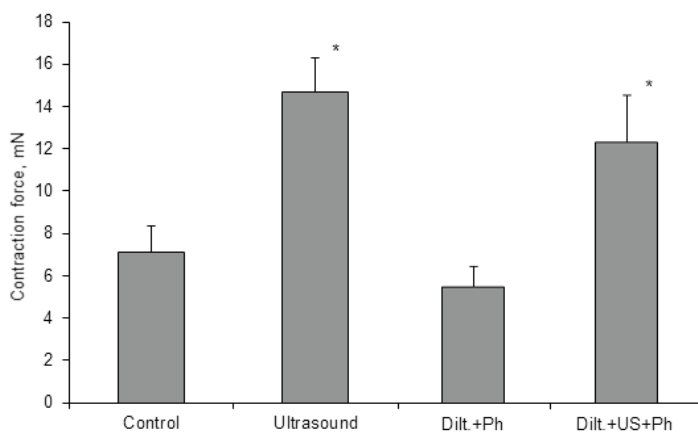


Fig. 67. The effect of 10-second US irradiation with and without diltiazem on the response of the contraction force in the isolated human *a. thoracica* rings (n=20) pre-contracted with Ph (10⁻⁴M) 10 min after the start of the US; n is the number of artery samples. *p < 0.01. The results are expressed as means ± SE.

The results depicted in Fig. 67 show a significant increase in the contraction force in the ultrasound group (51.6%, p < 0.01) exposed to 10-second ultrasound irradiation pulses and where vasoconstrictor phenylephrine (Ph, 10⁻⁴ M) was used 10 min after applying the pulse.

Similar data was obtained with the exposure of the artery segments to 20 s ultrasound irradiation, leading to the observation that, under the experimental conditions, the amount of ultrasound irradiation had no significant effect on the ratio of the contraction forces (12.4 ± 1.86 mN and 6.36 ± 1.3 mN, 48.4%, p < 0.01, respectively, in the groups exposed and not exposed to ultrasound) when the experimental groups were compared to the control groups.

The time that passed between the ultrasound exposure and vasoconstriction was found not to influence the level of the contraction ratio. Phenylephrine used immediately after the exposition to ultrasound resulted in an increased contraction force to 20.0 ± 2.8 and 9.2 ± 1.6 mN in the control group, respectively (ratio of ~ 2:1, 54 %, p < 0.01). Meanwhile, the increase of the time up to 20 minutes proved the assumption to be true that the effects of ultrasound are relatively long-lasting when compared to the artery lifespan *in vitro*. Therefore, in the case under consideration here, the isometric contraction of blood vessel samples in response to Ph remained significantly increased (16.63 ± 3.0 mN) compared to the ultrasound-free group (8.0 ± 1.66 mN), but were lower (minus 3.34 mN, 16.7 %) than the measurements taken immediately after irradiation with ultrasound.

To determine the influence of the slow calcium channel blocking on the isometric contraction of artery samples exposed to ultrasound irradiation, diltiazem, a well-known inhibitor of slow calcium channels, was used. For this purpose, blood vessel samples in both groups were immersed in a diltiazem solution of 50 μM concentration for 30 min. Throughout this period, the experimental group (20 min

after the immersion in diltiazem solution) was treated with 10-second ultrasound irradiation. The response of isometric contraction is presented in Fig. 67. Thereby, pre-treatment with diltiazem resulted in a smaller increase of contraction in both groups (12.16 ± 2.2 mN in the experimental group and 5.4 ± 1.04 mN in the US-free group, compared to the data presented in Fig. 67, where the experimental results were obtained under the same conditions, though the data values did not differ among themselves ($p > 0.05$). It means that the basic amount of calcium involved in the contraction mechanism is not from the outside of the cells, but is released from the internal resources, such as sarcoplasmic reticulum or mitochondria. Moreover, it means that this process is enhanced by ultrasound cavitation.

The following trials were performed on the same vessel segments of the thoracic artery; however, the ultrasound irradiation was used along the vessel lumen. The recorded response showed that, under conditions of 10-second internal ultrasound irradiation, the augmentation of the contraction force more than doubles ($\sim 2.3:1$) compared to the control (US-free; Ph was used 10 min after the exposure of the pulse of ultrasound).

An increase of the external irradiation frequency from 20 kHz to 32.6 kHz caused a greater increase of isometric contraction, and the ratio of contraction forces under those conditions was 2.46:1 (at 20 kHz, it was $\sim 2:1$; Fig. 67).

Consequently, the experimental results suggest that the isometric contraction of a smooth muscle in the isolated human *a. thoracica* segments is sensitive to the cavitation induced by the ultrasound pulse, and increases with the increase in ultrasonic frequency.

The effects of ultrasound irradiation on the vascular smooth muscle relaxation induced by carbachol and diltiazem are detailed below.

A hypothesis was raised that the low intensity cavitation induced by low-frequency ultrasound could restore the endothelial dysfunction stemming from systemic atherosclerosis. For the purpose of verifying this hypothesis, carbachol (Ch), an agonist of muscarinic M receptors whose effects are realized through the endothelial-dependent release of relaxing factors based on nitric oxide, a key vasodilator, was used. [97]

As studies have shown, the relaxation of blood vessels (as a response to Ch) treated with ultrasound irradiation is not unequivocal and is independent of the ultrasound frequency, irradiation time and the period of time passed since the start of exposition to ultrasound.

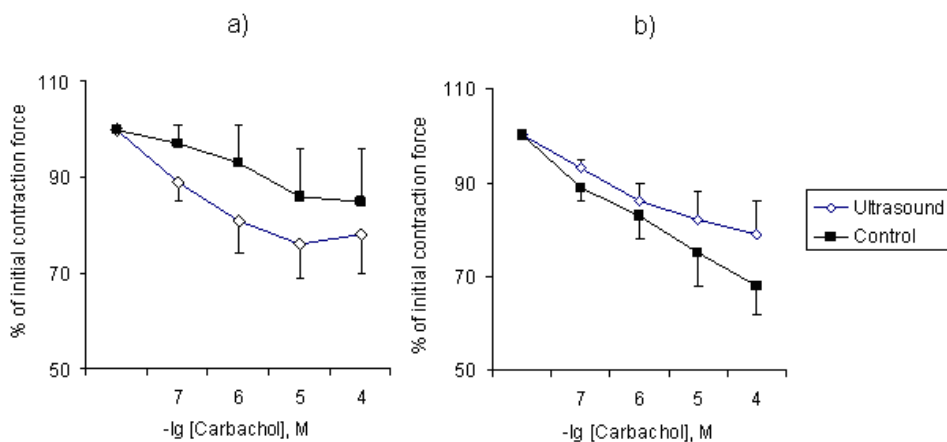


Fig. 68. a) Influence of 10-second US on the relaxation of isolated *a. thoracica* segments (n=15) induced by Ch (10⁻⁷ – 10⁻⁴M); the segments were pre-contracted with Ph (10⁻⁴ M) immediately after the start of US. b) Influence of 10-second US on the relaxation of isolated *a. thoracica* segments (n=14) induced by Ch (10⁻⁷ – 10⁻⁴M); the segments were pre-contracted with Ph (10⁻⁴ M) 20 min after the start of the US pulse; n is the number of artery samples. The results are expressed as means ± SE.

Accordingly, the data presented in Fig. 68a and Fig. 68b clearly shows that the time period from the start of irradiation with ultrasound to vasoconstriction has no significant effect on the smooth muscle relaxation process.

Regardless of whether the blood samples were pre-contracted with Ph immediately after the start of the exposure to ultrasound or 20 min afterwards, a similar relaxation process was observed. Therefore, the relaxation began in all the groups at a dose of 10⁻⁷ M of Ch, and varied within the range of 3 % to 11 %. An increase in the Ch dose caused the relaxation to slightly increase, as well, and at a concentration of 10⁻⁴ M, the relaxation reached 22.5 % and 21.3 % in the ultrasound-treated groups (in Fig. 68a and Fig. 68b, respectively). The differences between the control and the experimental groups as well as between the control groups in both events were not significant (p > 0.05).

As it was noted above, internal ultrasound irradiation more than doubled (by approx. 2.3 times), and the increase in the contraction force compared to the control group was observed. Such a significant increase in isometric contraction indicates the increased number of free intracellular calcium ions that are generally involved in the smooth muscle contraction process [98]. However, a question arises whether the smooth muscle cells are able to sequester the excess Ca to naturally induce their relaxation; otherwise said, the question is whether the smooth muscle cells remain viable after their exposure to ultrasound. With the aim to answer this question, the relaxation process of segments was recorded in real time when an experimental group was treated with internal ultrasound for 10 seconds and 10 min after the vasoconstrictor (phenylephrine) was used. The obtained results are presented in Fig. 69.

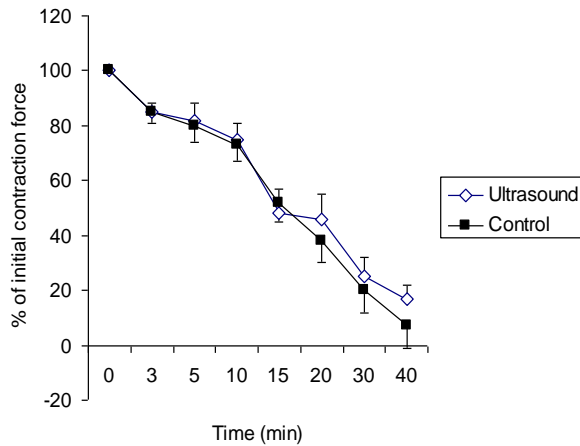


Fig. 69. Influence of 10-second internal US irradiation on the relaxation of blood vessel segments (n=13) over time; a vasoconstrictor (Ph, 10^{-4} M) was used 10 min after the start of the US pulse; *n* is the number of artery samples. The results are expressed as means \pm SE.

Thus a single dose of phenylephrine was observed to induce contraction of 26.16 mN and 11.61 mN, on average, in the ultrasound-treated and control groups, respectively (the ratio is approx. 2.25:1, 55.6 %, $p < 0.01$). Given such a difference in contraction forces, it was speculated whether or not this increased intercellular calcium concentration would slow the relaxation movement to some extent and thereby slow the relaxation of segments in the treated group. The taken measurements showed the relaxation magnitude to be very similar in both groups. At 40 min, it reached 82.5 % and 93 % in the ultrasound group and the control group, respectively. This difference was not statistically significant.

A similar response of the smooth muscle to carbachol was observed while using internal as well as higher frequency ultrasound irradiation (32.6 kHz). Accordingly, the obtained experimental data showed that low intensity cavitation induced by low frequency ultrasound irradiation has no effect on endothelium-dependent relaxation in isolated human blood vessels.

For the the next experimental study, diltiazem was used. Interestingly, diltiazem was observed to decrease the isometric contraction of the blood vessel segments by approx. 25 percent in the control group, and approx. 17.3 percent in the ultrasound-treated group in comparison to those without diltiazem.

Meanwhile, the relaxation dynamics of the vessel segments treated by diltiazem was not different from the control group (which included vessel segments not treated by diltiazem) (Fig. 70). In other words, ultrasound irradiation has no effect on relaxing the properties of diltiazem. Thus using it in a concentration-dependent manner gradually relaxed the segments, and its influence did not differ from the control group. For instance, at a dose of 10^{-4} M of diltiazem, the smooth muscles exposed to ultrasound were observed to relax to 50.4 percent. In the control group, the results were very similar (47.5 percent).

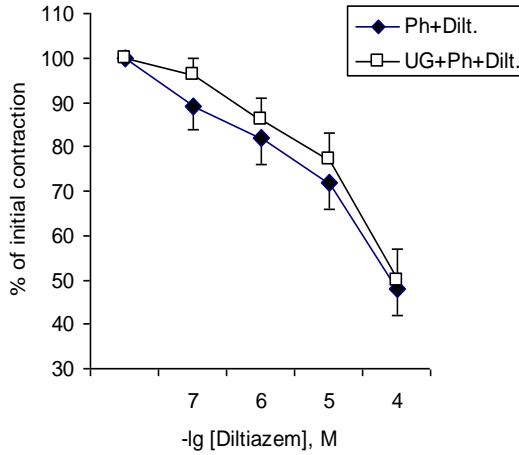


Fig. 70. Influence of diltiazem (Dilt.) on the relaxation of artery segments ($n=12$); a vasoconstrictor (Ph, 10^{-4} M) was used 10 min after the start of 10-second US exposure; n is the number of artery samples. The results are expressed as means \pm SE.

It follows from this study that low intensity cavitation induced by low-frequency ultrasound exposure does not affect the relaxation of smooth muscle associated with a slow calcium channel.

Experiments conducted on isolated human artery thoracic segments *in vitro* are influenced by low-intensity cavitation induced by low-frequency (4–6 W/cm², 20 kHz and 32.6 kHz) ultrasound. The obtained results show that the isometric contraction of those segments was increased by the factor of two (in the case of internal and 32.6 kHz stimulation) compared to the segments not irradiated with ultrasound. The influence of ultrasound treatment on the contraction force was observed to decrease insignificantly due to the pre-treatment of the segments with diltiazem (an inhibitor of slow calcium channels). When used in a concentration-dependent manner, diltiazem was observed not to modify the relaxation dynamics of the smooth muscle exposed to ultrasound. The use of ultrasound of the above mentioned parameters did not improve the endothelial relaxing properties.

5.3. Experimental Investigation of Tube-Shaped Waveguide Displacement Using Polytec PSV 3D Laser Vibrometer

With the aim to determine the resonance frequency for the maximum displacement toward the z axis, experiments were conducted on the experimental table of the *Polytec PSV 3D* laser vibrometer. The experimental investigation setup is shown in Fig. 71. It consists of the following: 1 is the Polytec PSV 3D laser vibrometer; 2 is the ultrasound waveguide system; 3 is the magnetic holder of the transducer; 4 is the anti-vibration table. To secure the reflection of the laser beam from the tip of the waveguide, the reflection film was glued on the tip. The mass of the

glued reflection film is insignificant, thus it has no implication for the results of the experiment. First of all, the FFT analysis was undertaken to determine the peaks of the system within the respective frequency range (15–30 kHz). Afterwards, the maximum displacement toward the z axis was determined. To determine the displacements when the transducer was excited with operating voltage, the peak was investigated in the time scanning mode.

The experimental investigations were conducted under several sets of different conditions and in different points of interest. As Fig. 71 shows, the waveguide was investigated under free conditions inserted in tube which was filled with water. In both cases, the displacement of the tip of the waveguide was measured. In ANother case, the screw of the housing of the waveguide and the housing of the waveguide (the lug) was investigated to determine the effect of THE housing (the lug) on the displacement of the waveguide.

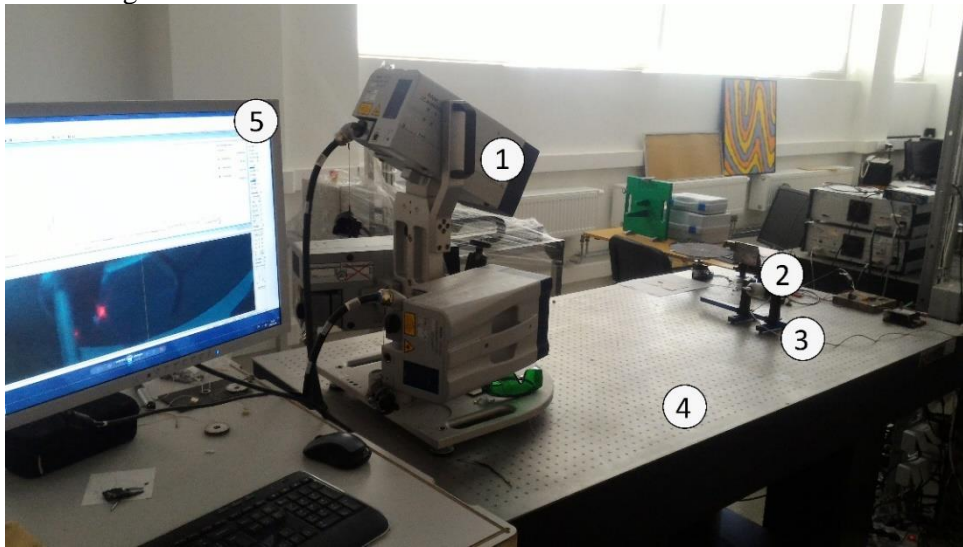


Fig. 71. The experimental setup. 1) A polytec machine (laser sources); 2) a waveguide; 3) a holder; 4) an anti-vibration table, 5) a PC.

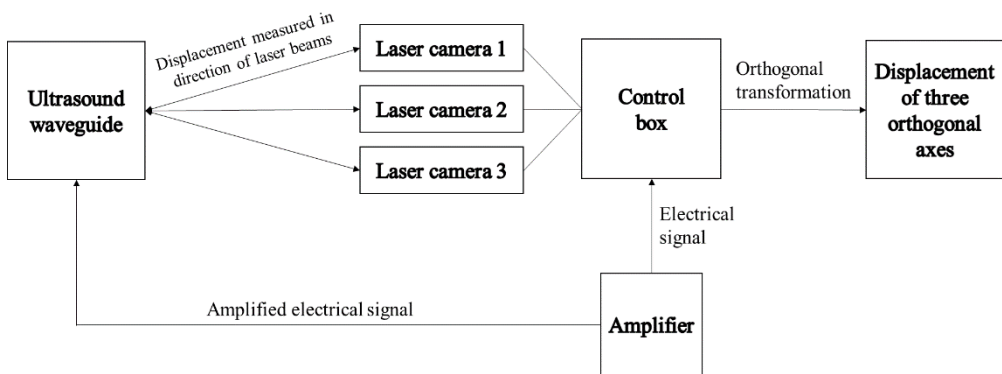


Fig. 72. Polytec PSV 3D laser vibrometer experimental scheme.

Ultrasonic blood vessels cleaning system was excited by a periodic chirp type signal with an amplitude of 10 volts to determine the FFT analysis of the tip of the waveguide.

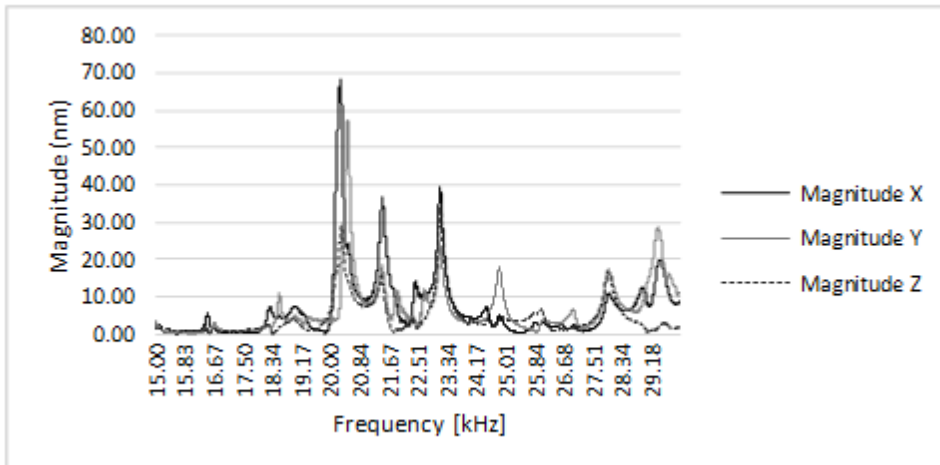


Fig. 73. (FFT analysis of the tip of waveguide in the range of 15–30 kHz) Determining the resonance frequency for the best displacement on the z axis.

Our analysis of the results revealed the following three resonances of the system – at 23.10 kHz, at 20.33 kHz and at 23.04 kHz. The maximum displacements along the z axis were recorded at a frequency of 23.10 kHz (with the error of 0.0815 kHz when compared to the result of modeling when using the Finite Element Method). Since the principal functionality of the ultrasonic system is to trespass the thrombus in the frontal direction (along the z axis), this particular frequency is hereinafter considered to be the operational frequency of the system.

Meanwhile, maximum displacements in the directions of x and y axes (meaning that the operational end of the waveguide is drawing an ellipse of the maximum radius which in turn enables to assume that the cavitation process is the most vigorous at this frequency) were observed at 20.5 kHz. This particular frequency is to be used if the primary task of the operation is not to trespass the thrombus in the frontal direction (the z axis) but rather to clean the walls of the occluded blood vessel.

As our results showed, the maximum displacements along the z axis occur at a resonance frequency of 23.19 kHz with the amplitude of 21 nm.

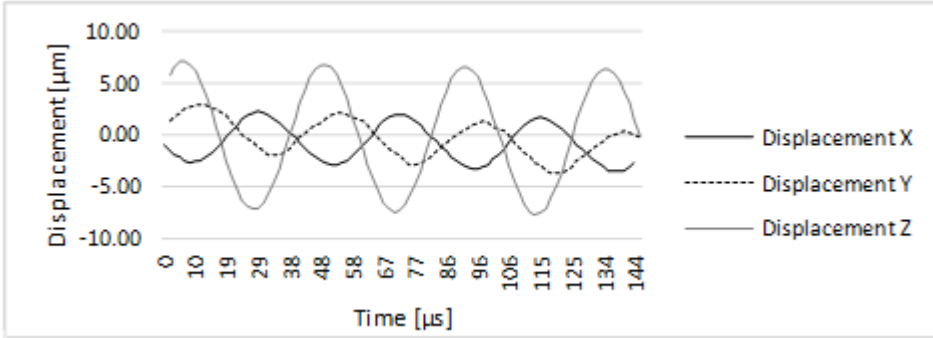


Fig. 74. *x*, *y*, and *z* axis displacement on the resonant frequency at the end point of the waveguide.

When the ultrasonic blood vessel clearing system was induced by the sine type signal with an amplitude of 100 V, the resonance frequency of 23.19 kHz was recorded. The tip of the waveguide under investigation provided maximum displacement towards the *z* axis amounting up to 7.02 micrometer (see Fig. 74).

Our computational mathematical analysis and experimental trials revealed that elliptical movement is characteristic for the tip of the waveguide. It was determined by the imperfections of the steel surface, and the mechanical wave transmission through the threaded connection between the screw connecting the waveguide to a concentrator and a transducer. In comparison to the results of the computational analysis, more significant displacements were observed in the course of the experiment under realistic conditions.

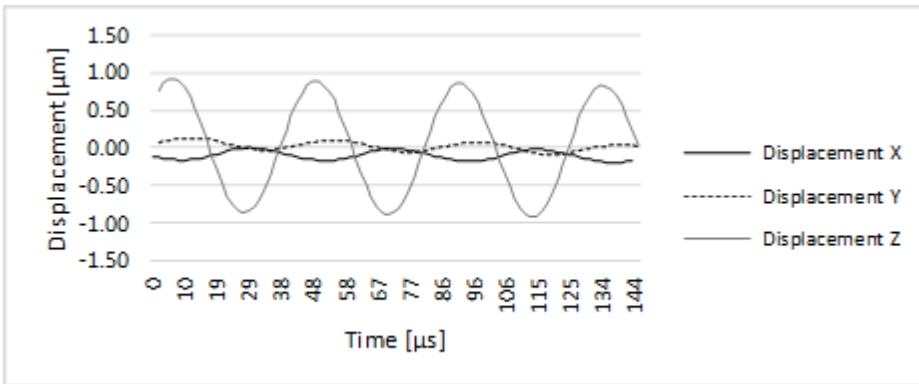


Fig. 75. *x*, *y*, and *z* axis displacement on the resonant frequency at the fixing element (screw) of the ultrasound system.

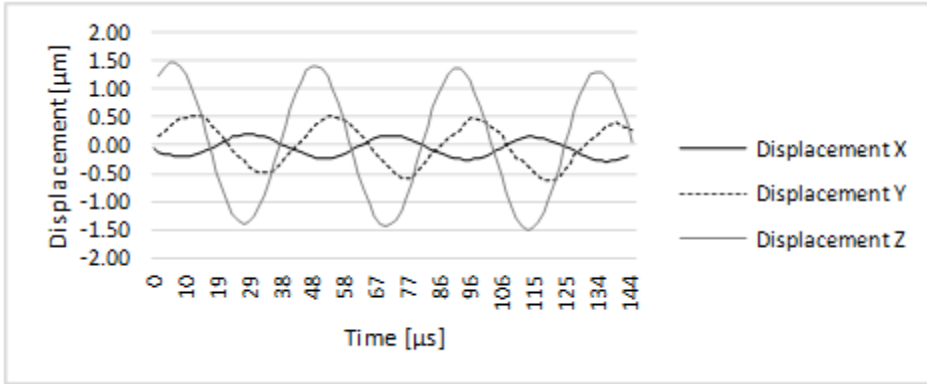


Fig. 76. x, y, and z axis displacement on the resonant frequency at the construction element (lug) of the ultrasound system.

The housing screw and the housing lug were investigated with the aim to determine the influence of these components on the displacements of the waveguide. The same excitation signal as described in the section above was used. The obtained results showed displacements of the screw towards z of 1.4 μm (Fig. 75) and the displacement of the housing end towards the z axis of 1.8 μm (see Fig. 76). Consequently, the housing can be considered to exert influence on the displacements of the tip of the waveguide toward the z axis.

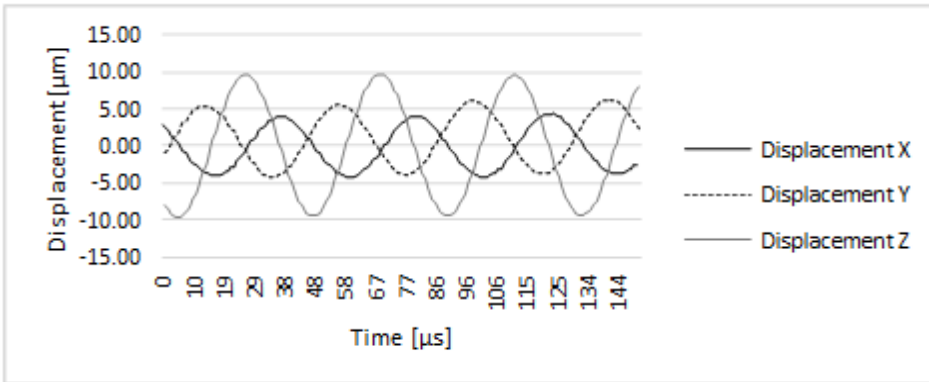


Fig. 77. x, y, and z axis displacement on the resonant frequency at the end point of the waveguide filled with water.

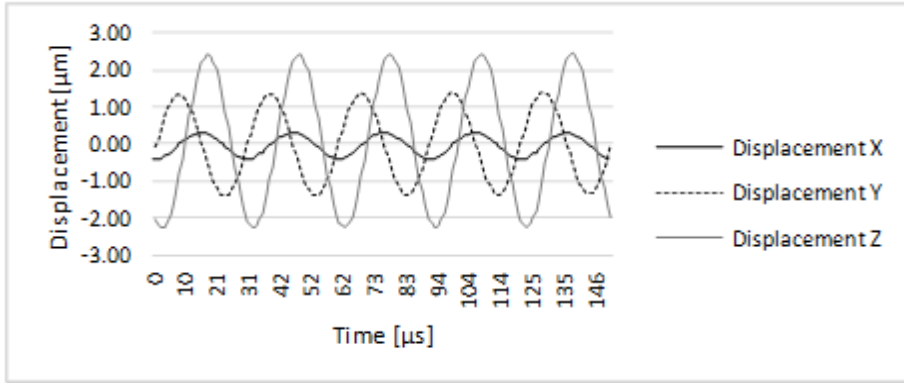


Fig. 78. *x*, *y*, and *z* axis displacement on the resonant frequency at the end point of the waveguide filled with water, placed in a water-filled catheter.

Fig. 77 illustrates the experiment conducted on the waveguide filled with water. In this case, the maximum displacement of $11.02 \mu\text{m}$ was determined. The results obtained through investigation on the waveguide filled with water and placed in a tube which was also filled with water are shown in Fig. 78. In this particular case, the maximum displacement of $2.1 \mu\text{m}$ was recorded; the wave period was observed to get shorter by more than 1.5 times. The investigation also revealed that the waveguide is damped when it is excited under conditions that are very similar to its real operating environment (being surrounded by fluid within the blood vessel). As the experiment delivered positive results, it makes a sound basis for undertaking further investigation, including the computational analysis of a newly designed innovative ultrasound system under realistic operating conditions.

5.4. Amplitude-Frequency Characteristic

To experimentally confirm the modeling accomplished by means of the *Finite Element Method* and the results of non-contact laser system, the amplitude-frequency characteristic was determined. The longitudinal vibration mode in a frequency range of 15–26 kHz was measured. The slowed acoustic signal of the suspended tube-shaped waveguide tip (rested upon the sensor) was measured, or, otherwise, the pressure on the unidirectional sensor (accelerometer) RTF KD 91, with its own resonance frequency of 50 kHz, and sensitivity of $0.5\text{mv}/1\text{m}$ per s^2 was investigated. The experimental platform and the schematic view is presented below in Figures 79 and 80 of this Chapter.

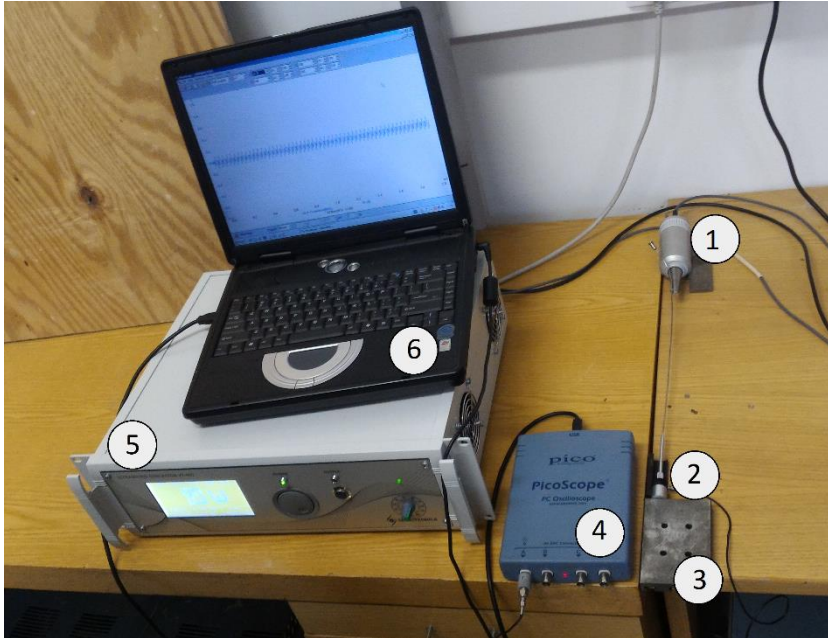


Fig. 79. The experimental setup, where 1) is a transducer; 2) is the Sensor RTF KD91; 3) is a sensor holder; 4) is the Oscilloscope Picoscope 3424; 5) is a generator; 6) is a PC.

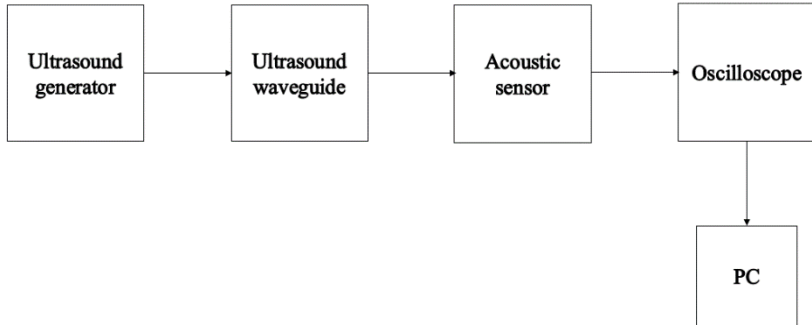


Fig. 80. A scheme of the amplitude-frequency characteristic experiment.

Findings and Results of the Experiment

The amplitude frequency of the waveguide while the generator is working at a different level of power is shown in Figures 81 and 82.

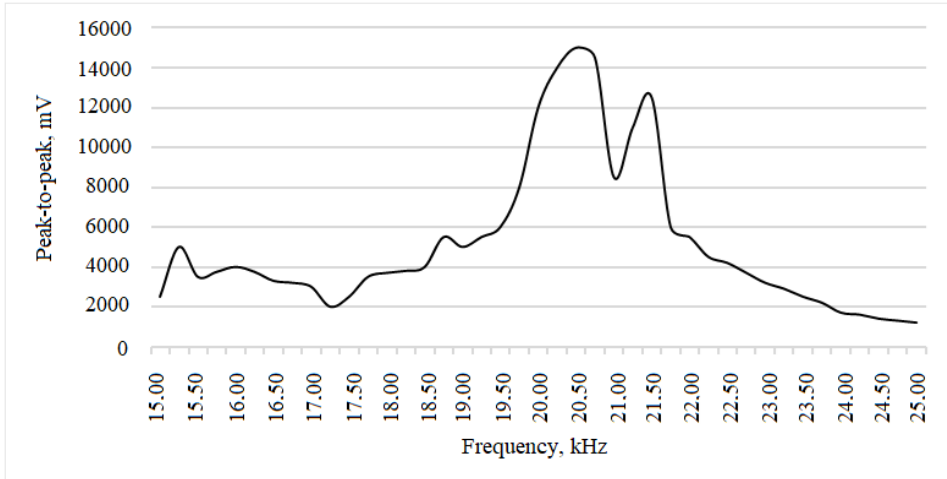


Fig. 81. Amplitude-frequency characteristic for 20% of generator power.

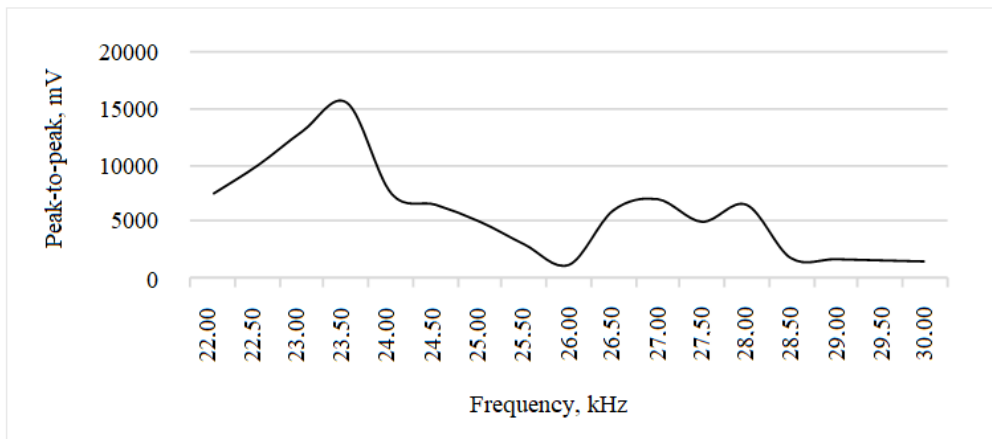


Fig. 82. Amplitude-frequency characteristic for 40% of generator power.

A piezo transducer produces through the waveguide a certain energy boost in a certain range. In this particular case, it is from 19.5 kHz to 22 kHz with the generator operating at 20 % of its power. By providing more power to the system, up to 22 kHz, displacements in the frequency range were so huge that they even caused impact on the acoustic sensor thus making it impossible to record the amplitude-frequency characteristic. However, in the range from 22 kHz to 30 kHz, the operation of the system was excellent and featured the maximum amplitude (in millivolts) at 23.2 kHz. This in principle matches the results obtained through the Finite Element Method with

some error which possibly occurred due to deformations suffered by the waveguide during measurements.

Once the amplitude-frequency characteristic was found, the nodes and antinodes were determined at the maximum quantity (vibration to the sensor). The results of the measurements are presented in Fig. 83.

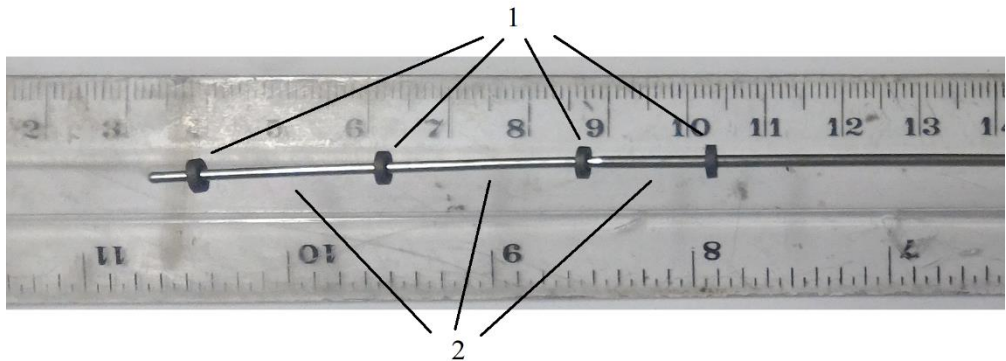


Fig. 83. Nodes and antinodes at 23.185 kHz frequency, where 1) are nodes; 2) are anti-nodes.

In Fig. 83, the standing waves can be seen with the system operating at a resonance frequency of 23.185 kHz. Displacements along the z (frontal) axis cause flexing vibrations to occur that have their own specific nodes and antinodes. At these antinodes, the ceramic rings (distinguished by the generation of extremely low friction when in contact with any other surfaces) tend to obtain the steady state. The variation in frequency makes them change the position. In general, they are positioned at steps of 20 mm.

The experiment showed three contact points to exist. This serves as a suitable visual aid to show how many active contact areas there are that absorb energy due to their friction.

5.5. Experimental Investigation of Waveguide Wire Influence to Surrounding Fluids

The results described/presented in this chapter have been published in the following article: Kargaudas, V., Bubulis, A., Navickas, J., Vitkus, L., Venslauskas, M. Theoretical and Experimental Investigation of Tube-Shaped Waveguide Wire. *Journal of Measurements in Engineering* 5, 2017, 257–265.

5.5.1. Mechanical and Thermal Influence on Blood

During the operation of the device under research, the cavitation process and the friction between the waveguide and the surrounding fluids cause temperature to rise dramatically. Human body temperature above 42 °C is well known to cause fatality as red blood cells undergo *in vivo* hemolysis [99]. Taking this into

consideration, the next series of experiments on human blood were undertaken. For this purpose, *Thermovisor FLIR SC7000*, a generic generator, a PC and the tube-shaped waveguide system was used. Fig. 84 shows the setup and a schematic view of the experiment accomplished.

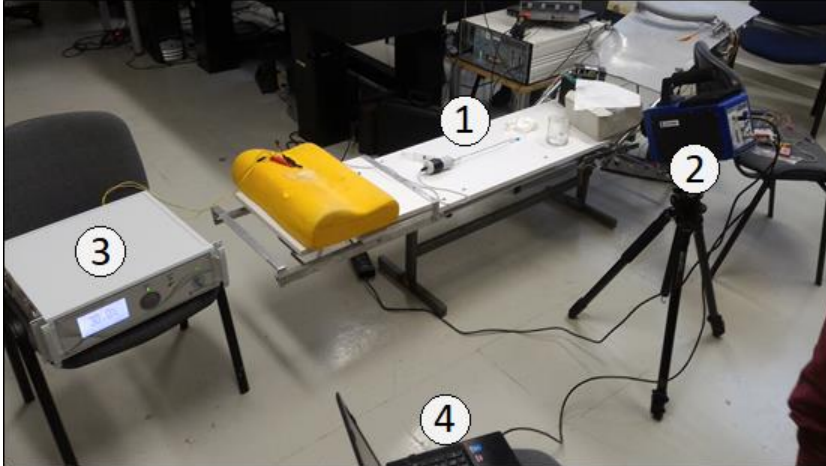


Fig. 84. The experimental setup where 1) is the waveguide in a tube filled with water; 2) is the Thermovisor FLIR SC7000; 3) is a generator; 4) is a PC.

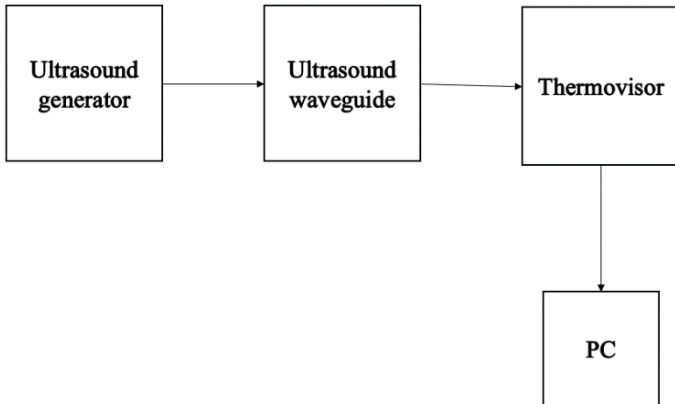


Fig. 85. A schematic view of the experiment.

The first experiment was carried out while using the operating system inside the tube with the diameter of 3 mm, which in its structure was very similar to a human artery. The data gathered in the course of the experiment revealed that it takes as little as 4 seconds to reach the lethal temperature of 42 °C (with the starting point being 36 °C).

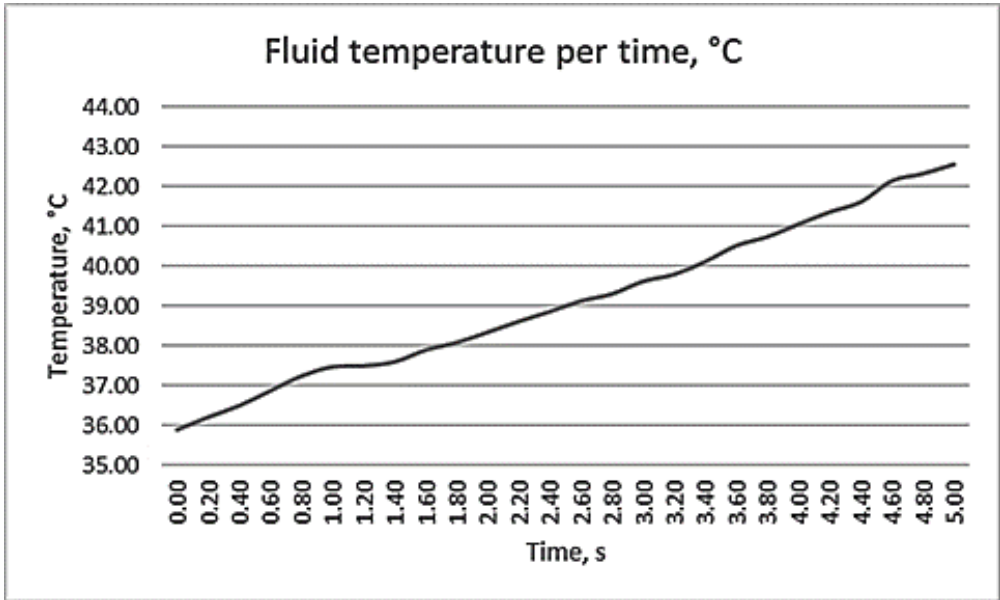


Fig. 86. Fluid temperature per time, °C.

As the next step, a series of figures presented below indicates what happens to the red blood cells (erythrocytes) after exposing blood to ultrasound for 30 s. The same experiment setup as described in Figs. 84 and 85 was used.

After blood had been affected with ultrasound, blood samples were gathered, and a thin 1-cell layer was spread on a transparent glass plate and checked with an electronic microscope. The pictures obtained with a microscope can be seen in Fig. 87, Fig. 88 and Fig. 89.

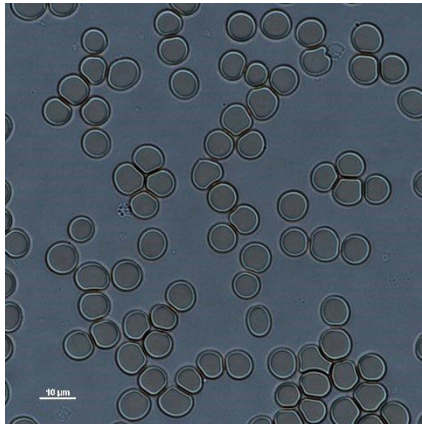


Fig. 87. A microscopic photo of erythrocytes exposed to ultrasound, the control group.

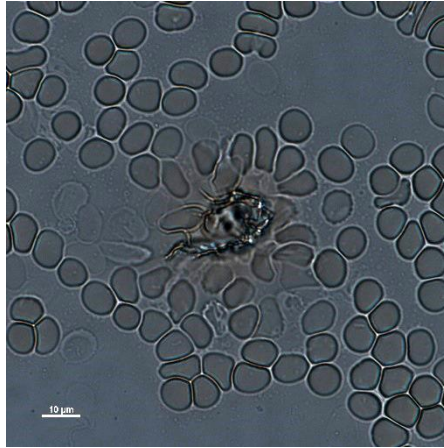


Fig. 88. A microscopic photo of erythrocytes exposed to ultrasound after 15 s of influence of the cavitation.

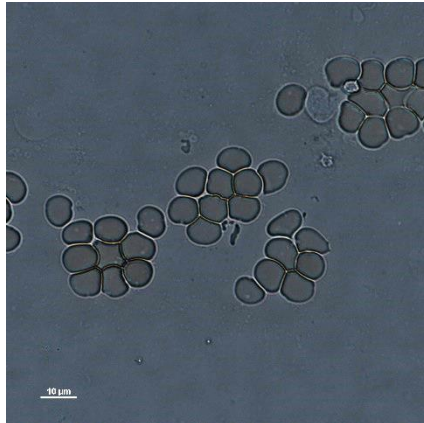


Fig. 89. A microscopic photo of erythrocytes exposed to ultrasound after 30 s of influence of the cavitation.

The microscopic pictures of human blood taken after exposing blood to ultrasound generated by the ultrasonic system with a tube-shaped waveguide revealed that, after 15 seconds of treatment, blood clots have been formed, and, after 30 seconds of treatment, some cells have totally been destroyed. Consequently, it is vital to find and establish the safe operating regime for the ultrasonic vascular clearing system of the innovative design offered here. Bearing all the above in mind, the experiments described above in Chapter 4.4.2 were undertaken.

5.5.2. Determination of the Safe Operating Regime for the Ultrasound System

The second experiment (within the same experimental setup as described in Chapter 4.4.1) was carried out with the aim to determine the safe (as the human body temperature above 42 °C is well known to cause fatality as red blood cells undergo *in vivo* hemolysis [99]) operating regime of the ultrasonic system under research. Figures 90 and 91 show the results of the experiment.

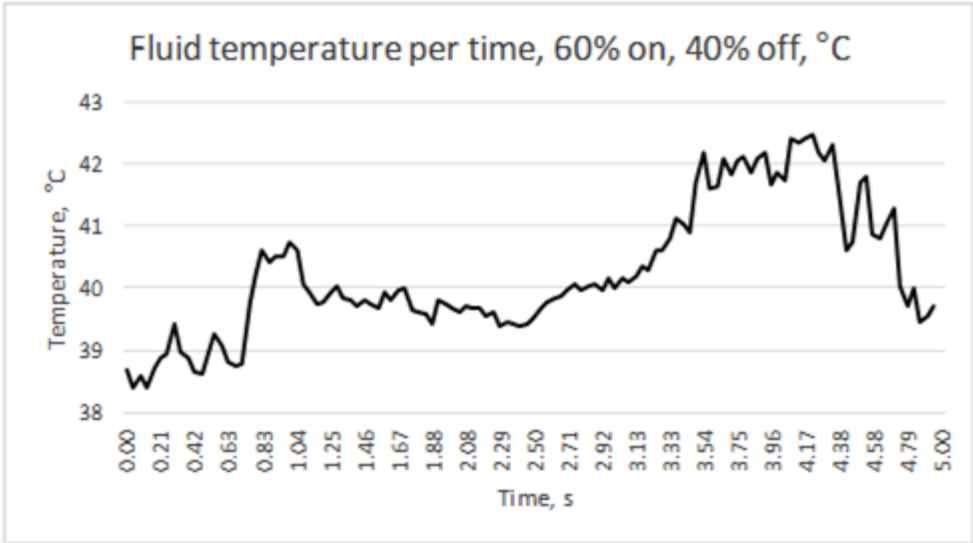


Fig. 90. The temperature inside a tube when operating under pulsed regime with 60 % on, 40 % off.

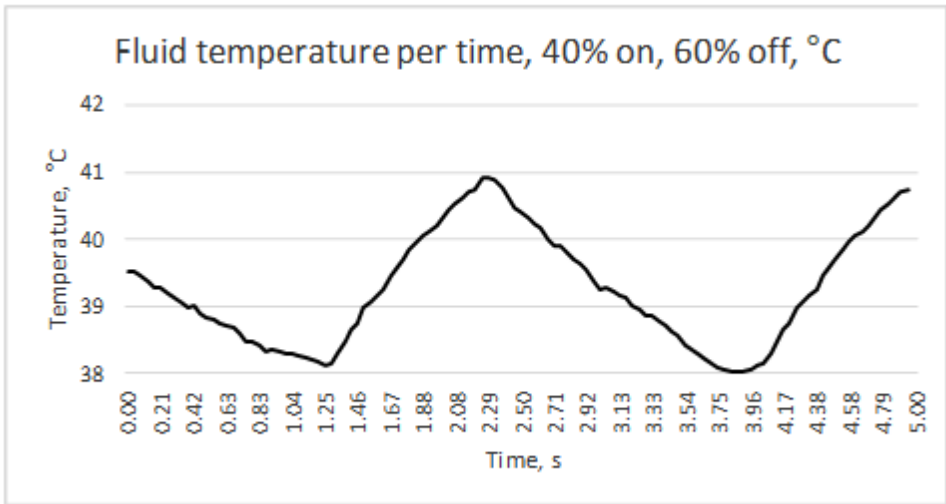


Fig. 97. The temperature inside a tube when operating under pulsed regime with 40 % on, 60 % off.

It was experimentally found that the safe operating regime, i.e., one which enables to avoid heating of the environment to the temperature harmful for the medium (blood) and the surrounding tissues, is achieved when the system is 40 % on, and 60 % off over the period of 1 second.

5.6. Impedance Analysis of the Waveguide in Different Working Regimes

Electrical impedance represents an electric method of finding the resonance frequency. Since the piezo ring is the electric condenser, measuring the impedance (reactance) allows finding the resonance frequencies of the system. Our measurements used the impedance analyzer *Wayne Kerr 6500b*. Its main parameters are presented in the table below.

Table 3. Technical specifications of the impedance analyzer *Wayne Kerr 6500b*

Frequency range, Hz	20 Hz to 20 mHz
Accuracy of set frequency, %	0.005%
Measurements per second	20

The experimental platform was comprised of the following two components: the transducer and the waveguide attached to it together with the impedance analyzer *Wayne Kerr 6500b* that provided the power supply to the transducer.

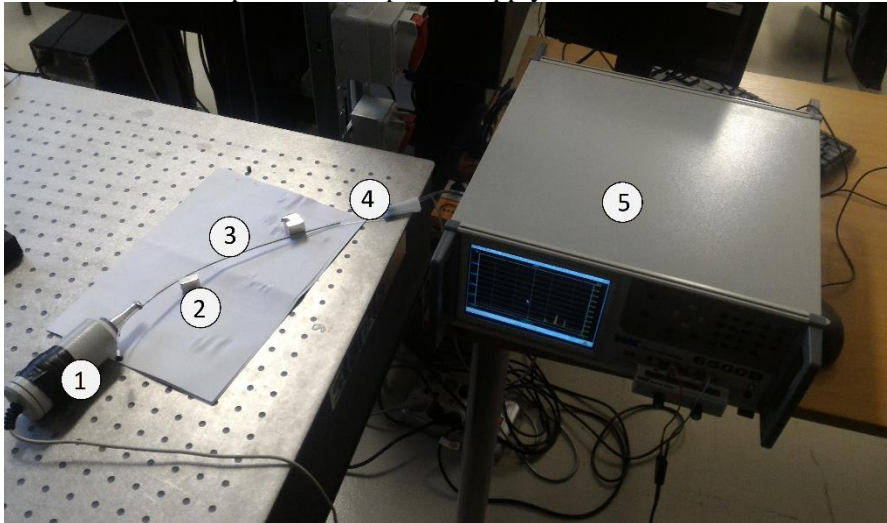


Fig. 92. The experimental setup, where 1) is the transducer; 2) are magnet holders; 3) is a tube-shaped waveguide; 4) is a plastic tube filled with water; 5) is the *Wayne Kerr 6500b* unit.

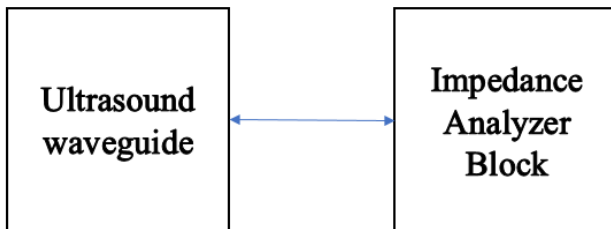


Fig. 93. A schematic view of the experiment.

In the following Figures 94–99, the dotted line shows the impedance resistance while the solid line shows the phase.

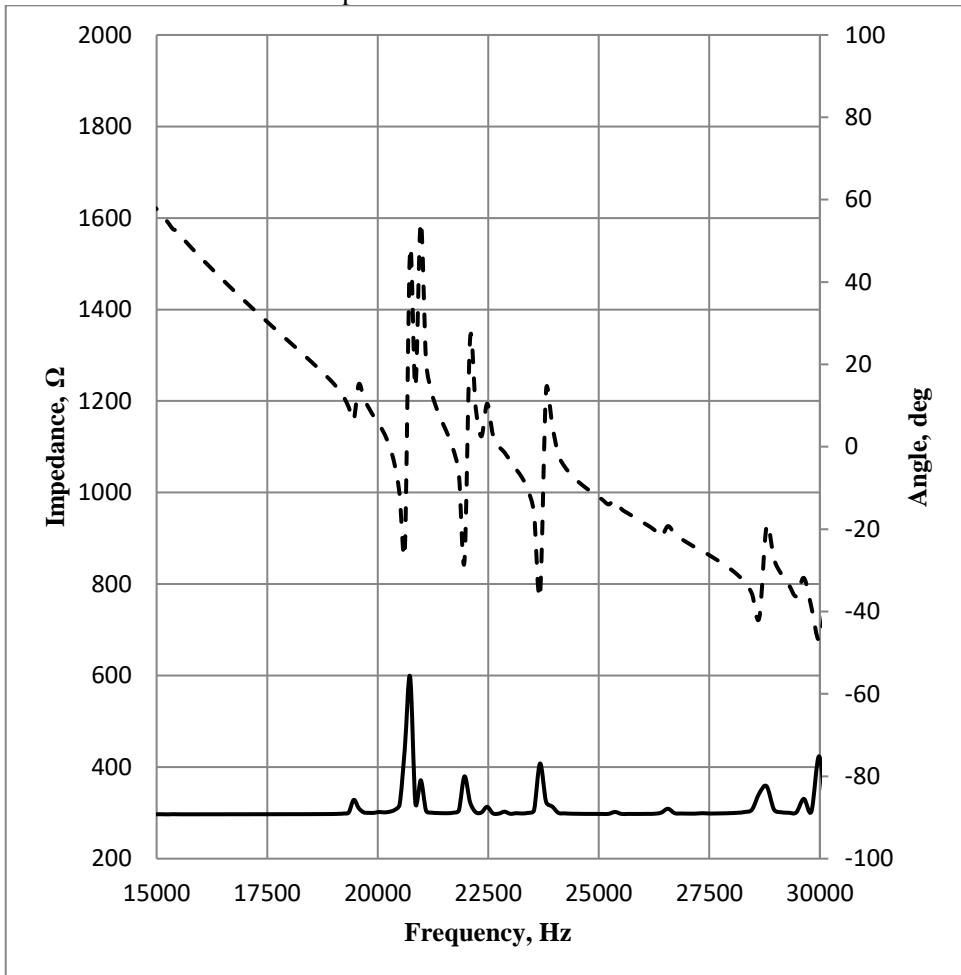


Fig. 94. Impedance analysis of the ultrasound system with a free waveguide in the air.

Our impedance analysis showed three main resonance modes – at ~ 20.852 kHz, 22.085 kHz and 23.807 kHz. These findings prove and (with a small deviation) confirm the results gathered during the experiment described in Chapter 4.3. The following figures show the results of the experiment that was carried out while using the waveguide in different positions: a) inserted in a tube filled with water b) bent c) clamped d) variations in between the first 3 positions.

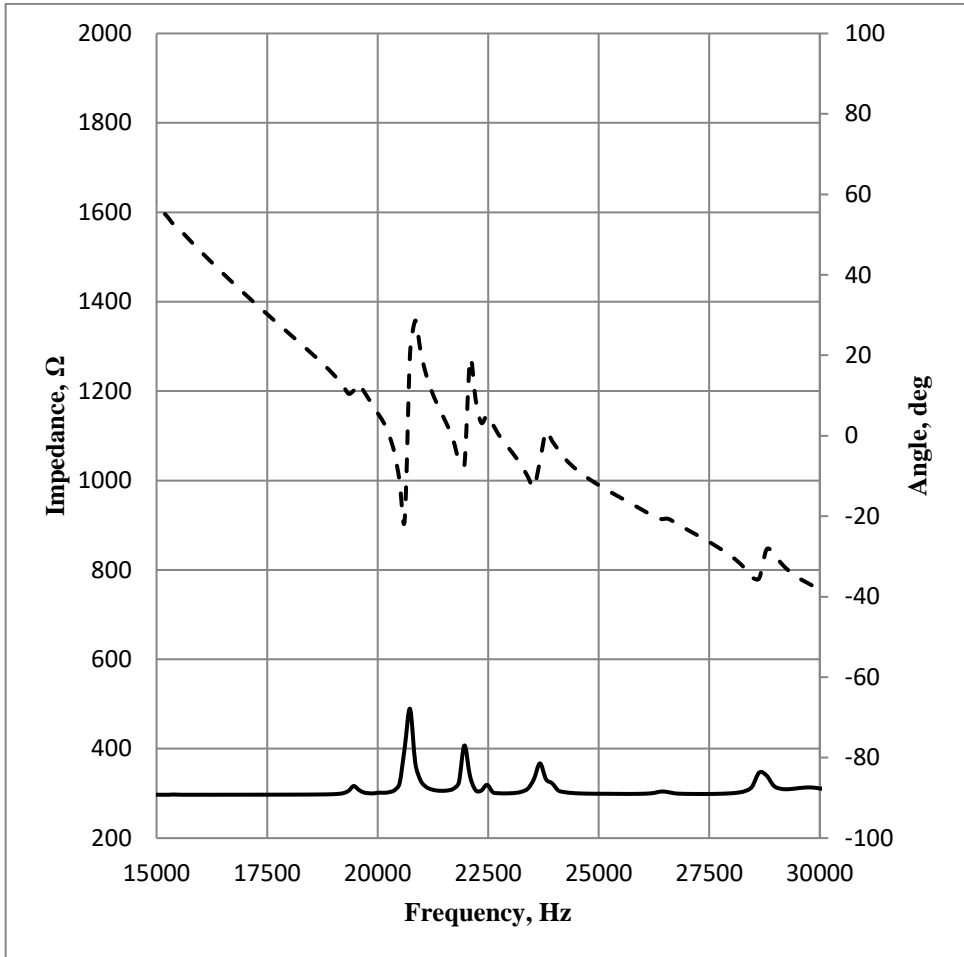


Fig. 95. Impedance analysis of the ultrasound system with a clamped-tip waveguide in the air.

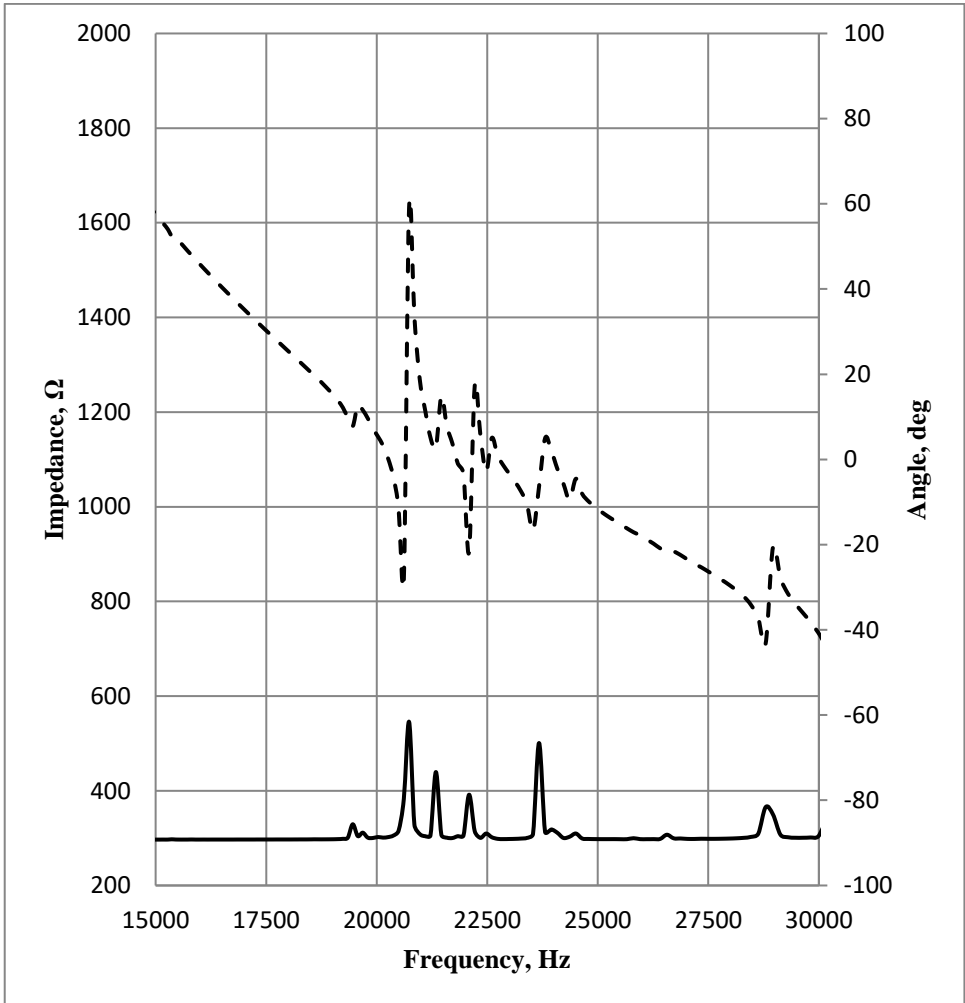


Fig. 96. Impedance analysis of the ultrasound system with a bent waveguide in the air.

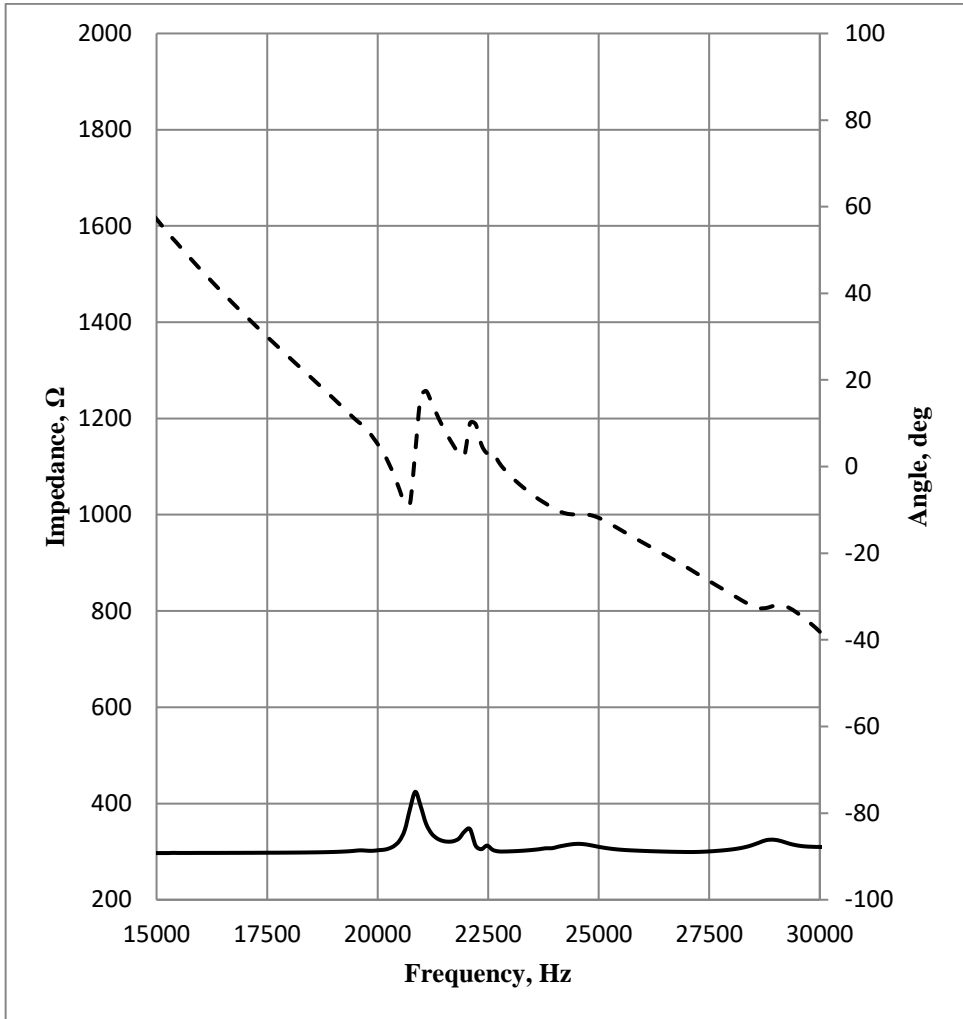


Fig. 97. Impedance analysis of the ultrasound system while the waveguide is placed in a tube filled with water.

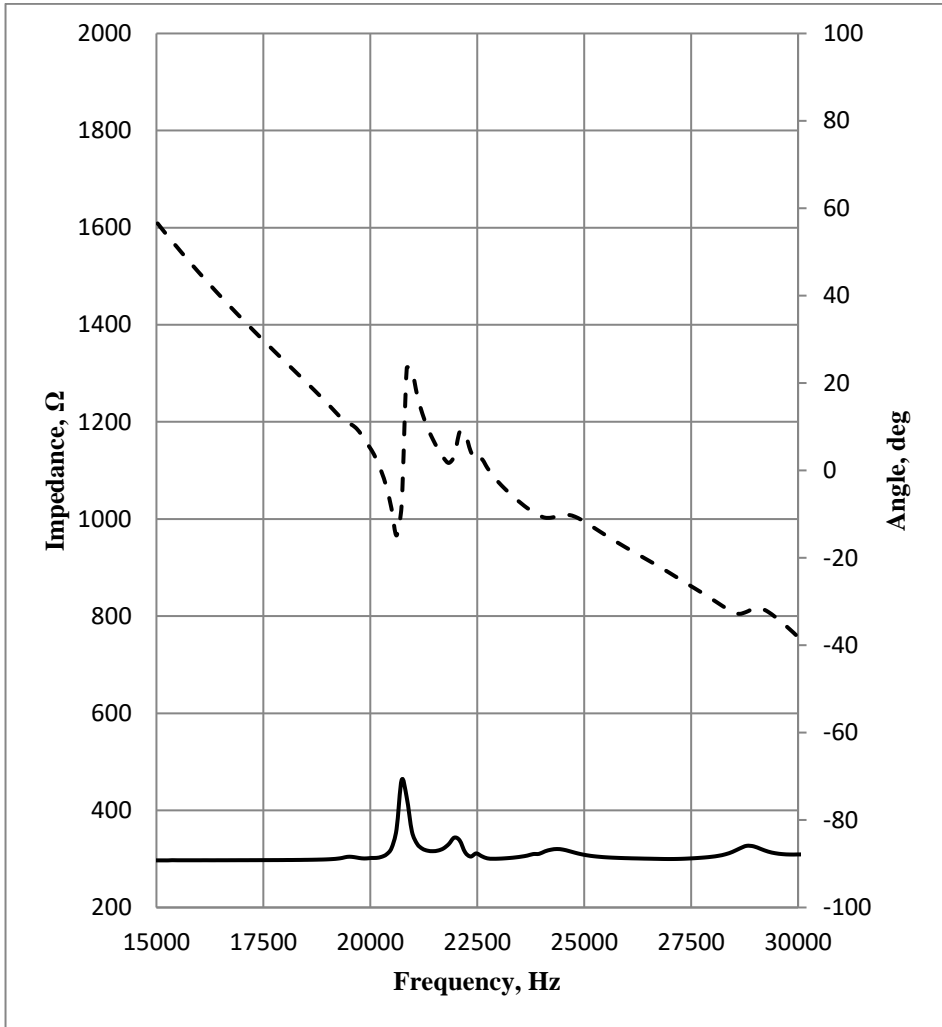


Fig. 98. Impedance analysis of the ultrasound system while the bent waveguide is placed in a tube filled with water.

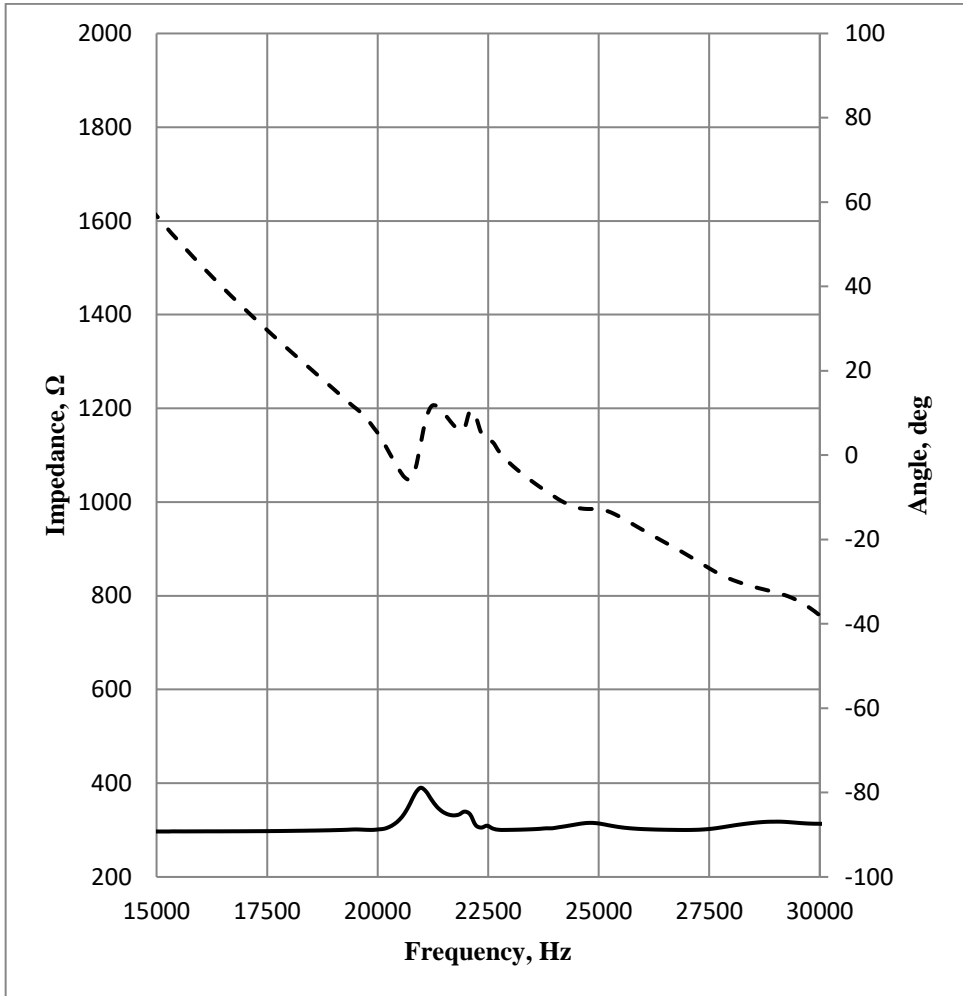


Fig. 99. Impedance analysis of the ultrasound system while the bent waveguide with a clamped tip is placed in a tube filled with water.

Our analysis showed an obvious decrease in impedance under conditions when the waveguide is less likely to vibrate, i.e., when the waveguide under research is bent, clamped at its tip, inserted in the tube filled with water, etc.

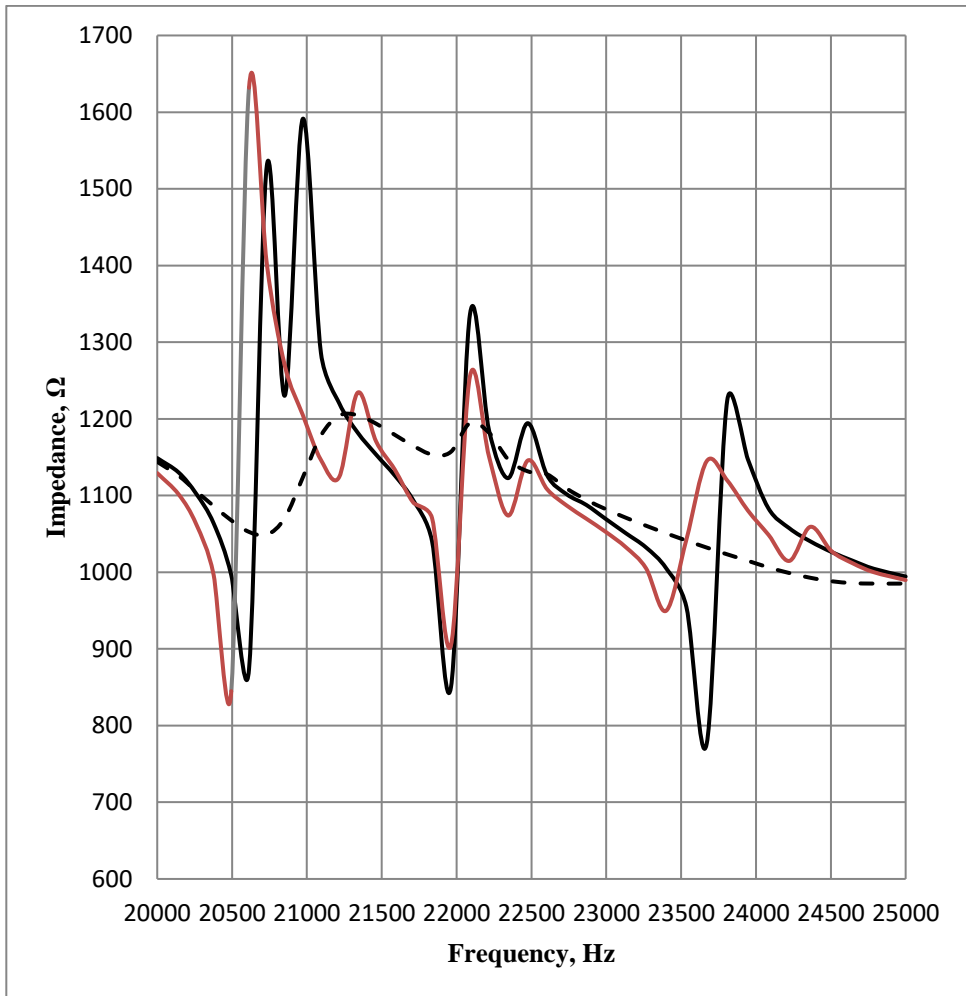


Fig. 100. Impedance analysis of the ultrasound system while the waveguide with a waveguide is in different positions: 1) the black continuous line – empty and free; 2) the grey line – bent; 3) bent, placed into a tube filled with water and clamped.

Fig. 100 indicates differences among the experimentally measured impedances with the waveguide placed in different positions. For instance, when the bent waveguide is tested, the first resonance mode is observed to be shifted by approx. 0.4 kHz (i.e., the required frequency is decreased). Meanwhile, the experimentally determined resonance frequency of 23.185 kHz when suppressing the waveguide under three different regimes (i.e., bent, immersed in water and with its tip being immobilised) does not result in desirable displacements anymore. It means that, in this particular case, the drop in impedance requires for the frequency to be changed, i.e., the frequency of 21.25 kHz must be used instead as it had featured positive results. In general, this particular experiment led to the following observations:

1. The position of the waveguide inserted in the blood vessel can be, in principle, determined on the grounds of impedance while comparing the actually operating waveguide to the experimentally taken measurements of the bent and immobilized waveguide. The lower is the impedance (in ohms), the greater is the obstacle the waveguide is confronting. In the resonance mode, the totally diminished impedance indicates that the tip of the waveguide has confronted some hard object, such as plaque lamella.
2. Certain positions of the waveguide (such as clamped at the tip, curved, etc.) cause the resonance frequency of the waveguide to vary. Observation of the impedance during the operation enables to work under the resonance regime at all times without the need to listen to the operation of the waveguide by using some external sensor or without using an X-ray, which in turn makes the operation safer and more patient-friendly.

5.7. Summary of Chapter 4

The results obtained through the Finite Element Method regarding displacements of each individual component of the waveguide – the tip of the tube, the lug and the screw – at the moment of operation, were proved experimentally in the thesis. The maximum displacement along the frontal z axis ($7.02 \mu\text{m}$) was found to occur at an operational frequency of 23.185 kHz.

When testing the ultrasonic system in the natural operational medium, namely, human blood, the critical temperature of 42 degrees at the tip of the waveguide was achieved in less than 3 s with the waveguide being vibrated in a continuous mode. For this reason, it is absolutely necessary to ensure the pulsed operating regime, i.e., the one that enables to avoid heating of the environment (blood) and the surrounding tissues up to the harmful temperature. It was experimentally found that such an operating regime is achieved when the system is 40 % on, and 60 % off over the period of 1 second.

The investigation of the ultrasonic system in several different positions (for instance, with the clamped tip in the air, in a tube filled with water, etc.) allowed finding changes in impedance resistance depending on the position of the tube. Although a higher number of similar experiments are required to be carried out while using more sensitive equipment, this is nevertheless a highly viable and promising data as the technique proposed herein allows for ‘anticipating’ if the waveguide is reclined against an occlusive malformation, if it is bent over while in the human artery, etc., which reduces the need for using harmful X-rays and the infusion of certain reagents into the human body.

CONCLUSIONS

1. Currently, cardiovascular diseases represent the leading cause of death and disability among humans before their age of 65 years. Moreover, the *World Health Organization* predicts a further growth of cardiovascular morbidity. For this reason, the comprehensive review of the relevant literature and patient information was undertaken. As a result, it revealed an obvious need for the development of an invasive ultrasonic waveguide enabling to trespass the thrombus while operating at both frontal and radial directions, allowing to feed and deliver any required amount of drugs to the damaged site of the blood vessel, and at the same time enabling to suck away the scurf of the broken occluding malformations.
2. The tube-shaped waveguide of the innovative design with the length of 260 mm and thickness of 1.5 mm has been developed with the holes drilled at its operational tip through which an unlimited amount of drugs can be fed to the site of the waveguide operation. The FEM modeling of the simplified waveguide acting in close to real-life conditions (in a muscle-surrounded blood vessel filled with blood) showed that the best frequency for the greatest amount of frontal and transverse pressure is 24.970 kHz. While working in such a resonant mode, the best waveguide tip point displacement towards the z axis (forward) is 8.3 μm .
3. The mathematical modeling of the waveguide allowed to observe and explore the phenomenon of the caverns, i.e., in the course of cavitation at the end of the waveguide, the pocket containing tenuous gas is formed that lags behind the pocket containing tenuous gas and which formed at the tip of the waveguide moving in circles at a certain angle in theta degrees. Further calculations enabled us to obtain the width of such a cavern which was equal to 2.3 μm .
4. The ultrasound effect on live human blood vessels was explored experimentally. A 2.4 times better response to contraction-inducing substances was observed in the case when a blood vessel was pre-treated with ultrasound. Measurements of the vibrations taken by a laser non-contact measurement system at different parts of the ultrasonic system under research proved the results of computational modeling using FEM to be true. The maximum displacement at the frontal z axis under a resonance frequency of 23.815 kHz was found to amount up to 7.9 μm . The safe operating regime for the tube-shaped waveguide was established experimentally. Blood was found not to heat above the destructive temperature of 42 degrees Celsius at the site of the waveguide operation (at its tip) when the ultrasound generator was operated in a pulsed mode, i.e., 40 % on, and 60 % off over its period of activity.

REFERENCES

1. NICHOLS, M., TOWNSEND, N., SCARBOROUGH, P., RAYNER, M. (2014). Cardiovascular Disease in Europe 2014: Epidemiological Update. In: *European Heart Journal*. 2014, 35(42), 2950–2959. ISSN 1522-9645.
2. TOWNSEND, N., NICHOLS, M., SCARBOROUGH, P., RAYNER, M. (2015). Cardiovascular Disease in Europe – Epidemiological Update 2015. In: *European Heart Journal*. 2015, 36(40), 2696–2705. ISSN 1522-9645.
3. GLOBAL HEALTH OBSERVATORY (GHO). (2017). *Raised Blood Pressure Data* [interactive]. [Accessed online August 10, 2017]. Via http://www.who.int/gho/ncd/risk_factors/blood_pressure_prevalence_text/en/
4. EUROSTAT. (2014a). *Tobacco Consumption Statistics* [interactive]. 2014. [Accessed online August 10, 2017]. Via http://ec.europa.eu/eurostat/statistics-explained/index.php/Tobacco_consumption_statistics
5. EUROSTAT. (2014b). *Overweight and Obesity – BMI Statistics* [interactive]. [Accessed online August 10, 2017]. Via http://ec.europa.eu/eurostat/statistics-explained/index.php/Overweight_and_obesity_-_BMI_statistics
6. EUROSTAT. (2014c). *Major and Chronic Diseases* [interactive]. [Accessed online August 10, 2017]. Via https://ec.europa.eu/health/major_chronic_diseases/diseases/diabetes_en
7. CENTERS FOR DISEASE CONTROL AND PREVENTION (CDC). (2016). *Diabetes Statistics and Forecast* [interactive]. [accessed online July 28, 2017]. Via <https://www.cdc.gov/diabetes/statistics/lea/fig3.htm>
8. ROBBINS, J.M., STRAUSS, G., ARON, D., LONG, J., KUBA, J., KAPLAN, Y. (2008). Mortality Rates and Diabetic Foot Ulcers. In: *Journal of the American Podiatric Medical Association*. 2008 November 1, 2008, 98(6), 489–493.
9. BLESSY, T., SUMAN, K.S. (2016). Blood Flow in Human Arterial System – a Review. In: *International Conference on Emerging Trends in Engineering, Science and Technology*. 24, 2016, 339–346.
10. HOSKINS, P.R., LAWford, P.V., DOYLE, B.J. (2017). *Cardiovascular Biomechanics*. 2017, 25–35, ISBN 978-3-319-46405-3.
11. MALANGA C.J. (2007). Coronary Circulation. In: *xPharm: The Comprehensive Pharmacology Reference*. New York: Elsevier. 2007, 1–3, ISBN 9780080552323.
12. KOSTA, S., NEGRONI, J., LASCANO, E., DAUBY, P.C. (2017). Multiscale Model of the Human Cardiovascular System: Description of Heart Failure and Comparison of Contractility Indices. In: *Mathematical Biosciences*. 284, 2017, 71–79.
13. WATS, S.W. (2007). Intrinsic Regulation of the Vasculature. In: *xPharm: The Comprehensive Pharmacology Reference*. New York: Elsevier. 2007, 1–5, ISBN 9780080552323.
14. CUENOD, C.A., BALVAY, D. (2013). Perfusion and Vascular Permeability: Basic Concepts and Measurement in DCE-CT and DCE-MRI. In: *Diagnostic and Interventional Imaging*. 94, 2013, 1187–1204.
15. HAMMOND, H.K. (2014). Exercise and the Cardiovascular System. In: *Reference Module in Biomedical Sciences*. Elsevier. ISBN 9780128012383.
16. MADANI, M.M., GOLTS, E. (2014). Cardiovascular Anatomy. In: *Reference Module in Biomedical Sciences*. Elsevier. ISBN 9780128012383.
17. HOIT, B.D. (2014). Normal Cardiac Physiology and Ventricular Function. In: *Reference Module in Biomedical Sciences*. Elsevier. ISBN 9780128012383.

18. WATTS, S.W. (2007). Regulation of the Vasculature. In: *xPharm: The Comprehensive Pharmacology Reference*. New York: Elsevier. 2007, p.1, ISBN 9780080552323.
19. KANAGY, N.L., WATTS, S.W. (2007). Vascular Smooth Muscle Contraction. In: *xPharm: The Comprehensive Pharmacology Reference*. New York: Elsevier. 2007, 1–5, ISBN 9780080552323.
20. LI, H., HORKE, S., FÖRSTERMANN, U. (2014). Vascular Oxidative Stress, Nitric Oxide and Atherosclerosis. In: *Atherosclerosis*. 2014, 237(1), 208–219.
21. ALEXOPOULOS, N., KATRITSIS, D., RAGGI, P. (2014). Visceral Adipose Tissue as a Source of Inflammation and Promoter of Atherosclerosis. In: *Atherosclerosis*. 2014, 233(1), 104–112.
22. YERRAMASU, A., DEY, D., VENURAJU, S., *et al.* (2014). Increased Volume of Epicardial Fat Is an Independent Risk Factor for Accelerated Progression of Sub-Clinical Coronary Atherosclerosis. In: *Atherosclerosis*. 2014, 220(1), 223–230.
23. TZIRTZILAKIS, E.E. (2015). Biomagnetic Fluid Flow in an Aneurysm Using Ferrohydrodynamics Principles. In: *Physics of Fluids*. 2015, 27(6), 061902.
24. COLLINS, R., SCRIMGEOUR, A., YUSUF, S., PETO, R. (1998). Reduction in Fatal Pulmonary Embolism and Venous Thrombosis by Perioperative Administration of Subcutaneous Heparin. In: *New England Journal of Medicine*. 1998, 318(18), 1162–1173.
25. VON BRÜHL, M. L., STARK, K., STEINHART, A., CHANDRARATNE, S., KONRAD, I., LORENZ, M., BYRNE, R.A. *et al.* (2012). Monocytes, Neutrophils, and Platelets Cooperate to Initiate and Propagate Venous Thrombosis in Mice *in Vivo*. In: *The Journal of Experimental Medicine*. 2012, 209(4), 819–835.
26. ABDULLAH, B.J.J., MOHAMMAD, N., SANGKAR, J.V., AZIZ, Y.A., GAN, G.G., GOH, K.Y., BENEDICT, I. (2014). Incidence of Upper Limb Venous Thrombosis Associated with Peripherally Inserted Central Catheters (PICC). In: *The British Journal of Radiology*. 2014, 78(931), 596–600.
27. THOMPSON, A.E. (2015). Deep Vein Thrombosis. In: *JAMA*. 2015, 313(20), 2090.
28. YAMAGAMI, T., KATO, T., IIDA, S., TANAKA, O., NISHIMURA, T. (2014). Retrievable Vena Cava Filter Placement during Treatment for Deep Venous Thrombosis. In: *The British Journal of Radiology*. 2014, 76 (910), 712–718.
29. GOLDBERGER, S.Z., BOUNAMEAUX, H. (2012). Pulmonary Embolism and Deep Vein Thrombosis. In: *The Lancet*. 2012, 379(9828), 1835–1846.
30. MENDOZA, E., LATTIMER, C. R. (2014). Superficial Vein Thrombosis. In: *Duplex Ultrasound of Superficial Leg Veins*. 2014, 217–225.
31. ZUILY, S., REGNAULT, V., GUILLEMIN, F., KAMINSKY, P., RAT, A.C., LECOMPTE, T., WAHL, D. (2013). Superficial Vein Thrombosis, Thrombin Generation and Activated Protein C Resistance as Predictors of Thromboembolic Events in Lupus and Antiphospholipid Patients. A Prospective Cohort Study. In: *Thrombosis Research*. 2013, 132(1), 1–7.
32. URBONAVICIUS, S., URBONAVICIENE, G., CICENAS, J., HOEGH, A., SANDERMANN, J., VALIUS, M. (2016). A Novel View to the Pathogenesis of Varicose Veins: What Proteins Are Talking? In: *Journal of Vascular Surgery: Venous and Lymphatic Disorders*. 2016, 4(1), 145.
33. SCHLÖGEL, M.J., BROUILLARD, P., BOON, L.M., & VIKKULA, M. (2015). Genetic Causes of Lymphedema. In: *Lymphedema*, 2015, 19–31.
34. VAN VELTHOVEN, M.E., BAARSMA, S., VAN HAGEN, P.M., VAN LAAR, J.A., MISSOTTEN, T. (2014). The Value of Rescreening in Primary Retinal Vasculitis. In: *Investigative Ophthalmology & Visual Science*. 2014, 55(13), 5793–5793.

35. FLAVAHAN, N.A. (2015). Pathophysiological Regulation of the Cutaneous Vascular System in Raynaud's Phenomenon. In: *Raynaud's Phenomenon*. 2015, 57–79.
36. BUTROS, S.R., LIU, R., OLIVEIRA, G.R., GANGULI, S., & KALVA, S. (2013). Venous Compression Syndromes: Clinical Features, Imaging Findings and Management. In: *The British Journal of Radiology*. 2013, 86(1030), 20130284.
37. RIERA, E., ACOSTA, V.M., BON, J. *et al.* (2016). Airborne Power Ultrasonic Technologies for Intensification of Food and Environmental Processes. In: *Physics Procedia*. Vol. 87, 2016, 54–60.
38. TIRIVAVIRI, A.M., IYUKE, E.S., PATERSON, E.A. (2018). Energy Changes during Use of High-Power Ultrasound on Food Grade Surfaces. In: *South African Journal of Chemical Engineering*. 2018, 62–73.
39. O'BRIEN, W.D. (2007). Ultrasound-Biophysics Mechanisms. In: *Progress in Biophysics and Molecular Biology*. 2007, 93, 212–255.
40. RYBYANETS, A.N., NAUMENKO, A.A., SAPOZHNIKOV, O.A., KHOKHLOVA, V.A. (2015). New Methods and Transducer Designs for Ultrasonic Diagnostics and Therapy. In: *2015 International Congress on Ultrasonics, 2015 ICU Metz, Physics Procedia 70*. 2015, 1152–1156.
41. VYAS, N., DEGHANI, H., SAMMONS, R.L., WANG, Q.X., LEPPINEN, D.M., WALMSLEY, A.D. (2017). Imaging and Analysis of Individual Cavitation Microbubbles around Dental Ultrasonic Scalers. In: *Ultrasonics*. 81, 2017, 66–72.
42. ABRAMOWICZ, J.S. (2017). How to Keep Ultrasound Safe in Obstetrics? What have We Learned? In: *Ultrasound in Medicine & Biology*. 43, 2017, 130–131.
43. ZHANG, N., CHOW, S.K., LEUNG, K.S., CHEUNG, W.H. (2017). Ultrasound as a Stimulus for Musculoskeletal Disorders. In: *Journal of Orthopaedic Translation*. 9, 2017, 52–59.
44. SILBERSTEIN, J., LAKIN, C.M., PARSONS, J.K. (2008). Shock Wave Lithotripsy and Renal Hemorrhage. In: *Rev Urol*. 2008, 10, 236–241.
45. VOTAVOVA, R., LINHARTOVA, A., KORINEK, J., MAREK, J., LINHART, A. (2015). Echocardiography in Coronary Artery Disease. In: *Cor et Vasa*. 57, 2015, 408–418.
46. LANDMESSER, U., HORNIG, B., DREXLER, H. (2004). Endothelial Function. A Critical Determinant in Atherosclerosis? In: *Circulation*. 2004, 109, Suppl II, 27–33.
47. HUYGENS, C. (1672). Extrait d'une lettre de M. Hugens de l'Académie Royale des Sciences à l'auteur de ce journal, touchant les phénomènes de l'eau purgée d'air. In: *J. des Sçavants*, 25 juillet 1672, 5027–5030.
48. REYNOLDS, O. (1903a). Experiments Showing the Boiling of Water in an Open Tube at Ordinary Temperatures. In: *Univ. Press, Cambridge*. 1900–1903, 578–587.
49. REYNOLDS, O. (1903b). On the Internal Cohesion of Liquids and the Suspension of a Column of Mercury to a Height more than Double that of the Barometer. In: *Scientific Papers on Mechanical and Physical Subject, vol. I*. Cambridge: Cambridge Univ. Press, 231–247.
50. DE LUC, J.-A. (1803). Introduction à la physique terrestre par les fluides expansibles. Paris, 1803, 93.
51. BAKER, K.G., ROBERTSON, V.J., DUCK, F.A. (2001). A Review of Therapeutic Ultrasound: Biophysical Effects. In: *Phys Ther*. 2001, 81, 1351–1358.
52. ALEXANDER, L.D., GILMAN, D.R., BROWN, D.R., BROWN, J.L., HOUGHTON, P.E. (2010). Exposure to Low Amounts of Ultrasound Energy does not Improve Soft Tissue Shoulder Pathology: a Systematic Review. In: *Phys Ther*. 2010, 90, 14–25.
53. CONNORS, B.A., SCHAEFER, R.B., GALLAGHER, J.J., JOHNSON, C.D., LI, G., HANDA, R.K., EVAN, A.P. (2018). Preliminary Report on Stone Breakage and Lesion Size

Produced by a New Extracorporeal Electrohydraulic (Sparker Array) Discharge Device. In: *Urology*. 2018, Accepted Manuscript.

54. SHUTLER, N.D., MESLER, R.B. (1965). A Photographic Study of the Dynamic and Damage Capabilities of Bubbles Collapsing near Solid Boundaries. In: *Trans. ASME D: J. Basic Engng*. 1965, 87, 511–517.

55. TEMPERLEY, H.N.V., CHAMBERS, L.L.G. (1946). The Behaviour of Water under Hydrostatic Tension: I. In: *Proc. Phys. Soc.* 58, 1946, 420–436.

56. NITA, H. (1999). *U.S. Patent No. 6,007,514*. Washington, DC: U.S. Patent and Trademark Office.

57. BRENNAN, L., GESSWEIN, D., CORNISH, W., SIEGEL, R.J. (2002). *U.S. Patent No. 6,450,975*. Washington, DC: U.S. Patent and Trademark Office.

58. CHANDRASEKARAN, V., GUO, Z., REN, B.Q., FEDIE, B. (2003). *U.S. Patent No. 6,562,031*. Washington, DC: U.S. Patent and Trademark Office.

59. PETERSON, T., PAL, D. (2003). *U.S. Patent No. 6,617,760*. Washington, DC: U.S. Patent and Trademark Office.

60. HARE, B.A., PRASAD, J.S. (2004). *U.S. Patent No. 6,730,048*. Washington, DC: U.S. Patent and Trademark Office.

61. NITA, H., SARGE, J. (2008). *U.S. Patent No. 7,335,180*. Washington, DC: U.S. Patent and Trademark Office.

62. RABINER, R.A., HARE, B.A., MARCIANTE, R.I., VARADY, M.J. (2010). *U.S. Patent No. 7,794,414*. Washington, DC: U.S. Patent and Trademark Office.

63. NITA, H., SARGE, J., TRAN, M., NGUYEN, S. (2011). *U.S. Patent No. 7,955,293*. Washington, DC: U.S. Patent and Trademark Office.

64. NITA, H., SARGE, J., NGUYEN, S. (2009). *U.S. Patent No. 7,604,608*. Washington, DC: U.S. Patent and Trademark Office.

65. NITA, H. (2012). *U.S. Patent No. 8,133,236*. Washington, DC: U.S. Patent and Trademark Office.

66. NITA, H., SARGE, J. (2012). *U.S. Patent No. 8,221,343*. Washington, DC: U.S. Patent and Trademark Office.

67. NITA, H. (2012). *U.S. Patent No. 8,246,643*. Washington, DC: U.S. Patent and Trademark Office.

68. NITA, H., SARGE, J., TRAN, M., NGUYEN, S. (2012). *U.S. Patent No. 8,308,677*. Washington, DC: U.S. Patent and Trademark Office.

69. SOLTANI, A., HANSMANN, D.R. (2014). *U.S. Patent No. 8,740,835*. Washington, DC: U.S. Patent and Trademark Office.

70. MUNGER G., PANDEY, A., VISWANATHAN, R. (2007). *U.S. Patent Application No. 11/838,794*.

71. BANSEVIČIUS, R., BUBULIS, A., JÜRĒNAS, V., VALAIKA, M., MINCHENYA, V.T. (2008). *Ultrasound Wave Guide Wire for Internal Blood Vessels Cleaning*. Reg. No. 08478001.4/EP08478010, Nov 21, 2008. Pat. No. 2310.

72. EKOS CORPORATION. *EndoWave Infusion Catheter System*. [Accessed online August 10, 2017]. Via <http://www.whichmedicaldevice.com/by-manufacturer/233/552/endowave-infusion-catheter-system>

73. GROMMES, J., STRIJKERS, R., GREINER, A., MAHNKEN A.H., WITTENS, C.H. (2011). Safety and Feasibility of Ultrasound-Accelerated Catheter-Directed Thrombolysis in Deep Vein Thrombosis. In: *Journal of Vascular and Endovascular Surgery*. 41, 2011, 526–532.

74. STRIJKERS, R., DE WOLF, M., ARNOLDUSSEN, C., TIMBERGEN, M., DE GRAAF, R., TEN CATE-HOEK, A.H., WITTENS, C.H. (2015). Venous In-stent Thrombosis Treated by Ultrasound Accelerated Catheter Directed Thrombolysis. In: *European Journal of Vascular and Endovascular Surgery*. 49, 2015, 440–447.
75. ARGON MEDICAL DEVICES. (no year given). *CLEANERXT Rotational Thrombectomy System*. [Accessed online August 10, 2017]. Via <http://www.whichmedicaldevice.com/by-manufacturer/361/972/cleanerxt-rotational-thrombectomy-system>
76. BOSTON SCIENTIFIC. (no year given). *Coronary Thrombectomy System*. [Accessed online August 10, 2017]. Via <http://www.bostonscientific.com/EN-US/products/thrombectomy-systems/angiojet-ultra-coronary-thrombectomy-system.html>
77. COVIDEN. (no year given). Trellis Peripheral Infusion System. [Accessed online August 10, 2017]. Via <http://www.whichmedicaldevice.com/by-manufacturer/27/551/trellis-peripheral-infusion-system>
78. WYLIE, M., MCGUINES, G., GAVIN, G. (2010). A Linear Finite Element Acoustic Fluid-Structure Model of Ultrasonic Angioplasty *in Vivo*. In: *International Journal for Numerical Methods in Biomedical Engineering*. 26, 2010, 828–842.
79. SHI, A., HUANG, P., GUO, S., ZHAO, L., JIA, Y., ZONG, Y., WAN, M. (2016). Precise Spatial Control of Cavitation Erosion in a Vessel Phantom by Using an Ultrasonic Standing Wave. In: *Ultrasonics Sonochemistry*. 31, 2016, 163–172.
80. MORSE, P.M. (1981). Vibration and Sound. In: *Acoustic Society of America*. 1981, 311–326.
81. NYBORG, W.L. (1996). Physics of Low Frequency Therapeutic Ultrasound. Ultrasound Angioplasty. In: *Developments in Cardiovascular Medicine*. 178, 1996, 1-23.
82. GAVIN, G.P., MCGUINNESS, G.B., DOLAN, F., HASHMI, M.S.J. (2007). Performance Characteristics of a Therapeutic Ultrasound Wire Waveguide. In: *International Journal of Mechanical Sciences*. 2007, 298–305.
83. NAGHAVI, M., WANG, H., LOZANO, R., DAVIS, A., LIANG, X., ZHOU, M., VOLLSET, S.E., OZGOREN, A.A., ABDALLA, S., ABD-ALLAH, F., AZIZ, M.I. (2015). Global, Regional, and National Age-Sex Specific All-Cause and Cause-Specific Mortality For 240 Causes Of Death, 1990–2013: A Systematic Analysis for the Global Burden of Disease Study 2013. In: *Lancet* 2015, 385, 117–131.
84. EUROPEAN SOCIAL SURVEY. (2015). *ESS Round 7 (2014/2015) Technical Report*. London: ESS ERIC.
85. KRAJICER, Z., HOWELL, M.H. (2000). Update on Endovascular Treatment of Peripheral Vascular Disease: New Tools, Techniques, and Indications. In: *Texas Heart Institute Journal*. 2000, 27(4), 369.
86. ABRAMOWITZ, M., STEGUN, I.A. (1970). *Handbook of Mathematical Functions*. New York, Dover.
87. БРЕХОВСКИХ, Л.М., ГОНЧАРОВ, В.В. (1982). Введение в механику сплошных сред. Москва/Moscow: Наука.
88. TIMOSHENKO, S.P., GOODIER, J.N. (1970). *Theory of Elasticity*. New York: McGraw-Hill.
89. CHEN, E.J., NOVAKOFSKI, J. (1996). Young's Modulus Measurements of Soft Tissues with Application to Elasticity Imaging. In: *IEEE Transactions on Ultrasonics, Ferroelectrics, and Frequency Control*. 1996, 43 (1).
90. REKTORYS, K. (1980). *Variational Methods in Mathematics, Science and Engineering*. London: D. Reidel Publ. Company.

91. ТЮЛИН, В.Н. (1976). Введение в теорию излучения и рассеяния звука. Москва/Moscow: Наука.
92. SIPIDO, K.R., CALLEWAERT, G., CARMELIET, E. (1995). Inhibition and Rapid Recovery of Ca^{2+} current during Ca^{2+} Release from Sarcoplasmic Reticulum in Guinea Pig Ventricular Myocytes. In: *Circ Res.* 1995, 76, 102–109.
93. BERS, D.M. (2002). Calcium and Cardiac Rhythms. Physiology and Pathophysiology. In: *Circ Res.* 2002, 90, 14–17.
94. EARLEY, S., NELSON, M.T. (2006). Central Role of Ca^{2+} -Dependent Regulation of Vascular Tone *in Vivo*. In: *J Appl Physiol.* 2006, 101, 10–11.
95. MITSUI, M., KARAKI, H. (1990). Dual Effects of Carbachol on Cytosolic Ca^{2+} and Contraction in Intestinal Smooth Muscle. In: *Am J Physiol.* 1990, 258, 787–793.
96. VAN BREEMEN, C., MANGEL, A., FAHIM, M., MEISHERI, K. (1982). Selectivity of Calcium Antagonistic Action in Vascular Smooth Muscle. In: *Am J Cardiol.* 1982, 49, 507–510.
97. DAVIGNON, J., GANZ, P. (2004). Role of Endothelial Dysfunction in Atherosclerosis. In: *Circulation.* 2004, 109, 27–32.
98. ENDOH, M. (2008). Cardiac Ca^{2+} Signalling and Ca^{2+} Sensitizers. In: *Circ J.* 2008, 72, 1915–1925.
99. JONG WEON CHOI, SOO HWAN PAI. (2002). Changes in Hematologic Parameters Induced by Thermal Treatment of Human Blood. In: *Annals of Clinical & Laboratory Science.* 2002, 32 (4) 393–397.

Scientific Publications in the Interest Field of The Thesis

International Conferences:

1. BUBULIS, A., GARALIENĖ, V., JURĖNAS, V., VEIKUTIS, V., **NAVICKAS, J.** (2013). Ultrasound Impact on the Isolated Human Thorica and Ultrasound Appliance, Potential in Preventing Artery Grafting. *The Improvement of the Quality, Reliability and Long Usage of Technological Systems and Technical Processes*. October 9–16, 2013. Eilat, Israel.
2. BUBULIS, A., GARALIENĖ, V., JURĖNAS, V., VEIKUTIS, V., **NAVICKAS, J.** Effect of Ultrasound on the Isolated Human Thoracica that is Used for Coronary Artery Bypass Grafting. *Vibroengineering – 2013*. September 17–19, 2013. Druskininkai, Lithuania.
3. BUBULIS, A., GARALIENĖ, V., JURĖNAS, V., **NAVICKAS, J.** (2014). Ultrasound Impact on the Isolated Human Artery Samples *in Vitro*. *The Improvement of the Quality, Reliability and Long Usage of Technical Systems and Technological Processes*. December 9–16, 2014. Taba, Egypt.
4. BUBULIS, A., PILKAUSKAS, K., **NAVICKAS, J.**, LUGANOV, I., PRONKEVICH, S., MINCHENYA, V. (2014). Oscillatory Elastic Tools for Ultrasonic Technological Systems. *10th International Conference on Mechatronic Systems and Materials Opole*. July 7–10, 2014. Opole, Poland.
5. BUBULIS, A., BILINAUSKAITĖ, M., **NAVICKAS, J.**, GOLINKA, E., SAVICH-TRETYAKOV, E. (2015). Computational Analysis of the Blood Flow in the Cavitation-Affected Vein. *VII Международная конференция по оптико-электронным информационным технологиям Фотоникс-2015*. April 20–23, 2015. Vinnitsa, Ukraine.
6. BRITCH, M.A., BUBULIS, A., MINCHENYA, V., VEIKUTIS, V., **NAVICKAS, J.** (2015). Mechanism of Generation of the Flexural Vibrations in an Ultrasonic Waveguide. *Vibroengineering VE'2015 & International Conference of Young Researchers on Science and Practice SAP'2015*. October 14–15, 2015. Katowice, Poland.
7. BUBULIS, A., VEIKUTIS, V., **NAVICKAS, J.**, MONTVILA, A., TIRLIKAITĖ, M. (2016). Ultrasound Effects on Isolated Vascular Segments Function. *Acute Cardiac Care and Emergency Medicine, 5th Meeting*. May 06–07, 2016. Vilnius, Lithuania.
8. BUBULIS, A., **NAVICKAS, J.**, MAŽEIKA, D. (2016). Design and the Main Parameters of Tube-Shaped Ultrasound Wave Guide Wire. *21st Conference of Vibroengineering*. August 31–September 1, 2016. Brno, Czech Republic.
9. BUBULIS, A., MINCHENYA, V., VEIKUTIS, V., **NAVICKAS, J.**, BAKANAUSKAS, V., PALEVIČIUS, P. (2017). Experimental Research of the Main Parameters of Tube-shaped Ultrasound Wave Guid Wire. *IV International School-Conference for Young Scientists “Nonlinear*

Dynamics of Machines” SCHOOL-NDM 2017. April 18–21, 2017. Moscow, Russia.

Publications in the Proceedings of International Conferences:

1. BUBULIS, A., GARALIENĖ, V., JURĖNAS, V., VEIKUTIS, V., NAVICKAS, J. Effect of Ultrasound on the Isolated Human Thoracica that is Used for Coronary Artery Bypass Grafting. In: *Proceedings of the Conference Vibroengineering – 2013*. September 17–19, 2013. Druskininkai, Lithuania.
2. BUBULIS, A., PILKAUSKAS, K., NAVICKAS, J., LUGANOV, I., PRONKEVICH, S., MINCHENYA, V. (2014). Oscillatory Elastic Tools for Ultrasonic Technological Systems. In: *Proceedings of the 10th International Conference on Mechatronic Systems and Materials*. July 7–10, 2014. Opole, Poland.
3. BUBULIS, A., GARALIENĖ, V., JURĖNAS, V., NAVICKAS, J. (2014). Ultrasound Impact on the Isolated Human Artery Samples *in Vitro*. In: *Proceedings of Conference “The Improvement of the Quality, Reliability and Long Usage of Technical Systems and Technological Processes”*. December 9–16, 2014. Taba, Egypt.
4. BRITCH, M.A., BUBULIS, A., MINCHENYA, V., VEIKUTIS, V., NAVICKAS, J. (2015). Mechanism of Generation of the Flexural Vibrations in an Ultrasonic Waveguide. In: *Proceedings of Vibroengineering–2015 Conference*. October 14–15, 2015. Katowice, Poland.
5. BUBULIS, A., NAVICKAS, J., MAŽEIKĀ, D. (2016). Tube-Type Ultrasound Waveguide Application and Analysis. In: *Proceedings of Vibroengineering–2016 Conference*. August 31–September 1, 2016. Brno, Czech Republic.
6. BUBULIS, A., MINCHENYA, V., VEIKUTIS, V., NAVICKAS, J., BAKANAUSKAS, V., PALEVIČIUS, P. (2017). IV Experimental Research of the Main Parameters of Tube-Shaped Ultrasound Wave Guide Wire. In: *Proceedings of IV International School-Conference for Young Scientists “Nonlinear Dynamics of Machines” SCHOOL-NDM 2017*. April 18–21, 2017. Moscow, Russia.

Publications in international journals:

1. BUBULIS, A., MINCHENYA, V., VEIKUTIS, V., NAVICKAS, J., BAKANAUSKAS, V., PALEVIČIUS, P. (2017). Design and the Main Parameters of Tube-Shaped Ultrasound Wave Guide Wire. In: *Journal of Vibroengineering*. 2017, 19(2), 1383–1392
2. BUBULIS, A., GARALIENĖ, V., JURĖNAS, V., NAVICKAS, J., GIEDRAITIS, S. (2017). Effect of Low-Intensity Cavitation on the Isolated Human Thoracic Artery *in Vitro*. In: *Ultrasound in Medicine and Biology*. 2017, 43(5), 1040–1047.

3. KARGAUDAS, V., BUBULIS, A., **NAVICKAS, J.**, VITKUS, L., VENSLAUSKAS, M. (2017). Theoretical and Experimental Investigation of Tube-Shaped Waveguide Wire. In: *Journal of Measurements in Engineering*. 5(4), 2017, 257–265

Patents:

1. *Ultragarsinis vidinio kraujagyslių valymo įrenginys*. Lithuanian patent. No. LT 6342 B. Inventors: Algimantas BUBULIS, Giedrius JANUŠAS, Darius MAŽEIKA, Vytautas NAGINEVIČIUS, Vytautas OSTAŠEVIČIUS, Arvydas PALEVIČIUS, **Jonas NAVICKAS**. 2017.01.10. 7p.
2. *Ultragarsinis kraujagyslių rekanalizacijos įrenginys*. Lithuanian patent. No. LT 6342 B. Inventors: Algimantas BUBULIS, **Jonas NAVICKAS**, Vincentas VEIKUTIS, Vladimir MINCHENYA, Juri ALEKSEEV, Ivan ADZERICHO. 2018.05.10. 7p.

Annexes

Annex 1

Table 4. Causes of death — diseases of the circulatory system, EU residents, 2013 [1]

GEO/TIME	2011	2012	2013	2014
European Union (28 countries)	395.33	394.25	383.35	373.62
Belgium	311.36	308.89	301.2	281.89
Bulgaria	1,181.53	1,168.03	1,085.8	1,131.02
Czech Republic	713.31	704.21	670.25	615.18
Denmark	293.87	286.78	267.68	256.59
Germany	406.25	404.07	433.08	403.54
Estonia	752.45	745.41	718.16	699.56
Ireland	352.8	351.32	343.85	309.91
Greece	445.51	448.34	404.74	381.41
Spain	271.78	271.03	253.07	244.99
France	223.03	221.55	212.87	202.93
Croatia	759.53	691.12	694.56	678.55
Italy	343.8	343.58	322.79	310.14
Cyprus	417.77	402.17	341.57	351.84
Latvia	891.33	920.61	914.55	882.7
Lithuania	911.45	900.56	894.09	848.82
Luxembourg	365.93	332.2	310.76	296.93
Hungary	778.94	779.4	778.24	761.52
Malta	484.36	519.43	405.82	372.42
Netherlands	293.45	288.58	282.75	271.73
Austria	437.9	450.24	443.8	418.07
Poland	638.89	652.35	635.34	591.39
Portugal	315.74	323.6	304.77	305.76
Romania	1,039.91	1,039.17	968.58	951.3
Slovenia	463.12	462.42	451.54	451.26
Slovakia	743.63	712.13	711.63	654.55
Finland	422.21	411.85	388.22	378.79
Sweden	376.23	371.39	354.05	338.32
United Kingdom	284.96	284.6	276.4	264.94

Neighbour countries				
Liechtenstein	368.89	325.82	230.49	296.38
Norway	314.59	311.69	288.5	272.63
Switzerland	301.07	303.82	294.71	280.04
Serbia	1,048.48	1,017.68	954.13	931.61
Turkey	470.66	340.36	375.89	:

Table 5. Causes of death — diseases of the circulatory system, EU residents, younger than 65 years, 2013 [1]

GEO/TIME	2011	2012	2013	2014
European Union (28 countries)	49.42	48.44	47.09	45.67
Belgium	34.98	33.1	32.34	29.75
Bulgaria	175.05	161.39	156.25	166.85
Czech Republic	73.23	69.78	66.51	61.48
Denmark	31.97	29.7	28.56	28.68
Germany	41.3	40.49	40.13	38.77
Estonia	96.69	97.08	97.67	94.3
Ireland	37.5	37.07	35.37	34.01
Greece	54.41	54.07	51.31	50.48
Spain	28.16	27.91	27.67	27.37
France	26.69	25.92	25.01	24.39
Croatia	74.75	73.38	68.4	67.24
Italy	28.7	28.11	26.7	26.15
Cyprus	36.31	35.88	30.87	34.34
Latvia	163.98	156.9	153.13	149.38
Lithuania	145.81	142.2	133.85	127.43
Luxembourg	35.02	33.19	35.17	28.85
Hungary	117.15	111.77	105.81	106.87
Malta	44.74	48.52	35.04	35.07
Netherlands	30.29	29.9	27.56	25.93
Austria	36.93	34.63	34.46	31.89
Poland	91.48	95.17	91.47	84.75
Portugal	29.68	28.39	28.88	34.25
Romania	122.78	120.93	115.9	114.95
Slovenia	42.51	37.75	36.03	35.38

Slovakia	87.94	84.78	85.63	80.11
Finland	50.47	47.38	44.48	43.28
Sweden	31.93	30.34	30.74	28.96
United Kingdom	38.47	37.18	37.57	36.82
Neighbour countries				
Liechtenstein	31.36	28.06	21.62	20.73
Norway	27.99	29.12	24.85	23.86
Switzerland	24.6	25.11	23.33	23.15
Serbia	105.22	102.62	99.86	101.26
Turkey	60.84	58.58	62.24	n/a

Annex 2

Mathlab program *Soundwaves in Tissue Limited Fluid* calculations

```
clc
% Pradiniai ir Kraujo duomenys
rn=0.075; % cm
r1=0.3; % cm min
% r1=0.5; % cm max
fH=21800; % Daznis
lamdt=4.0; % lambda cm, duotas atstumas z asyje
ro=1000; % kraujo tankis kg/m3
%av=0.0006; % amplitudė x asyje cm
%bv=0.00025; % amplitudė y asyje cm
om=2*pi*fH; %daznis rad/s
cf=147000; %garso greitis kraujyje cm/s
kf=om/cf; % 1/cm
kk=4*pi^2/lamdt^2-kf^2;% bangos skaičius
k=sqrt(kk); % 1/cm
cs=om/k; % redukuotas greitis
cfssant=cf/cs; % greičiu santykis

% Audinys
E=0.6; % tamprumo modulis N/cm2
Em2=E*10000; % tamprumo modulis N/m2
ni=0.45;
roi=1050; % audinio tankis kg/m3
cik=(1-ni)*Em2/((1+ni)*(1-2*ni)*roi);
cim=sqrt(cik); % garso greitis m/s
ci=cim*100 ; % greitis cm/s
ki=om/ci;
kap=sqrt(ki^2-(2*pi/lamdt)^2); % bangos skaičius

% Santykiai
ros=roi/ro; % tankiu santykis audinys/kraujas
ks=kap/k; % bangu skaičiai
chi=ks/ros; %

% BESELIO funkcijos
% argumentai
krn=k*rn; % k*r0
kr1=k*r1; % k*r1
pr1=kap*r1; % kapa*r1

Nma=3; % ! Formato aprasymas
for nc=1: Nma
% argumentas k*r0
Inn=besseli(nc,krn);
```

```

Knn=besselk(nc,krn);
Innb=besseli(nc-1,krn)-Inn/krn; % isvestine Pazymejimas b
Knnb=-besselk(nc-1,krn)-Knn/krn; % isvestine
% argumentas k*r1
In=besseli(nc,kr1);%
Kn=besselk(nc,kr1);%;
Inb=besseli(nc-1,kr1)-In/kr1; % isvestine
Knb=-besselk(nc-1,kr1)-Kn/kr1; % isvestine
% argumentas kapa*r1 Pazymejimas p
Jn=besselj(nc,pr1);
Yn=bessely(nc,pr1);
Jnb=besselj(nc-1,pr1)-Jn/pr1; % isvestine
Ynb=bessely(nc-1,pr1)-Yn/pr1; % isvestine

Mn=chi*(In*Jn-Kn*Yn)/(Jn^2+Yn^2);
Nn=chi*(Kn*Jn+In*Yn)/(Jn^2+Yn^2);
MMn(nc)=Mn; % Masyvas Mn(n)
NNn(nc)=Nn; % Masyvas Nn(n)
Mvn=Knnb/(Innb^2+Knnb^2); % v reiskia vingis, t.y. arg k*r0
Nvn=Innb/(Innb^2+Knnb^2);
Rn=Inb-Jnb*Mn-Ynb*Nn;
Sn=Knb-Jnb*Nn+Ynb*Mn;
RRn(nc)=Rn; % Masyvas Rn(n)
SSn(nc)=Sn; % Masyvas Sn(n)
XXn(nc)=Mvn*Rn-Nvn*Sn;
YYn(nc)=Nvn*Rn+Mvn*Sn;
end
XXn;
YYn;
MMn;
NNn;
RRn;
SSn;

% Kavernu padetis ir ilgiai
tekzL=0; % teta z vamzdelio kavernos padetis laipsniais
tekL=140; % teta audinio kavernos padetis laipsniais
tekz=tekzL*pi/180; % radianais
tek=tekL*pi/180; % radianais

lamzL=120; % vamzd. kav. ilgis laipsniais
lamL=115; % audinio kav. ilgis laipsniais
lamz=lamzL*pi/180; % radianais
lam=lamL*pi/180; % radianais
spau=1;
if spau==1
disp(['Maziausios kavernos vertes parinktos'])
disp([' '])

```

```

end
disp(['Vamzdelio kavernos padetis tekz=', num2str(tekzL), ...
      ', kavernos ilgis lamz=', num2str(lamzL), ' laipsniu'])
disp(['Audinio kavernos padetis tek=', num2str(tekL), ...
      ', kavernos ilgis lam=', num2str(lamL), ' laipsniu'])

%ha, qa, hb, qb skaiciavimai: teta=tt, lamda=md
% Vamzdelio kavernos duomenys
tt=tekz;
md=lamz;
for nc=1:Nma
    for jc=1:Nma
        if jc==nc
            ha(jc,nc)=sin(2*nc*tt)*(sin(nc*md)/nc)*(cos(nc*md)-...
                sin(nc*md)/(nc*md));
        else
            ha(jc,nc)=sin((jc+nc)*tt)*sin((jc+nc)*md)/(jc+nc)+...
                sin((jc-nc)*tt)*sin((jc-nc)*md)/(jc-nc)-...

2*cos(nc*tt)*sin(nc*md)*sin(jc*tt)*sin(jc*md)/(nc*jc*md);
        end
        if jc==nc
            qa(jc,nc)=md+cos(2*nc*tt)*sin(2*nc*md)/(2*nc)-...
                2*(cos(nc*tt)*sin(nc*md))^2/(nc*nc*md);
        else
            qa(jc,nc)=cos((jc+nc)*tt)*sin((jc+nc)*md)/(jc+nc)+...
                cos((jc-nc)*tt)*sin((jc-nc)*md)/(jc-nc)-...

2*cos(nc*tt)*sin(nc*md)*cos(jc*tt)*sin(jc*md)/(nc*jc*md);
        end

        if jc==nc
            hb(jc,nc)=md-cos(2*nc*tt)*sin(2*nc*md)/(2*nc)-...
                2*(sin(nc*tt)*sin(nc*md))^2/(nc*nc*md);
        else
            hb(jc,nc)=cos((jc-nc)*tt)*sin((jc-nc)*md)/(jc-nc)-...
                cos((jc+nc)*tt)*sin((jc+nc)*md)/(jc+nc)-...

2*sin(nc*tt)*sin(nc*md)*sin(jc*tt)*sin(jc*md)/(nc*jc*md);
        end
        if jc==nc
            qb(jc,nc)=sin(2*nc*tt)*(sin(nc*md)/nc)*(cos(nc*md)-...
                sin(nc*md)/(nc*md));
        else
            qb(jc,nc)=sin((jc+nc)*tt)*sin((jc+nc)*md)/(jc+nc)-...
                sin((jc-nc)*tt)*sin((jc-nc)*md)/(jc-nc)-...

2*sin(nc*tt)*sin(nc*md)*cos(jc*tt)*sin(jc*md)/(nc*jc*md);
        end
    end
end

```

```

end
% Galiniu kavernu verciu koef.
hcp(nc) = sin(nc*tt+nc*md)-sin(nc*tt)*sin(nc*md)/(nc*md);
hcm(nc) = sin(nc*tt-nc*md)-sin(nc*tt)*sin(nc*md)/(nc*md);
qcp(nc) = cos(nc*tt+nc*md)-cos(nc*tt)*sin(nc*md)/(nc*md);
qcm(nc) = cos(nc*tt-nc*md)-cos(nc*tt)*sin(nc*md)/(nc*md);
end
haz=ha; % vamzdelio kavernos duomenys
qaz=qa;
hbz=hb;
qbz=qb;
hcpz=hcp;
hcmz=hcm;
qcpz=qcp;
qcmz=qcm;
% Audinio kavernos duomenys
tt=tek;
md=lam;
for nc=1:Nma
    for jc=1:Nma
        if jc==nc
            ha(jc,nc)=sin(2*nc*tt)*(sin(nc*md)/nc)*(cos(nc*md)-...
                sin(nc*md)/(nc*md));
        else
            ha(jc,nc)=sin((jc+nc)*tt)*sin((jc+nc)*md)/(jc+nc)+...
                sin((jc-nc)*tt)*sin((jc-nc)*md)/(jc-nc)-...
2*cos(nc*tt)*sin(nc*md)*sin(jc*tt)*sin(jc*md)/(nc*jc*md);
        end
        if jc==nc
            qa(jc,nc)=md+cos(2*nc*tt)*sin(2*nc*md)/(2*nc)-...
                2*(cos(nc*tt)*sin(nc*md))^2/(nc*nc*md);
        else
            qa(jc,nc)=cos((jc+nc)*tt)*sin((jc+nc)*md)/(jc+nc)+...
                cos((jc-nc)*tt)*sin((jc-nc)*md)/(jc-nc)-...
2*cos(nc*tt)*sin(nc*md)*cos(jc*tt)*sin(jc*md)/(nc*jc*md);
        end

        if jc==nc
            hb(jc,nc)=md-cos(2*nc*tt)*sin(2*nc*md)/(2*nc)-...
                2*(sin(nc*tt)*sin(nc*md))^2/(nc*nc*md);
        else
            hb(jc,nc)=cos((jc-nc)*tt)*sin((jc-nc)*md)/(jc-nc)-...
                cos((jc+nc)*tt)*sin((jc+nc)*md)/(jc+nc)-...
2*sin(nc*tt)*sin(nc*md)*sin(jc*tt)*sin(jc*md)/(nc*jc*md);
        end
        if jc==nc

```

```

qb(jc,nc)=sin(2*nc*tt)*(sin(nc*md)/nc)*(cos(nc*md)-...
sin(nc*md)/(nc*md));
else
qb(jc,nc)=sin((jc+nc)*tt)*sin((jc+nc)*md)/(jc+nc)-...
sin((jc-nc)*tt)*sin((jc-nc)*md)/(jc-nc)-...
2*sin(nc*tt)*sin(nc*md)*cos(jc*tt)*sin(jc*md)/(nc*jc*md);
end

end
% Galiniu kavernu verciu koef.
hcp(nc)= sin(nc*tt+nc*md)-sin(nc*tt)*sin(nc*md)/(nc*md);
hcm(nc)= sin(nc*tt-nc*md)-sin(nc*tt)*sin(nc*md)/(nc*md);
qcp(nc)= cos(nc*tt+nc*md)-cos(nc*tt)*sin(nc*md)/(nc*md);
qcm(nc)= cos(nc*tt-nc*md)-cos(nc*tt)*sin(nc*md)/(nc*md);
end
ha;
qa;
hb;
qb;

% LYGTYS
a11=haz(1,1)*XXn(1)+hbx(1,1)*YYn(1);
a12=haz(2,1)*XXn(1)+hbx(2,1)*YYn(1);
a13=haz(3,1)*XXn(1)+hbx(3,1)*YYn(1);
a14=qaz(1,1)*XXn(1)+qbx(1,1)*YYn(1);
a15=qaz(2,1)*XXn(1)+qbx(2,1)*YYn(1);
a16=qaz(3,1)*XXn(1)+qbx(3,1)*YYn(1);

a21=haz(1,2)*XXn(2)+hbx(1,2)*YYn(2);
a22=haz(2,2)*XXn(2)+hbx(2,2)*YYn(2);
a23=haz(3,2)*XXn(2)+hbx(3,2)*YYn(2);
a24=qaz(1,2)*XXn(2)+qbx(1,2)*YYn(2);
a25=qaz(2,2)*XXn(2)+qbx(2,2)*YYn(2);
a26=qaz(3,2)*XXn(2)+qbx(3,2)*YYn(2);
a31=haz(1,3)*XXn(3)+hbx(1,3)*YYn(3);
a32=haz(2,3)*XXn(3)+hbx(2,3)*YYn(3);
a33=haz(3,3)*XXn(3)+hbx(3,3)*YYn(3);
a34=qaz(1,3)*XXn(3)+qbx(1,3)*YYn(3);
a35=qaz(2,3)*XXn(3)+qbx(2,3)*YYn(3);
a36=qaz(3,3)*XXn(3)+qbx(3,3)*YYn(3);

a41=haz(1,1)*YYn(1)-hbx(1,1)*XXn(1);
a42=haz(2,1)*YYn(1)-hbx(2,1)*XXn(1);
a43=haz(3,1)*YYn(1)-hbx(3,1)*XXn(1); % Linkējimai vis dar
skaitantiems cia
a44=qaz(1,1)*YYn(1)-qbx(1,1)*XXn(1);
a45=qaz(2,1)*YYn(1)-qbx(2,1)*XXn(1);

```

```

a46=qaz(3,1)*YYn(1)-qbz(3,1)*XXn(1);
a51=haz(1,2)*YYn(2)-hzb(1,2)*XXn(2);
a52=haz(2,2)*YYn(2)-hzb(2,2)*XXn(2);
a53=haz(3,2)*YYn(2)-hzb(3,2)*XXn(2);
a54=qaz(1,2)*YYn(2)-qbz(1,2)*XXn(2);
a55=qaz(2,2)*YYn(2)-qbz(2,2)*XXn(2);
a56=qaz(3,2)*YYn(2)-qbz(3,2)*XXn(2);
a61=haz(1,3)*YYn(3)-hzb(1,3)*XXn(3);
a62=haz(2,3)*YYn(3)-hzb(2,3)*XXn(3);
a63=haz(3,3)*YYn(3)-hzb(3,3)*XXn(3);
a64=qaz(1,3)*YYn(3)-qbz(1,3)*XXn(3);
a65=qaz(2,3)*YYn(3)-qbz(2,3)*XXn(3);
a66=qaz(3,3)*YYn(3)-qbz(3,3)*XXn(3);

```

```

%      glz      g2z      e1z      e2z      e3z      g1      g2
g3      e1      e2
Ama=[a11      a12      a14      a15      a16      hb(1,1) hb(2,1)
hb(3,1) qb(1,1) qb(2,1);
      a21      a22      a24      a25      a26      hb(1,2) hb(2,2)
hb(3,2) qb(1,2) qb(2,2);
      a31      a32      a34      a35      a36      hb(1,3) hb(2,3)
hb(3,3) qb(1,3) qb(2,3);
      a41      a42      a44      a45      a46      ha(1,1) ha(2,1)
ha(3,1) qa(1,1) qa(2,1);
      a51      a52      a54      a55      a56      ha(1,2) ha(2,2)
ha(3,2) qa(1,2) qa(2,2);
      a61      a62      a64      a65      a66      ha(1,3) ha(2,3)
ha(3,3) qa(1,3) qa(2,3);
      hcpz(1) hcpz(2) qcpz(1) qcpz(2) qcpz(3) 0      0      0
0      0      ; % vamzd. kav.virs
      hcmz(1) hcmz(2) qcmz(1) qcmz(2) qcmz(3) 0      0      0
0      0      ; % vamzd. kav. apac
      0      0      0      0      0      0      hcp(1) hcp(2)
hcp(3)      qcp(1) qcp(2) ; % audinio kav. virs
      0      0      0      0      0      0      hcm(1) hcm(2)
hcm(3)      qcm(1) qcm(2) ]; % audinio kav. apac

```

```

e3=-0.096921;
g3z=-2.2104;

```

```

Bma=[-pi*YYn(1)-g3z*a13-e3*qb(3,1); -g3z*a23-e3*qb(3,2) ; -
g3z*a33-e3*qb(3,3) ; ...
      pi*XXn(1)-g3z*a43-e3*qa(3,1);-g3z*a53-e3*qa(3,2) ; -
g3z*a63-e3*qa(3,3); ...
      -g3z*hcpz(3); -g3z*hcmz(3); -e3*qcp(3); -e3*qcm(3) ];
egs=Ama\Bma;
egslin=egs';
glz=egs(1);

```

```

g2z=egs (2);
e1z=egs (3);
e2z=egs (4);
e3z=egs (5);
g1=egs (6);
g2=egs (7);
g3=egs (8);
e1=egs (9);
e2=egs (10);
% Furje koef. an, bn, anz, bnz pagal ju aprasyama
for jn=1:3
    San(jn)=g1*ha(1,jn)+g2*ha(2,jn)+g3*ha(3,jn)+...
        e1*qa(1,jn)+e2*qa(2,jn)+e3*qa(3,jn); % =pi*an
    Sbn(jn)=g1*hb(1,jn)+g2*hb(2,jn)+g3*hb(3,jn)+...
        e1*qb(1,jn)+e2*qb(2,jn)+e3*qb(3,jn); % =pi*bn
    Sanz(jn)=g1z*haz(1,jn)+g2z*haz(2,jn)+g3z*haz(3,jn)+...
        e1z*qaz(1,jn)+e2z*qaz(2,jn)+e3z*qaz(3,jn); % =pi*anz
    Sbnz(jn)=g1z*hbz(1,jn)+g2z*hbz(2,jn)+g3z*hbz(3,jn)+...
        e1z*qbz(1,jn)+e2z*qbz(2,jn)+e3z*qbz(3,jn); % =pi*bnz
end
Anfu= San/pi; % Furje eilutes koef. an
Bnfu=Sbn/pi; % Furje eilutes koef. bn
Anfuz= Sanz/pi; % Furje eilutes koef. anz - su zvaigzdute
Bnfuz=Sbnz/pi; % Furje eilutes koef. bnz - su zvaigzdute

% KONTROLE
Delta=[1, 0 ,0];
nj=3;
kontr1=Anfuz(nj)*XXn(nj)+Bnfuz(nj)*YYn(nj)+Bnfu(nj)+Delta(nj)*
YYn(nj); % turi buti 0
kontr2=Anfuz(nj)*YYn(nj)-Bnfuz(nj)*XXn(nj)+Anfu(nj)-
Delta(nj)*XXn(nj); % turi buti 0

for jn=1:3
    var=(RRn(jn))^2+(SSn(jn))^2;
    ccnbr=- (Bnfu(jn)*RRn(jn)+Anfu(jn)*SSn(jn))/var;
    CCnbr(jn)=ccnbr;
    ddnbr=(Bnfu(jn)*SSn(jn)-Anfu(jn)*RRn(jn))/var;
    DDnbr(jn)=ddnbr;
    AAnbr(jn)=ccnbr*MMn(jn)-ddnbr*NNn(jn);
    BBnbr(jn)=ccnbr*NNn(jn)+ddnbr*MMn(jn);
end
CCnbr;
DDnbr;
CCn=CCnbr*cs;
DDn=DDnbr*cs;

```

```

disp(['Sprendinio skystyje konst. C1=', num2str(CcN(1)), ', ';
C2=', num2str(CcN(2)), ', '; C3=', num2str(CcN(3))])
disp(['Sprendinio skystyje konst. D1=', num2str(DDn(1)), ', ';
D2=', num2str(DDn(2)), ', '; D3=', num2str(DDn(3))])
AAnbr;
BBnbr;
omka=om/kap;
AAn=AAnbr*omka;
BBn=BBnbr*omka;
disp(['Sprendinio audinyje konst. A1=', num2str(AAn(1)), ', ';
A2=', num2str(AAn(2)), ', '; A3=', num2str(AAn(3))])
disp(['Sprendinio audinyje konst. B1=', num2str(BBn(1)), ', ';
B2=', num2str(BBn(2)), ', '; B3=', num2str(BBn(3))])

for nc=1:3
Ife=besseli(nc,krn);
Kfe=besselk(nc,krn);
CIK(nc)=CcN(nc)*Ife-DDn(nc)*Kfe;
SIK(nc)=CcN(nc)*Kfe+DDn(nc)*Ife;
Ifel=besseli(nc,kr1);
Kfel=besselk(nc,kr1);
CIK1(nc)=CcN(nc)*Ifel-DDn(nc)*Kfel;
SIK1(nc)=CcN(nc)*Kfel+DDn(nc)*Ifel;

Jfe=besselj(nc,kr1);
Yfe=bessely(nc,kr1);
CAB(nc)=ros*(AAn(nc)*Jfe+BBn(nc)*Yfe);
SAB(nc)=ros*(AAn(nc)*Yfe-BBn(nc)*Jfe);

Jfk=besselj(nc,pr1);
Yfk=bessely(nc,pr1);
Alfan(nc)=AAn(nc)*Jfk+BBn(nc)*Yfk;
Betan(nc)=BBn(nc)*Jfk-AAn(nc)*Yfk;
end
CIK;
SIK;
CIK1; % Cn*In-Dn*Kn kai r=r1; koef. prie slegio cos(n*teta)
SIK1; % Cn*Kn+Dn*In kai r=r1; koef. prie slegio sin(n*teta)
CAB;
SAB;
Alfanr=Alfan*ros; % tankiu santykis*alfan; koef. prie slegio
cos(n*teta)
Betanr=Betan*ros; % tankiu santykis*betan; koef. prie slegio
sin(n*teta)
KnnG=besselk(1,krn); % Beselio funkcija K1 kai r=r0
KnnbG=-besselk(0,krn)-KnnG/krn;
dbsk=cs*KnnG/KnnbG; %daugiklis skaciuojant slegi kai r=r0,
begaliniame sk.

```

```

KnnG1=besselk(1,kr1); % Beselio funkcija K1 kai r=r1
dbsk1=cs*KnnG1/KnnbG; %daugiklis skaciuojant slegi kai r=r1,
begaliniame sk.

% SLEGIS KAIP KAMPO FUNKCIJA - - - - -
Njt=500;
for jt=1:Njt % slegis kaip kampo funkcija
    tet=-pi+2*pi*(jt-1)/(Njt-1);
    TetL(jt)=tet*180/pi;
    preds=CIK(1)*cos(tet)+CIK(2)*cos(2*tet)+CIK(3)*cos(3*tet)-
    ...
    SIK(1)*sin(tet)-SIK(2)*sin(2*tet)-SIK(3)*cos(3*tet); %
r=r0

preds1=CIK1(1)*cos(tet)+CIK1(2)*cos(2*tet)+CIK1(3)*cos(3*tet)-
    ...
    SIK1(1)*sin(tet)-SIK1(2)*sin(2*tet)-SIK1(3)*cos(3*tet); %
r=r1
    Preds(jt)=preds; % redukuotas skyscio slegis kai r=r0
    Preds1(jt)=preds1; % redukuotas skyscio slegis kai r=r1
    Predbg(jt)=dbsk*cos(tet); % red. slegis kai r=r0
begaliniame sk.
    Predbg1(jt)=dbsk1*cos(tet); % red. slegis kai r=r1
begaliniame sk.
end
TetL;
Preds;
Predbg;

% SLEGIS KAIP ATSTUMO FUNKCIJA (kampas tecL=const)
Njr=1000; % Parinkti varsl=3
rga=0.5; % cm, spindulys
tecL=0; % kampas
tec=pi*tecL/180; % tas pats kampas radianais
for jr=1:Njr
    rs=(rn+(rga-rn)*(jr-1)/(Njr-1))/rn; % santykinis spindulys
r/r0
    rsa=k*rs*rn; % Beselio funkcijos argumentai kai r<r1
    rsb=kap*rs*rn; % Beselio funkcijos argumentai, kai r>r1
    Rs(jr)=rs;
    if rs<(r1/rn)
        prsc=(CCn(1)*besseli(1,rsa)-
DDn(1)*besselk(1,rsa))*cos(tec)+... % redukuotas slegis
skystyje kaip r funkcija
        (CCn(2)*besseli(2,rsa)-
DDn(2)*besselk(2,rsa))*cos(2*tec)+...
        (CCn(3)*besseli(3,rsa)-DDn(3)*besselk(3,rsa))*cos(3*tec)-
    ...
        (CCn(1)*besselk(1,rsa)+DDn(1)*besseli(1,rsa))*sin(tec)-...

```

```

        (CCn(2)*besselk(2,rsa)+DDn(2)*besseli(2,rsa))*sin(2*tec)-
...
        (CCn(3)*besselk(3,rsa)+DDn(3)*besseli(3,rsa))*sin(3*tec);
Prsc(jr)=prsc;
else
prac=(AAn(1)*besselj(1,rsb)+BBn(1)*bessely(1,rsb))*cos(tec)+..
.
(AAn(2)*besselj(2,rsb)+BBn(2)*bessely(2,rsb))*cos(2*tec)+...
(AAn(3)*besselj(3,rsb)+BBn(3)*bessely(3,rsb))*cos(3*tec)+...
(AAn(1)*bessely(1,rsb)-BBn(1)*besselj(1,rsb))*sin(tec)+...
(AAn(2)*bessely(2,rsb)-
BBn(2)*besselj(2,rsb))*sin(2*tec)+...
(AAn(3)*bessely(3,rsb)-BBn(3)*besselj(3,rsb))*sin(3*tec);
%red. slegis audinyje kaip r funkcija, nepadaugintas is tankiu
sant.
Prsc(jr)=ros*prac; % red. slegis audinyje kaip r funkcija
end
KnnF=besselk(1,rsa); % Beselio funkcija K1
prbga=cs*KnnF/KnnbG; % red. slegis begaliniam skystyje
Prbga(jr)=prbga;
end
Rs;
Prsc;
% PARINKTI varsl
varsl=3;
if varsl==1
plot(TetL,Preds,TetL,Predbg,'--')
grid on
title('SLEGIS ANT VAMZDELIO.')
xlabel('Kampas teta laipsniais')
ylabel('Redukuotas slegis')
text(-120,5000,'begaliniam skystyje')
text(10,16000,'su kavernomis')
end
if varsl==2
plot(TetL,Preds1,TetL,Predbg1,'--')
grid on
title('SLEGIS prie AUDINIO.')
xlabel('Kampas teta laipsniais')
ylabel('Redukuotas slegis')
text(-140,1800,'begaliniam skystyje')
text(-45,350,'su kavernomis')
end
if varsl==3
plot(Rs,Prsc,Rs,Prbga,'--' )
grid on

```

```
title('SLEGIS. Punktyru - begaliniam skystyje ')
xlabel('Santykinis atstumas r/r0')
ylabel('Redukuotas slegis')
text(-140,1800,'begaliniam skystyje')
text(-45,350,'su kavernomis')
end
```

```
clear
```